NUMERICAL MODELING OF THE DAEDALIA PLANUM LAVA FLOWS, MARS

by

Nathan Beauchamp

B.S. in Geology, Michigan Technological University, 2012

Submitted to the Graduate Faculty of the

Kenneth P. Dietrich School of

Arts and Sciences in partial fulfillment

of the requirements for the degree of

Master of Science

University of Pittsburgh

2017

UNIVERSITY OF PITTSBURGH

DIETRICH SCHOOL OF ARTS AND SCIENCES

This thesis was presented

by

Nathan Beauchamp

It was defended on

11-28-17

and approved by

William Harbert, Professor, University of Pittsburgh

Eitan Shelf, Assistant Professor, University of Pittsburgh

Thesis Director: Michael Ramsey, Professor, University of Pittsburgh

NUMERICAL MODELING OF THE DAEDALIA PLANUM LAVA FLOWS, MARS

Nathan Beauchamp, M.S.

University of Pittsburgh, 2017

Mars has been a target of scientific research for decades as its surface records a varied geologic history including the largest shield volcanoes in the solar system (Rossi and van Gasselt, 2010). The evidence of volcanism, from the shield volcanoes and the lava flows that extend for hundreds of kilometers, garnered the interest of many scientists to determine why the volcanism on the planet is at a scale much larger than on Earth (Zimbelman, 1998). Many previous studies compared terrestrial and Martian flows using empirical relationships to determine values for parameters such as eruption rate and viscosity (Zimbelman, 1998; Hiesinger et al., 2007). These terrestrial based empirical relationships have not been verified as being applicable to planetary flows (Crisp & Baloga, 1990). This study seeks to examine this issue by duplicating the flows using numerical modeling with the FLOWGO thermorheologic model of Harris and Rowland (2001) and comparing the generated eruption rate and viscosity values.

For modeling of this study, the majority of model parameters were based on data taken from the terrestrial Piton de la Fournaise volcano except for values directly measured from the Mars flows such as flow dimensions and path slope. Dimensions of flows were measured from Mars Reconnaissance Orbiter's Context Camera (CTX) images of the study region in Daedalia Planum, Mars. Slope and flow thickness required the use of elevation data from the Mars Orbiter Laser Altimeter (MOLA) instrument. Using these parameters, a set of three different models were generated that reproduced the flows in the Daedalia Planum within 10% of their measured length. The results of this study were comparable to the eruption rates and viscosity values of previous

studies. This study has shown that Martian lava flows can be modeled using terrestrial flow parameter values with results comparable to prior solely empirical studies.

TABLE OF CONTENTS

LIST OF TABLES

LIST OF FIGURES

PREFACE

I would like to thank Mike Ramsey for all the help in guided me in my research. I would also like to thank my fellow graduate students Daniel, James, Kevin, and Christine for their support. I must also acknowledge the usefulness of the JMars software in providing an efficient means of identifying and acquiring image data used in this study.

Table 1: Table summarizing the symbols used in equations found in this study along with their corresponding units.

Symbol	**Definitions**	**Units**
E_r	Eruption rate	m^3/s
d	Depth/thickness of flow	m
ϕ	Crystal content/crystallinity	%
W	Flow width (includes levees)	km
w	Channel width	m
x	Flow length	km
τ_0	Yield strength	Pa
τ	Basal shear stress	Pa
T_{hot}	Maximum exposed surface temperature	°C
T_{base}	Base temperature	°C
T_{core}	core temperature	°C
ρ	Lava density	kg m^{-3}
θ	Slope	degrees
v_{mean}	Mean velocity	m/s
η	Viscosity	Pa-s
η_0	Dynamic viscosity at the liquidus temperature	Pa-s
η_f	Dynamic viscosity of a fluid	Pa-s
ε	Emissivity	dimensionless
Q_{rad}	Radiative heat loss	W/m
Q_{cond}	Conductive heat loss	W/m
Q_{force}	Convective heat loss	W/m
	Constants	
Symbol	Definitions	Values	Units
K	Thermal diffusivity	3.0×10^{-7}	m^2/s
G_z	Graetz number	300	dimensionless
g	Gravity constant	3.8	m/s^2

1.0 INTRODUCTION

The surface of Mars has channelized lava flows that extend for hundreds of kilometers compared to the largest (<50 km) flows found on Earth (Zimbelman, 1998; Garrey et al., 2007; Baloga and Glaze, 2008; Malin, 1980; Pinkerton and Wilson, 1994). The difference in maximum lengths may be attributed to various reasons such as differences in eruption rate, eruption volume, eruption period or rheology compared to Earth (Hauber et al., 2009). One of the arguments for this difference is that planetary specific conditions such as gravity, atmospheric pressure and temperature cause variations in the volcanism that separate them from Earth analogs. With one third Earth's gravity, Mars is assumed to have basaltic eruption rates 3-5 times higher than Earth. This higher eruption rate is caused by the requirement for the magma source to have a larger conduit to overcome the decrease in density driven buoyancy (Wilson and Head, 1994). Wilson and Head (1994) concluded that the lower gravity on Mars would cause a decrease in a flow's lateral spread, which requires an increase in thickness at the same flow volume. However, recent research does corroborate that gravity has the strongest effect on flow conditions on other planetary bodies but indicates that it causes a shortening of flows due to a decrease in downslope flow velocity. This decrease in flow velocity causes an increase in the time for flows to move the same distance, which implies a longer period for cooling and a decrease in the final flow length (Rowland et al., 2004). A countervailing conclusion comes from the study by Keszthelyi and Self (1998) who deduced that channelized flows longer than 100 km do not exit on Earth because they

require slopes of >5° over a sufficiently long length. Current research on Mars supports this inference as flows that are >> 100 km long have only been identified on steeper sides of shield volcanoes that have diameters of several hundred kilometers (Hauber et al., 2009).

Many previous studies such as Zuber et al., 2000, Hauber et al., 2009 and Hiesinger et al., 2007 have estimated properties of Martian flows such as eruption rate and viscosity using empirical relationships based on Earth data as a means of comparing the volcanism between the two planets. These relationships have been assumed to also be applicable to planetary data but the limited direct data on the properties of Martian flows hinders the ability to determine a quantitative empirical relationship (Crisp & Baloga, 1990).

One method for expanding beyond the previous work is to use numerical modeling to recreate Martian flows. This investigation utilized the numerical model FLOWGO to examine the potential difference in between terrestrial and Martian volcanism (Harris and Rowland, 2001). This work seeks to determine what flow parameters are entered to produce modeled flows with a length matching measured values.

1.1 GEOLOGIC HISTORY

Martian geologic history has included volcanic activity dating back to approximately 4 Gyr (Carr, 2007). This long geologic history has been separated into three coarse geologic eras: Oldest Noachian (4.65-3.7 Gyr), Hesperian (3.7-3.0 Gyr), and the youngest Amazonian (3.0 Gyr-present) (Rossi and van Gasselt, 2010; Neukum et al., 2001; Hartmann and Neukum, 2001; Greely et al, 2000). Evidence exists that indicates the planet's rate of volcanism peaked in the Noachian and

tapered out into the Hesperian with only periodic eruptions in the Amazonian (Carr and Head, 2010).

The large image dataset from the Viking Mission provided the best early dataset for Martian geologic investigations (Greely et al, 2000; Rossi and van Gasselt, 2010). Geologic investigations using Viking and later data sets have shown a lack of evidence for plate tectonics, which implies a stark difference in the geologic mechanism responsible for the formation of volcanoes on this planet. No mechanism for recycling of the lithosphere by plate tectonics has preserved the planet's volcanic history, which may extend to as recently as the last few 10s of millions of years (Rossi and van Gasselt, 2010; Neukum et al., 2004; Crown and Ramsey, 2016). This difference in geologic mechanisms has led to the volcanic activity on Mars being concentrated in discrete zones rather than along plate boundaries like on Earth (Carr, 2007). The largest volcanic zone is the Tharsis bulge that covers approximately 30,000,000 km² (5000 km across) and rises approximately 10 km above the median elevation (Carr, 2007; Phillips et al., 2001; Solomon and Head, 1982; Zuber et al., 2000; Banerdt et al., 1992 pages 249-297). On top of this bulge are the largest shield volcanoes found in the solar system (Harris, 2013b). The shield volcanoes on Mars indicate that volcanism should be basaltic in nature (Carr, 2007). This assumption has been reinforced by remote sensing data, which indicates a nearly uniform surface composition primarily separated into basalt or weathered basalt (Bandfield et al., 2000; Wyatt and McSween, 2002; Bibring et al., 2005).

Tharsis Montes is a string of three of the largest volcanoes on the Tharsis bulge (Figure 1) (Plescia, 2004; Carr, 2007). Arsia Mons is the southernmost shield of the three volcanoes and is 30 times larger than the largest volcano of Earth (Mauna Loa in Hawaii) at 400 km across and a height of 17.7 km (Plescia, 2004; Carr, 2007). The volcanoes' flanks have a slope of

approximately 5°, which shallows to the plains, with many regions having slopes less than 1° (Smith et al., 1999a). The focus of this work will be the volcanic plain to the south of the Arsia Mons called Daedalia Planum, which is a covered by series of overlapping lava flows (Warner and Gregg, 2003; Crown and Ramsey, 2016). Viking data were used by Scott and Tanaka (1986) to produce the initial geologic maps of the Daedalia Planum lava flows separating them into eight units that cover about 2.5 billion years of Martian volcanic history. Higher resolution (<20 m) image data provided by modern instruments were used to document the properties (e.g. flow length and width) and morphologies of the flows in the Arsia Mons region (Warner and Greg, 2003; Bleacher et al., 2007 a, b). The large spatial coverage and resolution (5-6 m) of CTX data sets allowed Crown et al. (2015) to relative age date the individual lava flows in the Daedalia flow fields based on small impact crater counting. These age data indicate a complex flow history covering a range in age from as young as ~100 my to ~1 Gya overlying even older plains (Crown and Ramsey, 2016; Crown et al., 2015). One reason for choosing this region for this study is that these flows are an important part of the planet's more recent history as they may represent the final stages of volcanism.

The study was performed in two regions approximately 370 km south of Arsia Mons (Figure 1). The study areas have a shallow average slope of less than 1°. Study Area A is generally made up of long (>100 km), sinuous flows that are easily separated into individual flows. Study Area B is generally made of numerous short (~80 km or less) flows that intermingle with one another making individual identification more difficult than Area A.

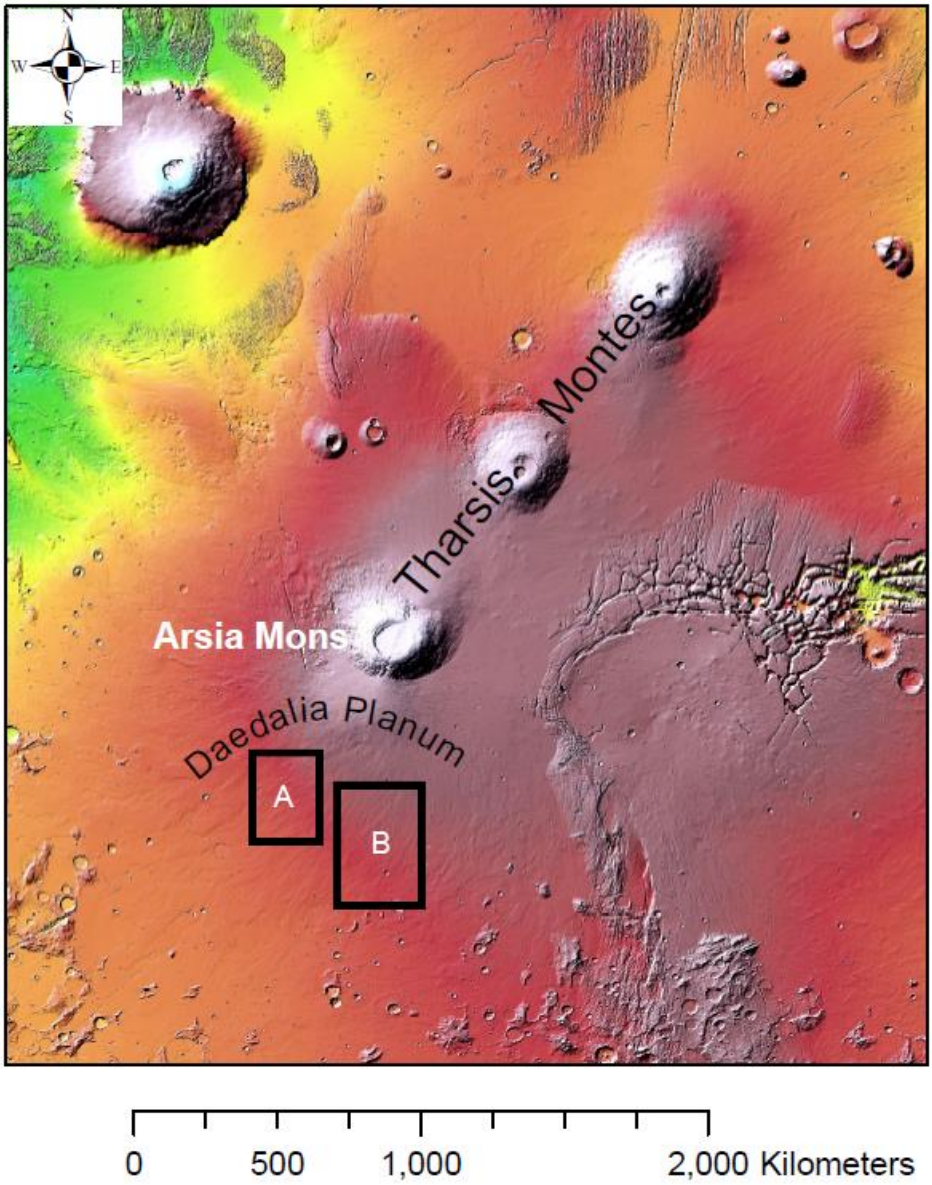

Figure 1: Image of Tharsis region with study site regions A and B identified. Original image is a subset of a MOLA Global Colorized Hillshade (Smith et al., 2003).

1.2 MODEL BACKGROUND

Two general assumptions of numerical models of lava flows is that they are either volume or cooling limited. Flows that are volume limited extend to their final length only once their supply of material is depleted without any influence of cooling and or rheological properties. Cooling

limited flows have a constant, unending material supply and do not stop until rheologic conditions caused by cooling make continued motion impossible (Harris, 2013b).

As this investigation seeks to examine the rheology of Martian flows, the cooling limited 1-D thermorheologic model FLOWGO was chosen (Harris and Rowland, 2001). The FLOWGO model is based on the flow being approximated as a single control volume that moves down an exact replica of the existing channel without impedance from the flow front (Wantin et al., 2013). The general model structure of the flow as seen in Figure 2 is assumed to be made up of a central channel surrounded by stagnant levees and covered by a fractured, discontinuous and moving carapace (Harris and Rowland, 2001). The discontinuous carapace is made up of a fractured crust that covers a fraction of the flow and insulates the hot inner core. The fractures through this crust expose the hot interior core that radiates heat through them at the maximum surface temperature (T_{hot}), which is less than the core temperature (T_{core}) (Crisp & Baloga, 1990; Harris et al. 2005; Harris, 2013b). The base of the flow is another thermal component that is separated from the inner core by its cooler temperature (T_{base}) induced by conductive cooling with the preexisting surface (Harris and Rowland, 2001; Wantin et al., 2013). The assumption that T_{hot} is cooler than T_{core} is based on the studies of the temperature difference between a flow's core and surface with a maximum difference of 300°C (Hon et al. 1994; Wright & Flynn 2003; Bailey et al. 2006; Harris, 2013b). The model takes this difference in temperature into account by subtracting a buffer temperature from the original core temperature with a value generally set at -140°C based on the work from Harris and Rowland (2001). The cooler surface crust has a temperature (T_{crust}) range of 360-650°C for active channel flow (Flynn & Mouginis-Mark 1994), whereas active pahoehoe flows have a crust that ranged from 390-770°C (Flynn & Mouginis-Mark 1992). Cooling of the

crust occurs over time with Hon et al. (1994) determining that crust that is 1 min old will have a temperature of 425-675°C.

FLOWGO can have the eruption rate be an input or as a dependent variable depending on the data available for the study flow. As no such data exists for this study region, the eruption rate was determined by Equation 1:

$$E_r = dwv_{mean} \quad (1)$$

which is a function of the flow's area (thickness (d) × channel width (w)) and flow velocity (v_{mean}) (Harris and Rowland, 2001; Harris et al., 2015; Harris and Rowland, 2015 a, b).

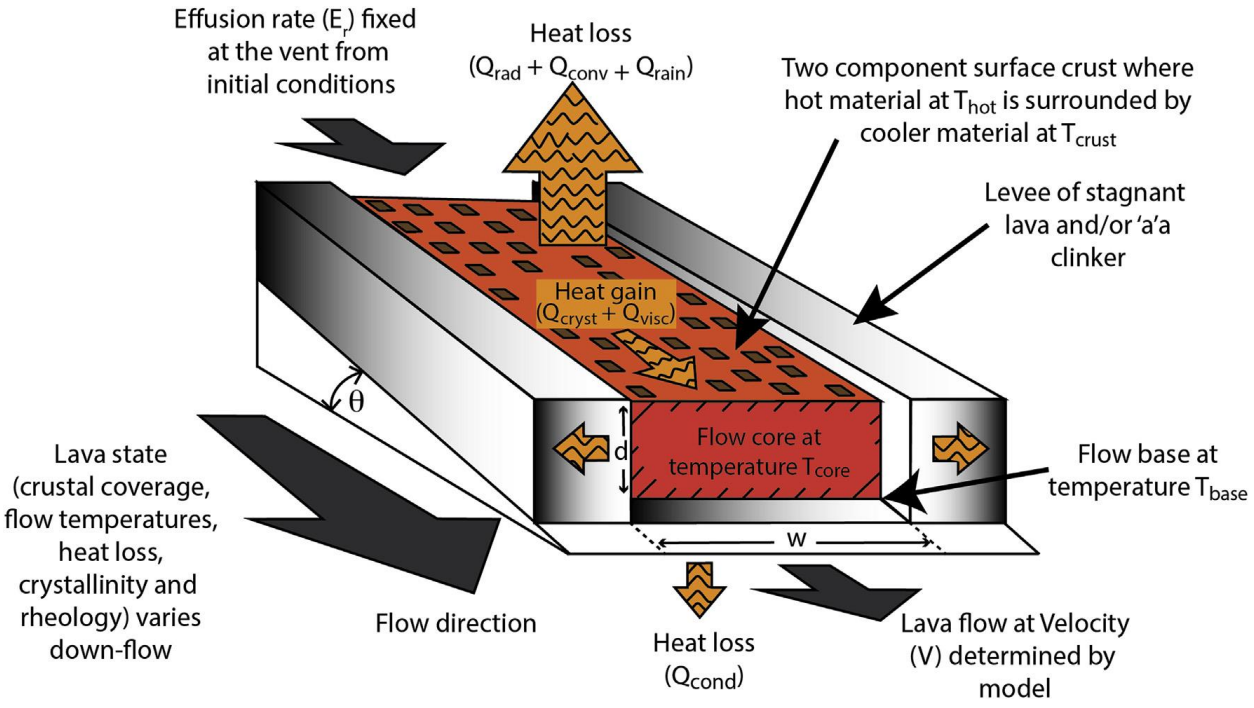

Figure 2: Figure that summarizes the flow structure used in the FLOWGO model. Figure reproduced from Chevrel et al., 2018 with permission from Elsevier (see Appendix D).

FLOWGO modeling runs through three major steps with the first determining the flows starting velocity using Equation 2. The velocities of the flow at each increment in the model are calculated using/solving the Jeffreys (1925) equation with the Bingham fluid modifications of

Moore (1987) for flow through a channel that is substantially wider then it is deep (Harris et al., 2007b). The following equation is the modified equation by Moore (1987):

$$v_{mean} = \left(\frac{d^2 \rho g sin(\theta)}{3\eta}\right)\left(3 - \frac{4}{3}\frac{\tau_0}{\tau} + \frac{1}{3}\left(\frac{\tau_0}{\tau}\right)^4\right) \quad (2)$$

in which the velocity (v_{mean}) is dependent upon gravity of the planetary body (g), density of the flow material (ρ), the thickness (d), the slope (θ), the viscosity (η), basal shear stress (τ) and the cores yield strength (τ_0) of the core of the flow. The second step has the core temperature of the flow decreased based on the heat loss by radiation (Q_{rad}) emitted from the cracks in the surface crust, conduction through the flow base (Q_{cond}) and convection of the atmosphere with the flow surface (Q_{force}) as shown in Figure 2 (Rowland et al., 2005). Further discussion of the heat loss model can be found in the original literature Harris and Rowland, 2001 or subsequent publications such as Harris et al., 2015 and Harris and Rowland, 2015.

The final step involves using the heat loss at each step to update the control volumes rheologic properties caused by a decrease in the flow's temperature (Harris and Rowland, 2001; Wantin et al., 2013). The model operates on the basis that the lava will continue to flow until it cools to a level where its rheology results in a velocity of zero (Rowland et al., 2005). This change in velocity is strongly controlled by changes in a flow's viscosity.

1.2.1 Lava Rheology: Viscosity

The flow of a fluid like lava is impeded by internal resistive forces such as viscosity (Harris, 2013b). The viscosity of lava is controlled by composition (silica content), water content, crystal content and temperature (Harris, 2013b). Modeling a flow's viscosity requires rheologic models that track changes in the lavas temperature (T_{core}) and crystallinity (ϕ) over time (Harris and

Rowland, 2015a, b). The Einstein-Roscoe relationship has been used to determine the bulk viscosity of a fluid and solid (crystal) mixture ($\eta(\phi)$) such as lava as a function of only crystallinity (Einstein, 1906; Roscoe, 1952). Equation 3 shows that the relationship depends on the dynamic fluid viscosity (η_f), starting phenocryst content (ϕ) and the value R. The value R is the inverse of the maximum crystal content (ϕ_{max}) that a flow can obtain before movement ceases (Harris and Rowland, 2015a, b).

$$\eta(\phi) = \eta_f(1 - R\phi)^{-2.5} \tag{3}$$

The best-fit temperature dependent η_f was determined based on the use of the empirical Vogel-Tanmann-Fulcher (VTF) equation (Equation 4) using chosen parameter constants shown in Table 2 (Mono and Pereira, 2004). Equation 4 contains the parameters D, E and F which are determined based on a melt composition such as those found in Hess and Dingwell, 1996; Giordano, 2006 and 2008 (Harris and Rowland, 2015a, b).

$$\eta(T) = 10\text{^}\left(D + \frac{E}{T_{core} - F}\right) \tag{4}$$

Table 2: Viscosity constant values used for flow models in this study. BAMB-S0 values taken from Chevrel et al., 2014.

	Piton Composition values	BAMB-S0
D	-4.52	-4.125
E	5558	4975
F	582.9	626.9

The original parameter values were based on the composition of Piton de la Fournaise volcano which has a composition dissimilar to Martian basalts. However, Martian basalts differ from terrestrial analogs most strongly in their high iron content (Chavrel et al., 2014). Chavrel et al. (2014) worked on the flow behavior of basalt with a composition similar to Martian basalt and concluded that the work done by Giordano et al. (2008) provides the best model approximation.

The equation parameters were updated based on the composition of the Backstay (BAMB) rock analyzed in situ on Mars (Ming et al., 2008). This rock is from the Columbia Hills of Gusev Crater and is an example of one of the few alkali basalts found on the surface of Mars in this region (Chavrel et al., 2014). This composition was chosen for this study as it has the highest and most similar viscosity to Piton de la Fournaise of those investigated by Chavrel et al. (2014) and also provides some level of ground truth data.

2.0 METHODS

2.1 DATA ACQUISITION

FLOWGO requires flows with distinct channels surrounded by stagnant levees (Harris and Rowland, 2001). An examination of the Daedalia on Plenum was performed using the global mosaic of Mars generated from Thermal Emission Imaging System (THEMIS) day data using the JMars software to identify flows with the required structure (Christiansen et al.; Hill et al., 2014 and Edwards et al., 2011). The global coverage of the mosaic and 100 m spatial resolution provided for easy identification of channelized structures but did not have the resolution needed for further detailed study (Hill et al., 2014 and Edwards et al., 2011). Figure 3a-b shows that THEMIS images provide higher contrast between flows allowing for easier initial identification compared to the higher resolution CTX images. Higher spatial resolution images were required to measure the dimensions including the flow length, channel width and area of the chosen flows for modeling and verification of results. Visible data of the study region were obtained using the Mars Reconnaissance Orbiter's Context Camera (CTX) at 5 m resolution as the instrument combines high spatial resolution and near complete coverage of the region. CTX is a single visible band instrument band pass of 0.5-0.7 μm with a ~30 km swath width (Malin et al., 2007) (Table 20 of Appendix A). Figure 4 shows how the flow length was measured down the centerline of the identified channel, and channel width was measured periodically along the flow with particular attention given to extremes (maximum or minimum). Channel width is required as a parameter for the modeling of each flow and flow length is needed for comparison to modeled flow length.

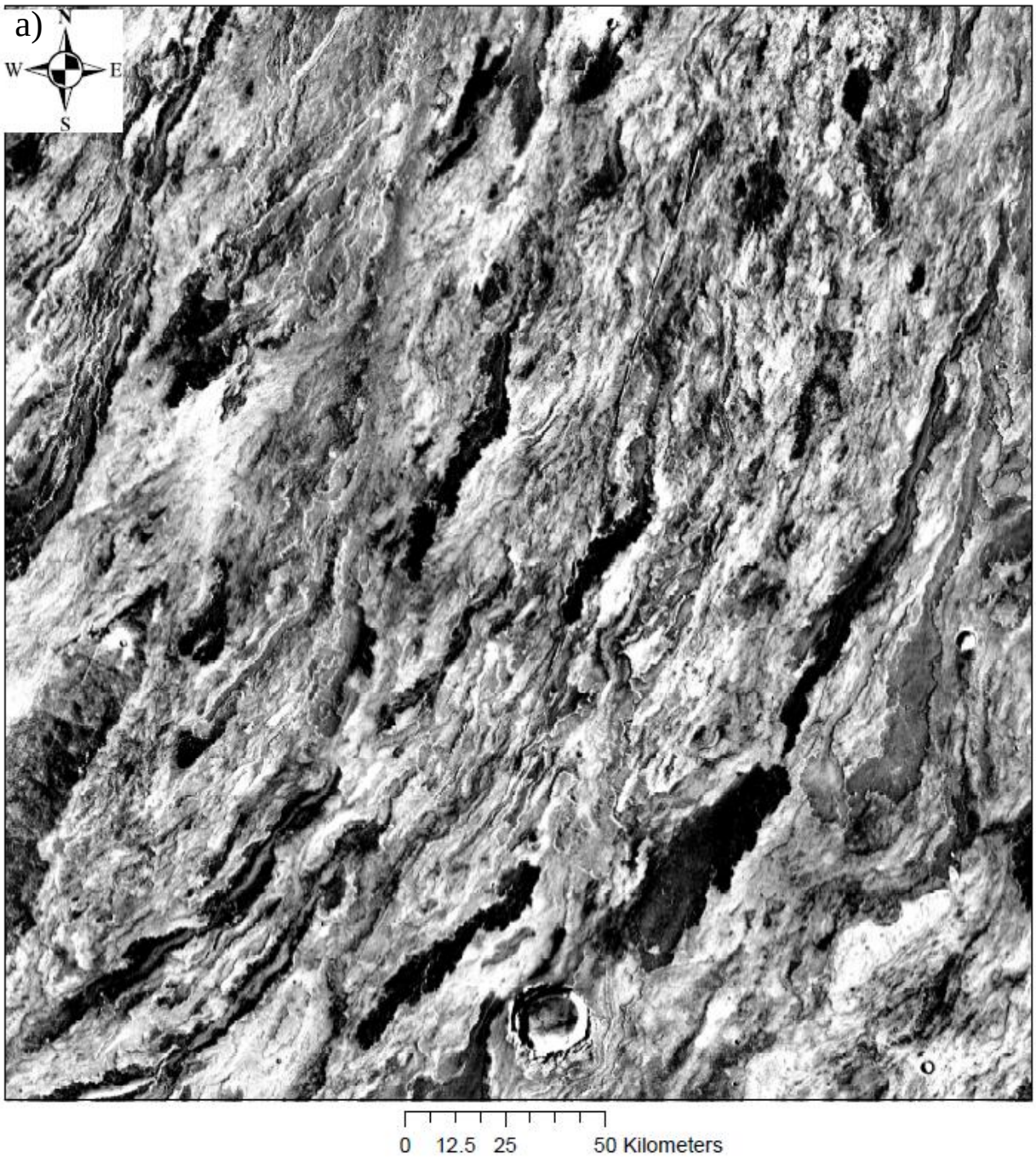

Figure 3: THEMIS (3a) and CTX (3b) subset images of Study Area B without flow outlines for clarity of flow fields.

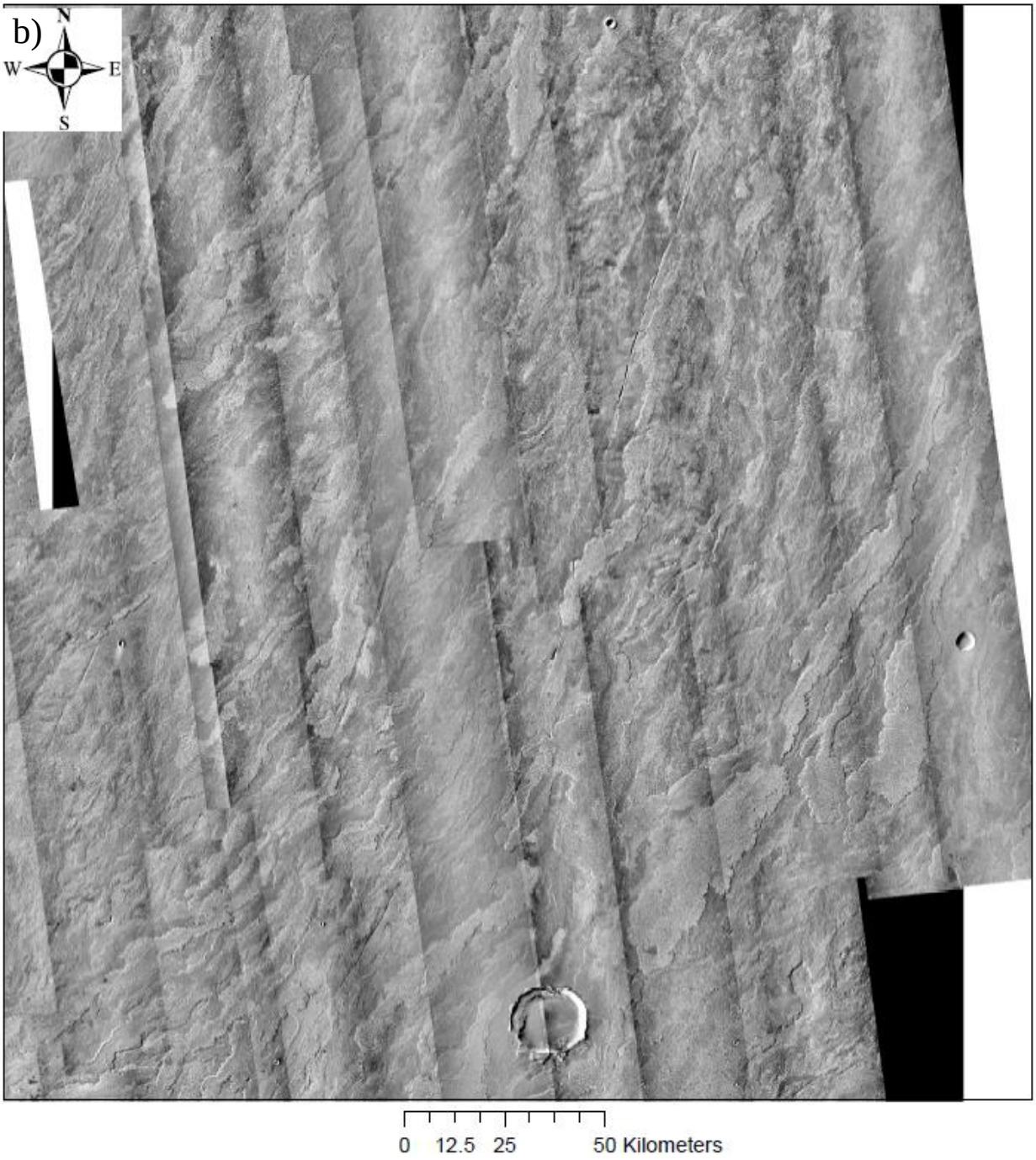

Figure 3: THEMIS (3a) and CTX (3b) subset images of Study Area B without flow outlines for clarity of flow fields.

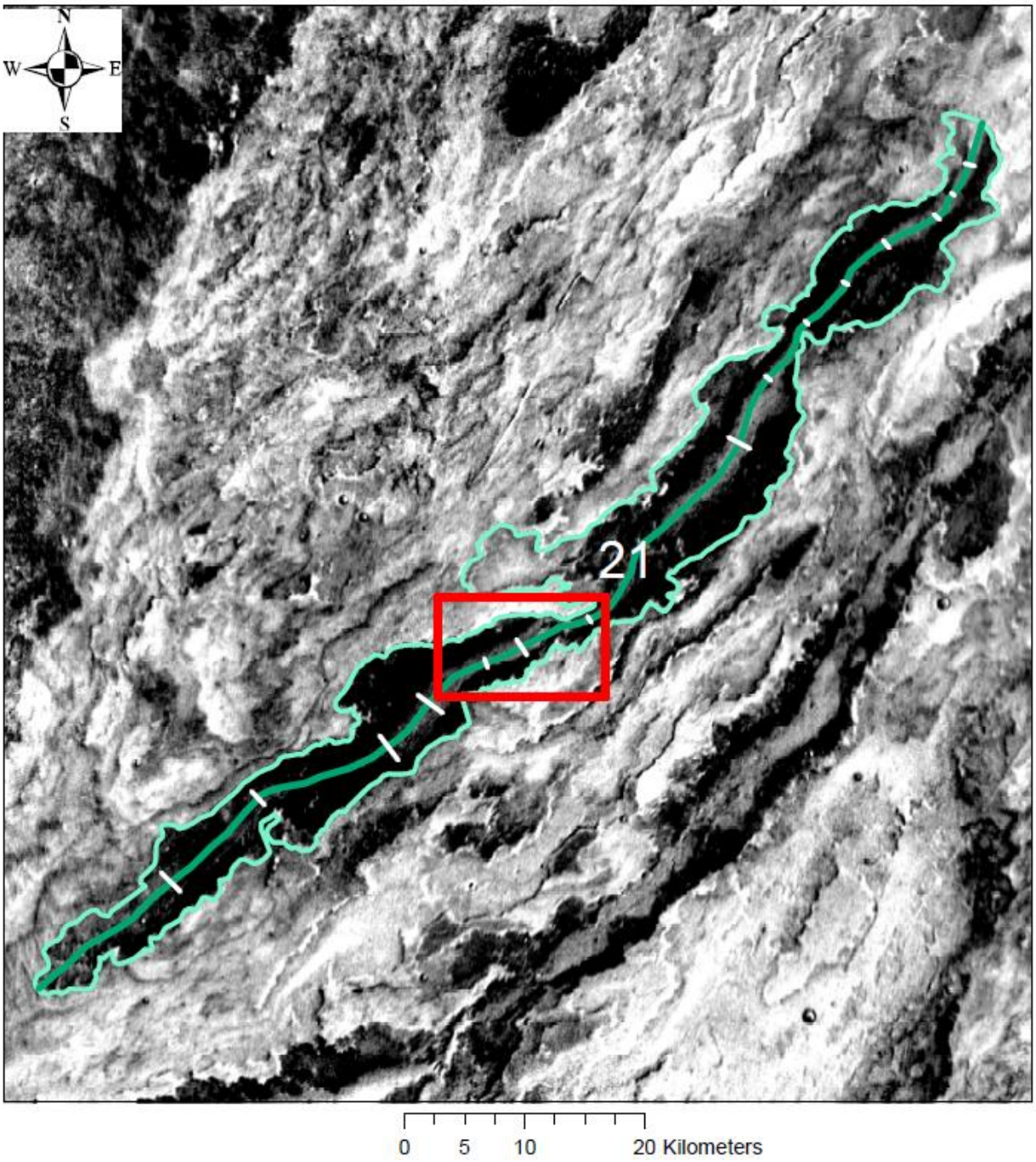

Figure 4: THEMIS mosaic image of Flow 21 with overlays of lines from which flow length and channel width were determined. Red outline indicates location of image shown in Figure 5.

Topographic data (flow thickness and slope) of studied flows was provided from the Mars Orbiter Laser Altimeter (MOLA) instrument, which has a vertical accuracy of up to 37.5 cm and horizontal accuracy of 100 m (Garvin et al., 2000 and Smith et al, 2001). MOLA was a laser

altimeter that measured elevation by determining the time difference between the transmission and reflected return of infrared laser pulses from the surface (Smith et al, 2001). Each measurement point was 130 m in diameter and spaced about 330 m apart (Garvin et al., 2000 and Glaze et al., 2003). The original point by point elevation data have been used to generate a global digital elevation model (DEM) by mathematically interpolating the elevation between points (Smith et al., 2003). This DEM was used to generate a slope map for the study region from which points of slope along a line parallel to each flow were acquired to determine the flow path slope for each iteration step of the model. This process was based on the assumption that the nearby regional slope would be nearly identical to the original flow path slope beneath the existing flows. Typically, FLOWGO slope data can come directly from the centerline of the existing channel but this method was chosen for this study as it avoids the smoothing caused by the existing flow. This region is made up of stacks of flows with only small variations in topography that that can be included in the model.

The thickness of each flow is not measured directly from the global DEM due to low topographic difference between the flows and surrounding terrain (Smith et al., 1999a**;** Glaze et al. 2003). Higher accuracy topographic data were obtained using the original precision experiment data records (PEDR) for the study region. MOLA PEDRs contain the original point by point elevation data rather than the gridded data provided by the DEM. At least five PEDR passes were chosen for each flow thickness calculation. Each path had the data points over the central channel and points to the south of the flow averaged as shown in Figure 3 in order to determine the elevation of each location. The channel thickness was subsequently determined by subtracting the regional elevation from the channel elevation. Regional elevation points were chosen to the south of the flow as the elevation increases moving north towards Arsia Mons. Care was taken in choosing

regional elevation data points as flows may meander and intermingle as shown in the upper right side of Figure 3 and thus no longer represent regional elevation.

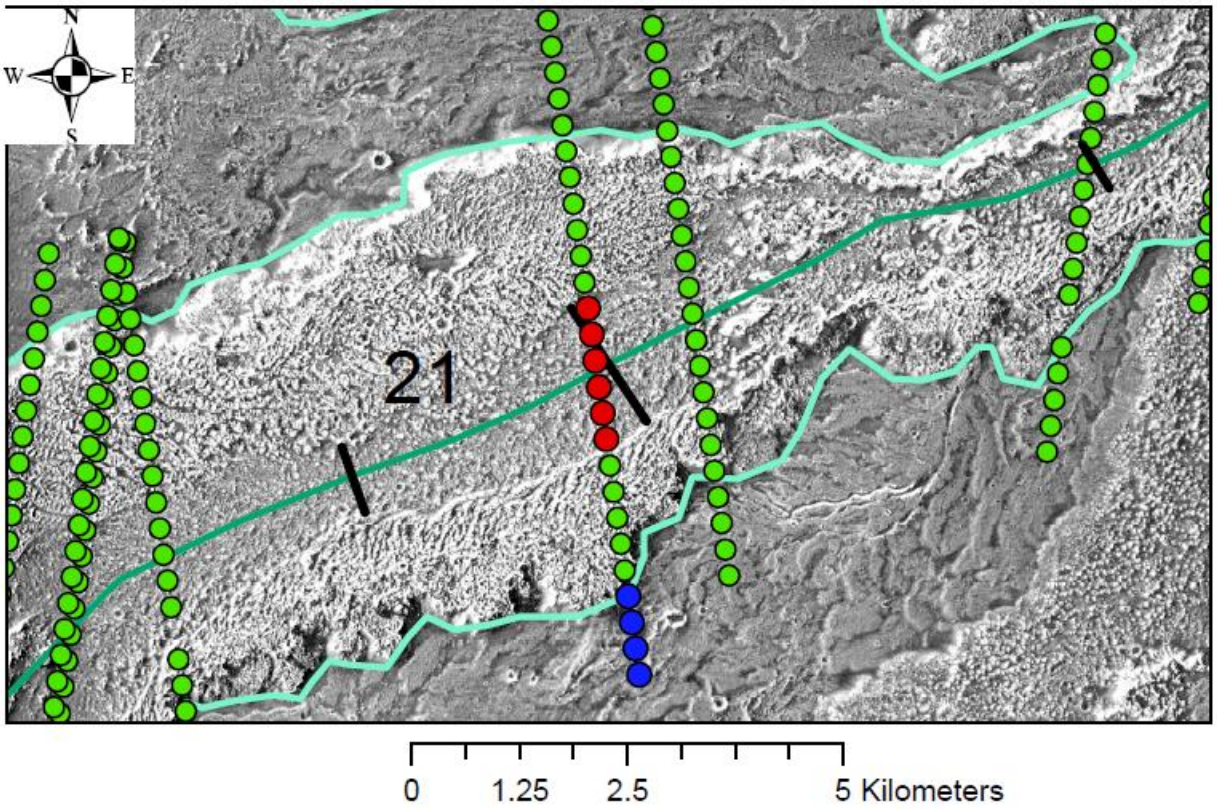

Figure 5: CTX image of Flow 21 from location outlined in Figure 4 depicting the PEDR data and its use for flow thickness calculation. Data points highlighted in red are averaged to determine the elevation of the central channel whereas data points highlighted in blue are averaged to determine the regional elevation value.

2.2 FLOWGO MODELING

The flows were initially modeled based on the rheological properties of the 2010 lava flows at Piton de la Fournaise volcano along with planetary specific properties such as gravity and atmospheric temperature and pressure as shown in Table 12 of Appendix A (Harris et al., 2015; Rowland et al. 2004). These values include eruption and base temperature, density and vesicularity, and convection parameters such as wind speed (Table 12). Eruption temperature was left unchanged at 1114°C as there is no direct value for Martian flows. Additional model parameters were determined specifically for this study including flow dimensions, emissivity, and crust temperature.

The dimensions of the model control volume for FLOWGO are generally measured from the beginning of each flow at the vent but identification of the starting point (vent location) in this study was not possible. Without the at-vent dimensions, the thickness value used in the model is an average of the measured thickness values for each flow and the minimum channel width was chosen as the input variable.

Emissivity is the material property that describes the how efficiently a surface radiates thermal energy which ranges from 0 to 1 as a perfect emitter (Sabins, 1997). This value is important as the higher the value the faster that the modeled flow will lose heat. The average basalt emissivity is 0.95, which is used in most studies (Harris, 2013a). The average value has been determined based on data taken from solid lava at ambient temperatures but investigations of active surfaces (molten) can result in an emissivity of ~0.8 (Harris, 2013a; Crisp et al., 1990;

Ramsey and Harris, 2016 and Wells and Cullinane, 2007). This work will cover both cases by running models for all flows using both as end member values.

Unlike emissivity, only one crust temperature value was chosen. Crust temperature can vary over a wide range (370-770°C) shown by the work of Flynn and Moughinis-Mark (1992). In order to determine the best value for this study, a set of models of Flow 3 over the emissivity range of 0.8-0.95 and a constant starting phenocryst content of 10% were generated. Four separate model runs were performed with emissivity values of 0.8, 0.85, 0.90 and 0.95 over the specified T_{crust} range of 580-720°C at 5°C intervals.

Utilizing the chosen average crust temperature value, four different model runs were performed with Table 3 showing a summary of differences between runs. The first model run ($M0_{0.80}$) is a control model that uses the original parameter values for the Piton de la Fournaise flow except for the chosen T_{crust} value and emissivity of 0.80 for all of the study flows. $M0_{0.80}$ held phenocryst content at a constant 10.4% without any attempt at fitting the modeled flow length to the measured value. This model run was conducted to determine any variation in model results between the flows irrespective of the best fit starting phenocryst content (ϕ). The other three model runs were integrated through a series of ϕ values until the modeled flow length matched the measured length within a margin of error (generally accepted for this study as ~1-5 km. Models were performed with different intervals for ϕ decreasing from 5% to as low as 0.001% over a starting phenocryst content range of 0% to 40% to determine the best fitting value for each flow. Large parameter intervals were used to first determine a narrow range over which the finer intervals can be used to determine the best fitting value for each flow.

Table 3: Table with the parameters separating the four different model runs performed for the study.

	Phenocryst Content	Emissivity	Viscosity
$M0_{0.80}$	Constant at 10.4%	0.80	Piton de la Fournaise
$M1_{0.80}$	Best fit values	0.80	Piton de la Fournaise
$M1_{0.95}$	Best fit values	0.95	Piton de la Fournaise
$M2_{0.80}$	Best fit values	0.80	Mars Specific

2.2.1 Sensitivity Analysis

To understand how variables effect model results, the sensitivity of the model for selected variables was investigated. Model runs were done in which phenocryst content, eruption temperature, crust temperature, vesicularity and average slope were varied individually with all other parameters held constant based on the best fitting model results for Flow 3. Each sensitivity model had different but constant variable intervals with results for each run compared to the original starting results. The sensitivity was determined by having all changes in the chosen variable and resulting changes in flow length and eruption rate change to the percentage of the starting value based on Equation 5 given below:

$$\text{Sensitivity} = \frac{original\ model\ value - new\ value}{original\ model\ value} \times 100 \quad (5)$$

Two additional full model runs ($M1_{0.95}$ and $M2_{0.80}$) were performed to fully examine the difference caused by changes in model parameters. Model $M1_{0.95}$ differs from $M1_{0.80}$ by its emissivity. Model $M2_{0.80}$ differs from the other models in that it uses a different set of compositionally determined constants for its viscosity model with the Martian specific values taken from Chevrel et al. (2014).

2.3 ERUPTION RATE CALCULATIONS FOR MARS

Many previous studies (Pinkerton and Wilson, 1994; Wilson and Head, 1983; Zimbelman, 1985; and Hiesinger et al., 2007) use the concept of the Graetz number to estimate a flow's eruption rate as a check on the model values, a similar calculation was performed for the investigated flows. The eruption rate was estimated using the empirical based equation given below:

$$Q = G_z * K * x * \left(\frac{W}{d}\right) \quad (6)$$

which it depends on a flow's length (x), thickness (d) and width (W). The other variables include thermal diffusivity (K) and the dimensionless Graetz number (G_z) with values taken from literature (Pinkerton and Wilson, 1994; Wilson and Head, 1983; Zimbelman, 1985; and Hiesinger et al., 2007). The Graetz number describes the relationship between a flow's heat loss through diffusion and the rate at which heat is advected along the length of the flow (Gregg and Fink, 1996; Pinkerton and Wilson, 1994). A Graetz number value of 300 was chosen for most studies based on previous work that show flows cease to advance at that value (Pinkerton and Wilson, 1994). Thermal diffusivity is the final variable in the equation with a value set at 3.0×10^{-7} m^2/s but is highly dependent on composition (Gregg and Fink, 1996; Warner and Gregg, 2003; and Hiesinger et al., 2007).

3.0 RESULTS

3.1 FLOW DATA

Twenty-one possible flows were identified within the study region from examination of THEMIS mosaic images. These initial flows were identified based on the presence of visible channels required for modeling. These initial flow selections were then limited to nine based on quality and length of identified leveed channel and availability of MOLA data. The nine flows (2-6, 12, 19-21) from the original selection provide a wide range in length, thickness, and channel width (Table 4). The flows were separated into study Area A that contains three flows (2,5 and 6) and six more in study Area B as shown in Figure 6. Figure 7 shows how the flows range in length from as short as 48.82 km for Flow 19 to as long as 214.61 for Flow 5. Thickness ranges from a minimum of 13.8 m to a maximum of 44.46 m, with slope varying from 0.33-0.88 degrees. The flows generally show a southwest direction with Flow 2 having an almost westerly direction.

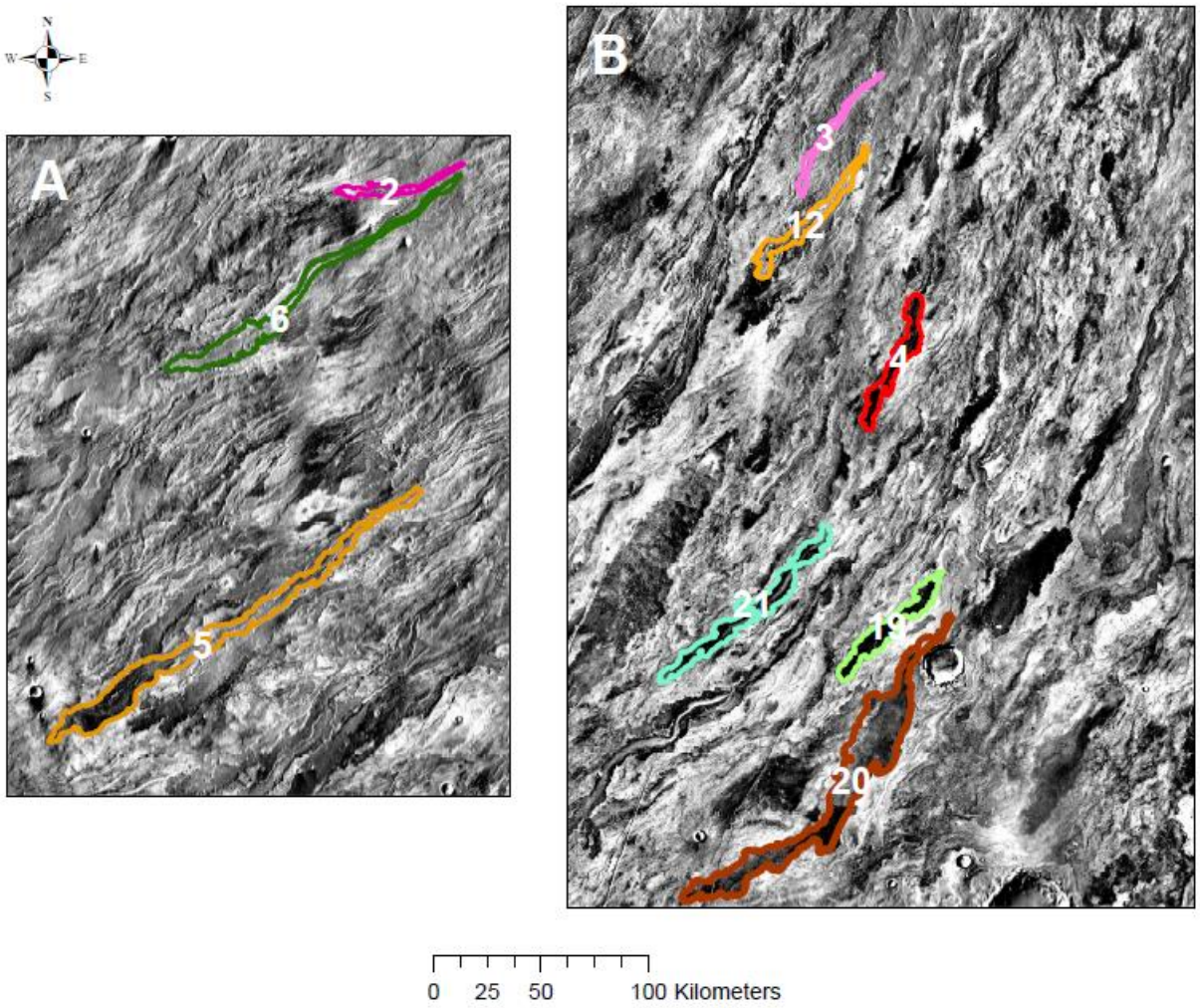

Figure 6: Study Regions A and B made up of flow outlines overlaying a subset of the global THEMIS day mosaic.

The gradual change in slope of the region causes flows in close proximity to have similar average slope values such as Flows 2 and 6 at 0.88 and 0.83 respectively. Whereas Flow 2 and 6 are close in path slope, their other parameters such as thickness and length differ greatly at 26.87 m versus 44.46 m and 63.95 km versus 174.54 km respectively. The thinnest flow is Flow 3 at only 13.8 m and its slope falls in the middle range of chosen flows at 0.64° and a measured length of 71.72 km. Flow shape varies greatly as Table 4 shows that the flow width (including levees) for narrow flows like Flow 3 is only 1.92 km compared to 6.37 km for Flow 4 even though their lengths differ by less than 4 km.

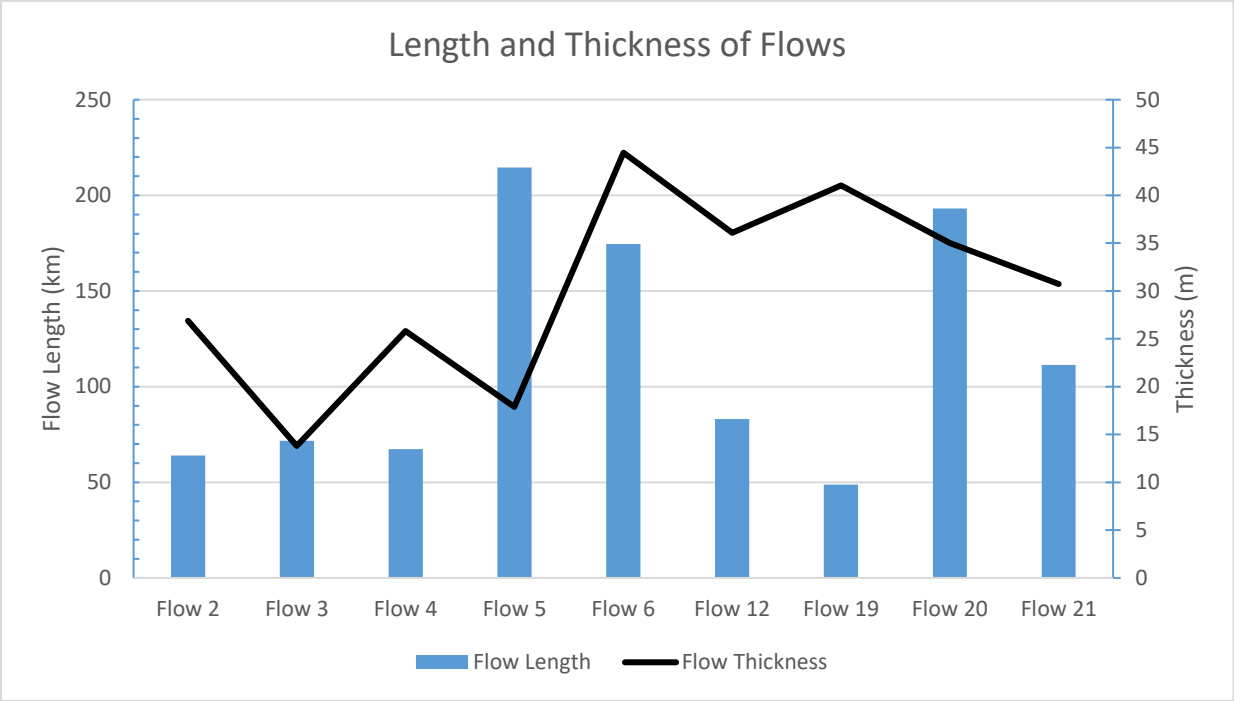

Figure 7: Plot of the flow length and thickness for study flows.

Table 4: Table of the measured flow parameters in this study.

	Flow 2	Flow 3	Flow 4	Flow 5	Flow 6	Flow 12	Flow 19	Flow 20	Flow 21
Length (km)	63.95	71.72	67.27	214.61	174.54	83.03	48.82	193.09	111.28
Area (km^2)	176.78	137.99	428.62	1,468.62	786.84	373.08	453.18	1,916.26	687.88
Flow Width (km)	2.76	1.92	6.37	6.84	4.51	4.49	9.28	9.92	6.18
Avg. Slope (°)	0.88	0.66	0.47	0.48	0.83	0.54	0.37	0.34	0.33
Thickness (m)	26.87	13.80	25.83	17.90	44.46	36.10	41.04	35.02	30.72
Minimum Channel Width (m)	185.22	149.55	878.58	264.59	139.14	213.47	624.01	691.96	342.88
Maximum Channel Width (m)	536.20	465.05	1,558.17	686.53	931.37	628.96	1,675.12	3,201.19	1,215.86

3.2 FLOWGO MODEL

Crust temperature for this study was based on the combination of Earth based data for a temperature range and varying the flow's emissivity over a constant phenocryst content. Figure 8 shows a subset of model results for Flow 3 for this step with a crust temperature range of 580-720°C at 10.0% starting phenocryst content. The results show that the lower the emissivity value used in the model, the higher the crust temperature required to match the measured flow length. The modeled length decreases linearly with increasing crust temperature until around a modeled length of 65 km after which the relationship levels out. Careful examination of the results show that Flow 3 is best modeled over a crust temperature range of 605-649°C depending on the emissivity value. Using the results from this set of model runs, an approximate average crust temperature of 625°C was chosen. This is the best value chosen based on the parameters and the flow used during the temperature determination analysis.

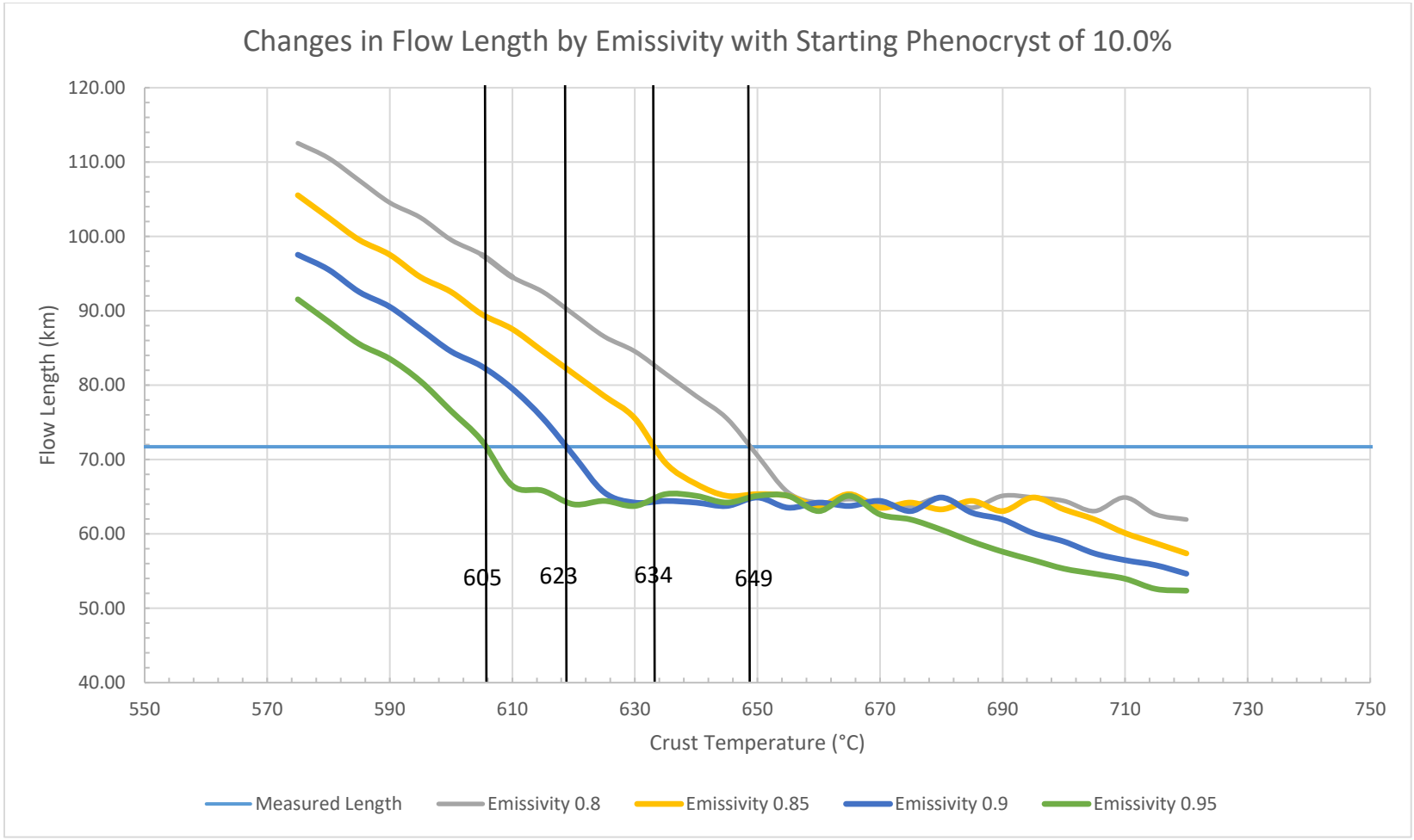

Figure 8: Model results for Flow 3 at a starting phenocryst content of 10% and at specified emissivity values over a range of crust temperatures. Vertical lines indicate crossing point of modeled and measured flow length with the crust temperature (°C) at each point annotated over the crossing lines.

Using the determined crust temperature and other model parameters, the control Model $M0_{0.80}$ produced modeled flows longer than the measured value except for the longest flow (Flow 5) that was modeled at approximately half the measured length (see Table 5). Most modeled flows were more than double their measured value with Flow 19 having the greatest difference at being 25.19 times longer than the measured length. This large disparity in model results can be attributed in part due to a differences in flow path slope and thickness between each flow. Flow 19 has the third lowest average slope of 0.37 degrees compared 0.642 degrees of Flow 3 that has the lowest difference in modeled versus measured flow length at only 14 percent longer. Variation in thickness is even greater with Flow 19 being the second thickest at 41.04 m compared to only 13.8 m for Flow 3.

Table 5: Table that summarizes the model results from $M0_{0.80}$. $M0_{0.80}$ is set at a crust temperature of 625°C, starting phenocryst content of 10.4% and an emissivity of 0.8.

	Flow 2	Flow 3	Flow 4	Flow 5	Flow 6	Flow 12	Flow 19	Flow 20	Flow 21
Measured Length (km)	63.95	71.72	67.27	214.61	174.54	83.03	48.82	193.09	111.28
Modeled Length (km)	891.799	81.54	442.63	108.49	2049.36	1273.06	1278.52	732.64	483.87
Flow Length Difference	12.95	0.14	5.58	-0.49	10.74	14.33	25.19	2.79	3.35
Eruption Rate (m^3/s)	2.32×10^5	1.62×10^4	4.58×10^5	1.09×10^5	5.66×10^5	5.06×10^5	3.50×10^5	1.01×10^6	2.32×10^5
Width (m)	185.22	149.55	878.58	264.59	139.14	213.47	624.01	691.96	342.88
Depth (m)	26.87	13.8	25.83	17.9	44.46	36.1	41.04	35.02	30.72
Crust Temperature (°C)	625	625	625	625	625	625	625	625	625
Phenocryst Content	10.4%	10.4%	10.4%	10.4%	10.4%	10.4%	10.4%	10.4%	10.4%
Emissivity	0.8	0.8	0.8	0.8	0.8	0.8	0.8	0.8	0.8
Ave. Slope	0.875	0.642	0.471	0.485	0.828	0.539	0.37	0.346	0.328
Min. Eruption Rate (m^3/s)	1.62×10^4		Max. Eruption Rate (m^3/s)		1.01×10^6				

The results of Model $M0_{0.80}$ indicated a need to change the starting phenocryst content for each flow in order to reach a modeled flow length similar to the measured value. Figure 9 shows an example for Flow 3 model results for Model $M1_{0.80}$ with a phenocryst interval of 1%. The best fit model for this flow benefited from the work on the determination of the crust temperature which narrowed down possible starting phenocryst content to be higher than 10% but likely below 20%. This assumption came from the fact that the flow length at an emissivity of 0.8 and a 10% phenocryst content needed a crust temperature of 649°C.

Flow 19 was not as easy to determine the best fit phenocryst content as Figure 10 shows that the content must be in the region of 30% phenocryst content. Figures 10 show that changes in phenocryst interval size gives different resolution of changes in flow length caused by phenocryst content. At an interval of 2.5% there appears to be only one best fit solution but at 0.25% and 0.05% intervals, three separate best fit values become apparent. This model result is the best at showing that models must be run at a sufficiently small interval to determine a best fit value. This result is unique in the fact that there are three possible best fit phenocryst values ranging from 28.6% to 29.7% which is only a 1.1% variance in possible values. Flow 21 has shown a similar occurrence of multiple best fit values (only 2 in this case) the difference between such values is very small at less than 1%.

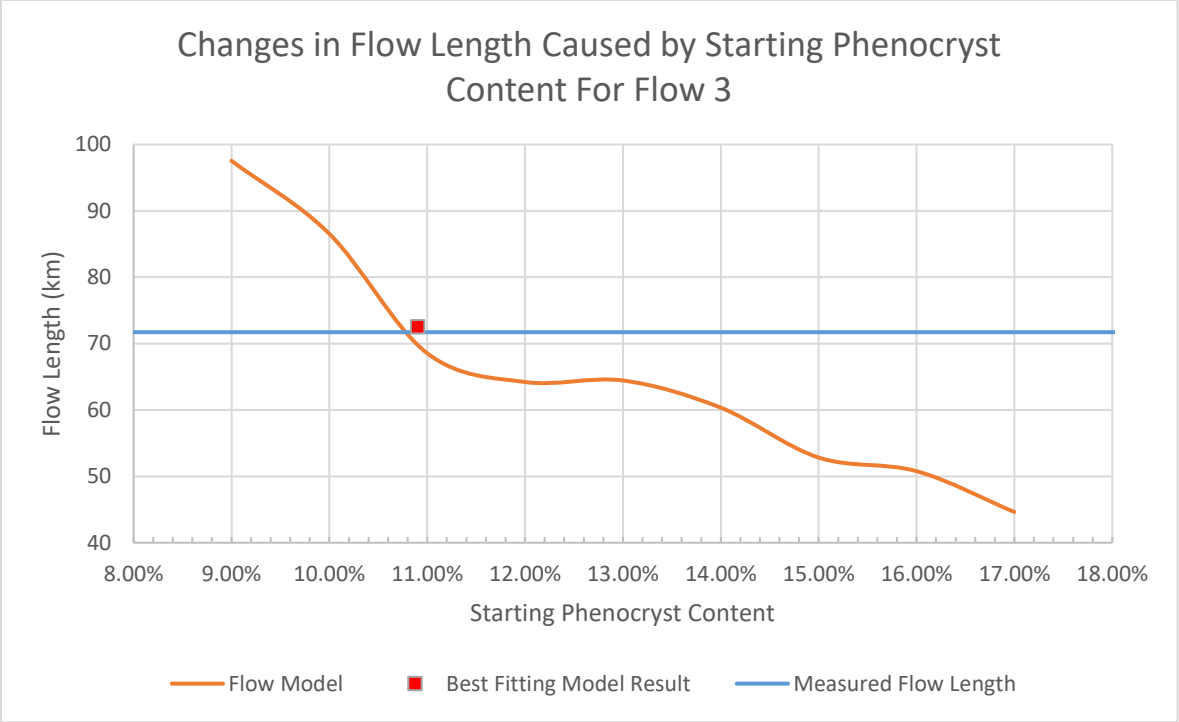

Figure 9: Model results for changes in Flow 3 length for Model $M1_{0.80}$ over a range of starting phenocryst content at a 1% interval. The best-fit point does not fall on the line as it was identified at a smaller phenocryst interval.

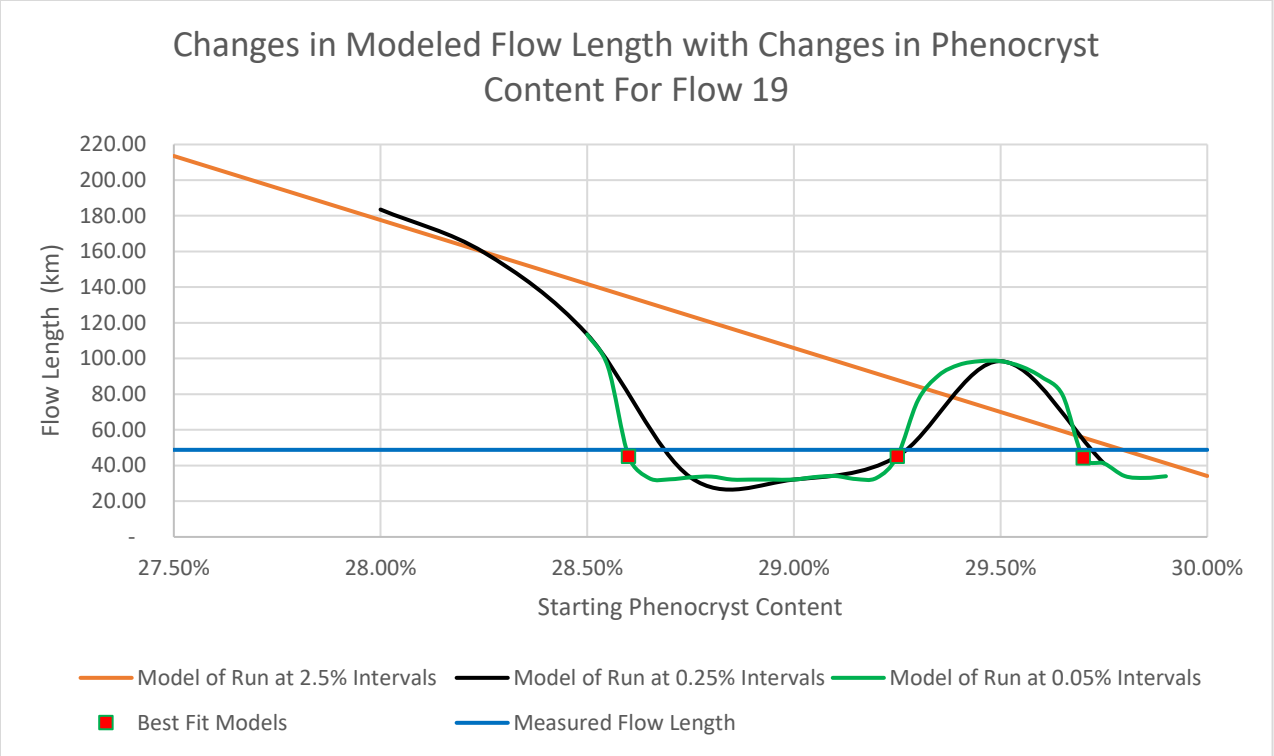

Figure 10: Model results for changes in Flow 19 length for Model $M1_{0.80}$ over a range of starting phenocryst content. The best fit model values for starting phenocryst content are identified separately for clarification.

Modeling of flows at Daedalia Planum indicates they have a relatively high crust temperature (625°C) and have a starting phenocryst content that ranges from 0% to 33.3% for Model $M1_{0.80}$ (Table 6). Best fit model results required the increase of starting phenocryst content from 10.4% to a minimum of 10.9% for Flow 3 and a maximum of 33.3% for Flow 6. General observations of results show that three of the four flows over 100 km in length had the lowest starting phenocryst content ranging from 10.9% to a maximum of 19.27%. Flow 6 is an outlier as it is one of the longest flows at 174.54 km but has the highest required phenocryst content. Flow 2 has the second highest starting phenocryst content at 30.77% and is similar to Flow 6 in that its average slope is also over 0.8 degrees. Modeled flow lengths have a high degree of match to the measured length with the greatest difference for Flow 6 with it being 9.34% shorter than measured.

Flow 5 is unique in the fact that a decrease in starting phenocryst content to 0% is required for the flow length to be similar the measured value with it only being 9.31% shorter.

Table 6: Table summarizing the modeled length and starting phenocryst content of specified models.

	Flow 2	**Flow 3**	**Flow 4**	**Flow 5**	**Flow 6**	**Flow 12**	**Flow 19**	**Flow 20**	**Flow 21**
Flow Length (km)									
Measured Length	63.95	71.72	67.27	214.61	174.54	83.03	48.82	193.09	111.28
$M0_{0.80}$	891.80	81.54	442.63	108.49	2049.36	1273.06	1278.52	732.64	483.87
$M1_{0.80}$	63.80	72.54	61.01	194.56	172.36	78.80	45.13	191.64	109.87
$M1_{0.95}$	63.80	72.54	66.63	210.47	171.21	89.06	46.52	198.64	111.87
$M2_{0.80}$	63.80	73.54	67.63	214.81	176.36	87.06	45.44	186.64	111.87
$\frac{M0_{0.80}}{Measured}$	12.95	0.14	5.58	-0.49	10.74	14.33	25.19	2.79	3.35
$\frac{Measured - M1_{0.80}}{Measured}$	-0.23%	1.14%	-9.31%	-9.34%	-1.25%	-5.09%	-7.56%	-0.75%	-1.27%
$\frac{Measured - M1_{0.95}}{Measured}$	-0.24%	1.14%	-0.96%	-1.93%	-1.91%	7.26%	-4.71%	2.87%	0.53%
$\frac{Measured - M2_{0.80}}{Measured}$	-0.23%	2.54%	0.54%	0.09%	1.04%	4.85%	-6.93%	-3.34%	0.53%
Starting Phenocryst Content									
$M1_{0.80}$	30.77%	10.90%	24.00%	0.00%	33.30%	24.90%	28.60%	19.27%	17.41%
$M1_{0.95}$	30.13%	9.20%	22.40%	0.00%	32.70%	24.56%	28.27%	18.25%	17.00%
$M2_{0.80}$	30.55%	10.25%	22.90%	4.40%	33.07%	24.79%	28.50%	18.95%	17.82%
$\frac{M1_{0.80} - M1_{0.95}}{M1_{0.80}}$	-0.64%	-1.70%	-1.60%	0.00%	-0.60%	-0.34%	-0.33%	-1.02%	-0.41%
$\frac{M1_{0.80} - M2_{0.80}}{M1_{0.80}}$	-0.22%	-0.65%	-1.10%	4.40%	-0.23%	-0.11%	-0.10%	-0.32%	0.41%

3.3 ERUPTION RATES

Model $M1_{0.80}$ produced eruption rates of that range from 1.57×10^4 m^3/s to as high as 5.85×10^5 m^3/s (average of 1.65×10^5 m^3/s). Table 7 shows that the flows can be separated in this model into two broad groups with flows 2, 3, and 19 having an eruption rates below 60,000 m/s^3 and flows 4-6, 12, and 20-21 with eruption rates greater than 90,000 m^3/s.

Figure 11 shows how modeled eruption rates compare to rates taken from literature review. Terrestrial eruption rates are only fraction of the model results, Historic Hawaiian eruptions have a maximum eruption rate of 500 m^3/s, which is approximately one-thirtieth the minimum model value (Rowland and Walker, 1990). The difference between the model eruption rates and Hawaiian eruptions is not unusual compared to the several order of magnitude differences found in the estimated eruption rates for Martian flows found in Table 7 and Figure 11. Examples of this variation include Pieri and Baloga (1986) that gave a range of 9×10^2-1×10^6 m^3/s and Hauber et al. (2011) with a range of 23-4.3×10^4 m^3/s. The large range of results even include the maximum eruption rate of 404 m^3/s found by Hiesinger et al. (2007) that is very similar to the previously mentioned Hawaiian rate. As a secondary means of comparing to these previous studies, eruption rates were calculated using the Graetz number method for the flows in this study giving a range of 5.92×10^2-7.38×10^3 m^3/s. Figure 11 shows that this range is substantially below the model results but are still within the ranges of previous Martian flow studies.

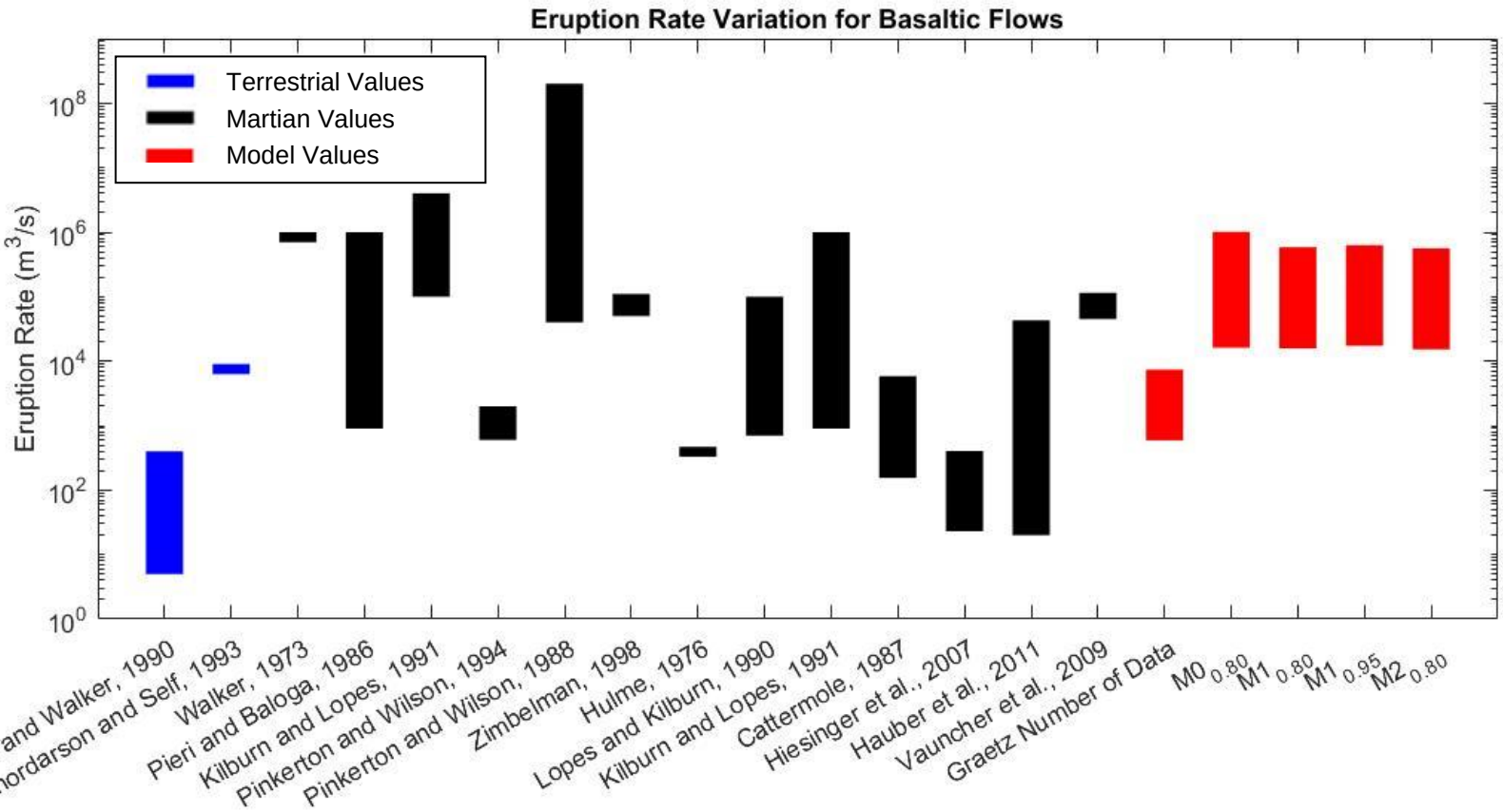

Figure 11: Compilation of basalt flow eruption rate estimates in a logarithmic scale from literature and model results. Data taken from Table 15 in Appendix A.

Table 7: Table that summarizes the eruption rate results from the various different models for the flows in this study.

	Flow 2	**Flow 3**	**Flow 4**	**Flow 5**	**Flow 6**	**Flow 12**	**Flow 19**	**Flow 20**	**Flow 21**
					Eruption Rate (m/s^3)				
$M0_{0.80}$	2.32×10^5	1.62×10^4	4.58×10^5	1.09×10^5	5.66×10^5	5.06×10^5	3.50×10^5	1.01×10^6	2.32×10^5
$M1_{0.80}$	5.19×10^4	1.57×10^4	1.71×10^5	1.78×10^5	9.98×10^4	1.96×10^5	4.35×10^4	5.84×10^5	1.49×10^5
$M1_{0.95}$	5.54×10^4	1.73×10^4	1.99×10^5	1.78×10^5	1.07×10^5	2.01×10^5	4.67×10^4	6.28×10^5	1.53×10^5
$M2_{0.80}$	4.97×10^4	1.53×10^4	1.78×10^5	1.38×10^5	9.59×10^4	1.85×10^5	4.16×10^4	5.60×10^5	1.35×10^5
$\frac{M1_{0.80} - M1_{0.95}}{M1_{0.80}}$	6.76%	10.00%	15.75%	0.00%	6.84%	2.82%	7.46%	7.41%	2.99%
$\frac{M1_{0.80} - M2_{0.80}}{M1_{0.80}}$	-4.11%	-2.72%	3.76%	-22.62%	-3.84%	-5.43%	-4.18%	-4.11%	-9.04%
					Starting Viscosity				
$M1_{0.80}$	1492.38	949.61	884.82	245.92	1873.26	942.84	1246.87	649.24	580.47
$M1_{0.95}$	1413.41	373.16	793.39	245.92	1771.59	920.31	1214.58	610.2	566.7
$M2_{0.80}$	1562.5	419.51	875.36	317.51	1955.95	998.1	1319.68	679.2	634.5
$\frac{M1_{0.80} - M1_{0.95}}{M1_{0.80}}$	-5.29%	-60.70%	-10.33%	0.00%	-5.43%	-2.39%	-2.59%	-6.01%	-2.37%
$\frac{M1_{0.80} - M2_{0.80}}{M1_{0.80}}$	4.70%	-55.82%	-1.07%	29.11%	4.41%	5.86%	5.84%	4.61%	9.31%
					Ending Viscosity				
$M1_{0.80}$	1.14×10^6	2.17×10^5	1.04×10^5	2.23×10^3	3.14×10^{10}	4.27×10^4	2.74×10^6	1.20×10^5	7.79×10^6
$M1_{0.95}$	2.98×10^5	2.26×10^7	5.88×10^4	8.53×10^3	1.13×10^4	3.12×10^5	8.30×10^5	3.60×10^4	1.67×10^4
$M2_{0.80}$	1.32×10^5	1.63×10^4	2.98×10^4	1.12×10^4	1.82×10^7	1.92×10^6	9.82×10^8	1.73×10^6	5.26×10^4

3.4 VISCOSITY

Results for viscosity are separated into starting viscosity and ending viscosity as shown in Table 6. Model $M1_{0.80}$ starting viscosities have very little variation covering a range of $2.46\times10^{2}-1.87\times10^{3}$ Pa-s. Figure 12 shows that the Model 1 Ending Viscosity covers a much larger range of $2.23\times10^{3}-3.14\times10^{10}$ Pa-s than the staring viscosity and even the largest literature range of $1.40\times10^{2}-5.60\times10^{6}$ Pa-s taken from Moore et al. (1978). The large discrepancy in ending viscosity can be attributed to differences in starting phenocryst content as Flow 5 has the lowest viscosity at 2.23×10^{3} Pa-s and lowest starting phenocryst content compared to Flow 6 which has the highest viscosity in the study and the highest starting phenocryst content. Further discussion of this outlier will appear latter in this study as it deals with limitations of the FLOWGO model. Eliminating this maximum value brings the Model $M1_{0.80}$ maximum viscosity to 7.79×10^{6} Pa-s which is very similar to the value from Moore et al. (1978) and within the range of maximum values found in Table 8.

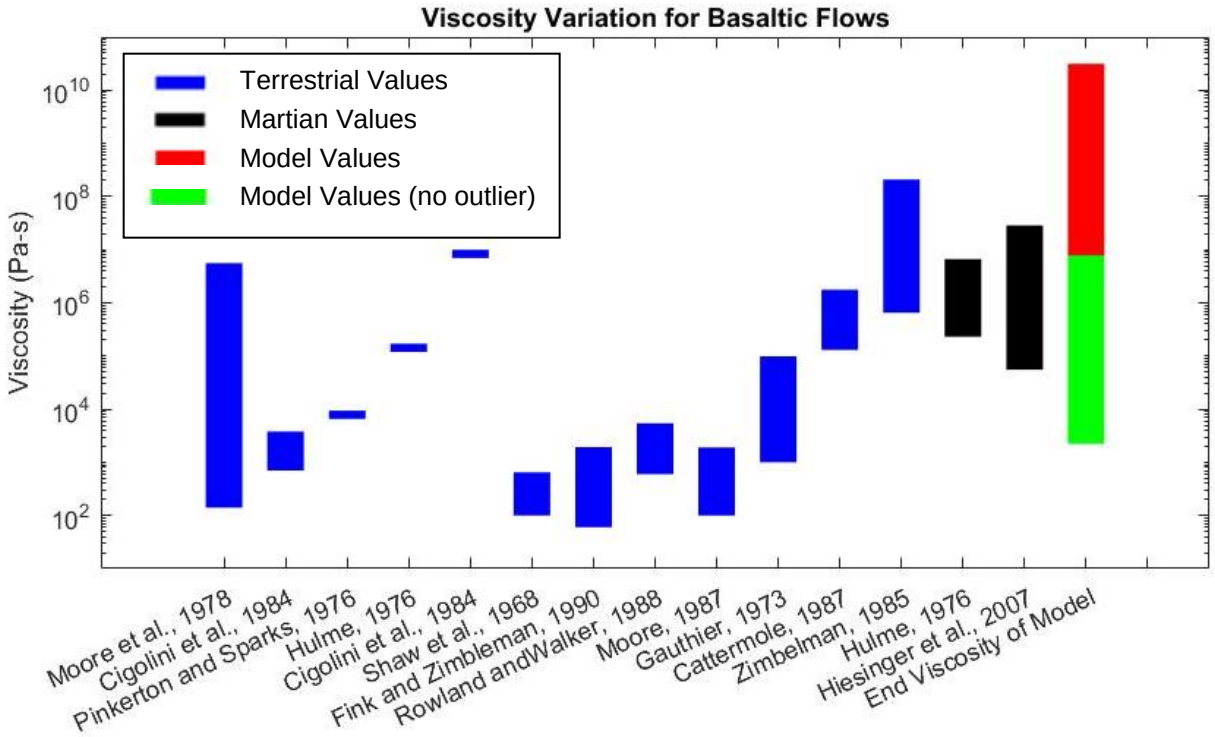

Figure 12: Figures summarizing the viscosity of Model $M1_{0.80}$ and literature values.

Table 8: Summarization table for basalt flow viscosity estimates from specified literature and model results.

Reference	Location	Min Viscosity (Pa-s)	Max Viscosity (Pa-s)
Moore et al., 1978	Mauna Loa, Hawaii	1.4×10^2	5.6×10^6
Cigolini et al., 1984	Makaopuhi, Hawaii	7.0×10^2	4.5×10^3
Pinkerton and Sparks, 1976	Mount Etna, Italy		9.4×10^3
Hulme, 1976	Mauna Loa, HI		1.7×10^5
Cigolini et al., 1984	Arenal, Costa Rica		1.0×10^7
Shaw et al., 1968	Kilauea (Makaopuhi)	6.5×10^2	7.5×10^2
Fink and Zimbleman, 1990	Kilauea (Pu'u 'O'o)	6.0×10^1	2.0×10^3
Rowland andWalker, 1988	Kilauea (pahoehoe)	6.0×10^2	6.0×10^3
Moore, 1987	Mauna Loa (1984)	1.0×10^2	2.0×10^3
Gauthier, 1973	Etna (1971)	1.0×10^3	1.0×10^5
Cattermole, 1987	Alba Patera, Mars	1.3×10^5	1.9×10^6
Zimbelman, 1985	Ascraeus Mons, Mars	6.5×10^5	2.1×10^8
Hulme, 1976	Olympus Mons, Mars	2.3×10^5	6.9×10^6
Hiesinger et al., 2007	Ascraeus Mons, Mars	5.52×10^4	2.86×10^7
End Viscosity of Model	Daedalia Planum, Mars	4.4×10^3	3.10×10^{10}

3.5 VARIABLE SENSITIVITY

Six variables were adjusted in a separate set of model runs to determine how each variable effect the resulting modeled flow length and effusion rate. Figure 14 shows a general summary of the effect each variable had with only changes in slope and eruption temperature having a positive correlation with flow length and eruption rate.

The eruption temperature is the most important variable as it has the strongest correlation with both eruption rate and flow length. Increasing the eruption temperature from 1050 to 1110 (5.71% increase) will cause the eruption rate to more than double and the flow length to more than triple as shown in Table 10 and Figure 13. Figure 13 shows that the relationship between these variables is almost perfectly linear with flow length being more strongly affected by changes in eruption temperature than eruption rate.

Table 9: Summary table of the relationship between selected variables and resulting model outputs of flow length and eruption rate. Values given mean that an increase of 1 for the input variable will cause the designated change in the dependent variable (flow length or eruption rate). These relationship values are based on the slope of a linear best fit line shown in figures 13 and 15-18.

Input Variable	Flow Length	Eruption Rate
Phenocryst Content	1 to -0.44	1 to -0.31
Crust Temperature	1 to -0.71	
Eruption Temperature	1 to 73.2	1 to 48.8
Emissivity	1 to -1.1	
Vesicularity	1 to 0.024	
Average Slope	1 to 1.12	1 to 1.12

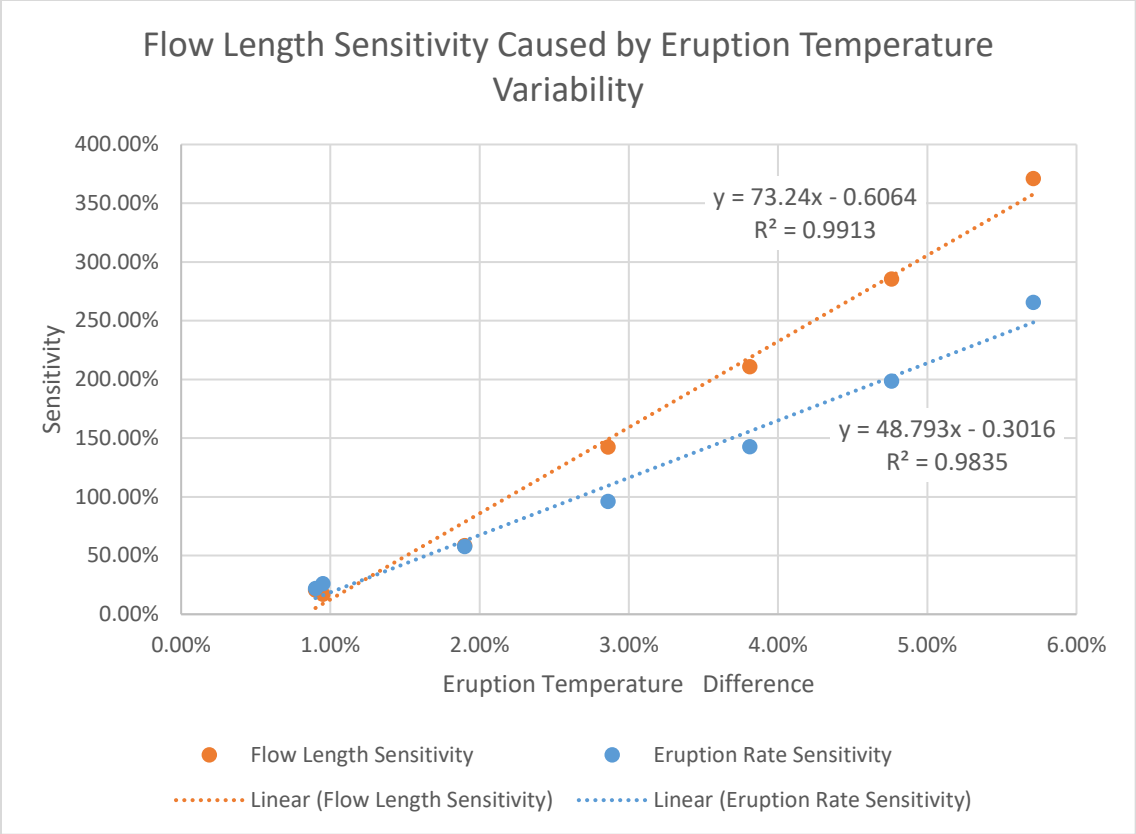

Figure 13: Plot showing the sensitivity of flow length and eruption rate to changes in eruption temperature. Plot includes the linear fit line and equation for each relationship.

Emissivity has the second greatest effect on a flows length as Table 9 shows that an increase of 10.00% in emissivity causes a -11.64% decrease in flow length. Figure 15 shows that emissivity has almost a perfect linear relationship with flow length. The strong relationship shown by this part of the study indicates that determining the appropriate value for emissivity is important for accurate modeling of lava flows.

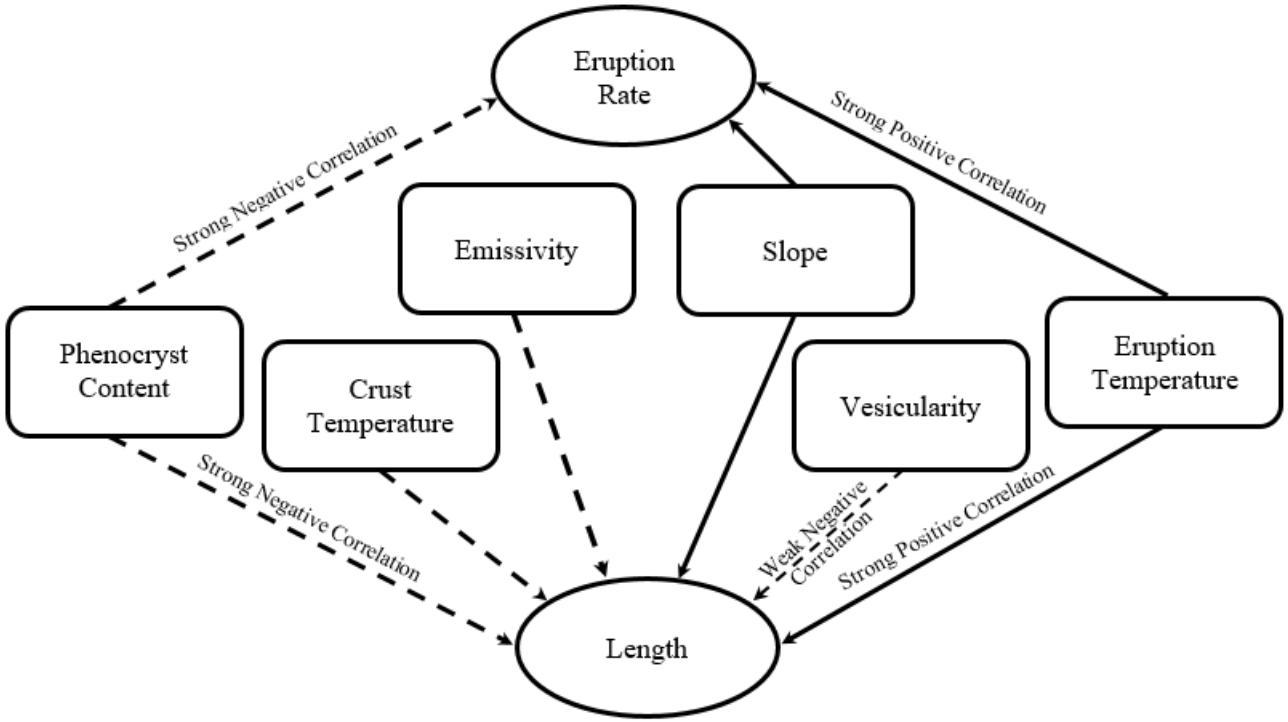

Figure 14: Characterization of relationship between selected variables and resulting modeled length and eruption rate. Relationship arrows start from the impute variable and point towards the subsequent dependent result. Negative correlations indicate an increase in the impute variable will cause a decrease in the dependent.

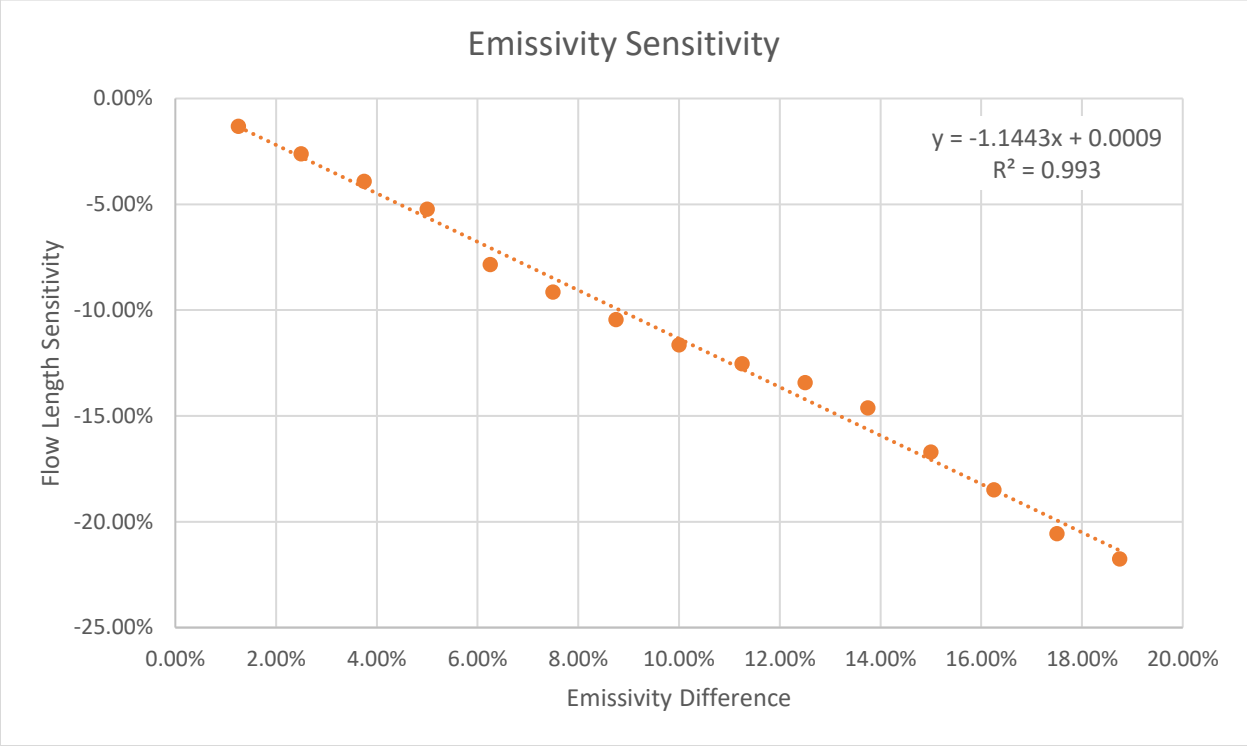

Figure 15: Plot showing the sensitivity of flow length to changes in emissivity. Overlaid on the plot is the linear fit line and equation for this relationship.

Model analysis shows that an increase in crust temperature causes a decrease in flow length due to its negative correlation. The analysis shows that doubling the crust temperature (300°C to 600°C) will cause a decrease in the flow length by about 70% (Table 10 and Figure 16).

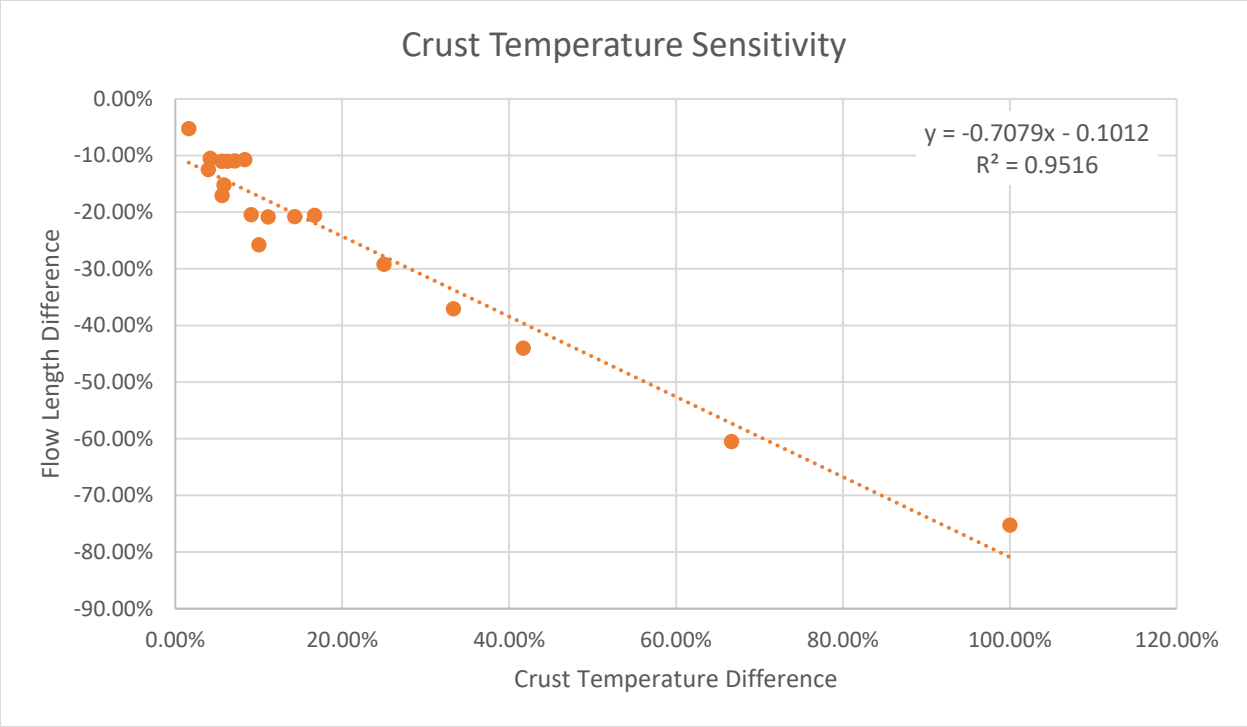

Figure 16: Sensitivity of flow length plotted against changes in crust temperature. Overlaid on the plot is the linear fit line and equation for this relationship in the upper right corner.

Changes in phenocryst content causes strong negative change in both flow length and eruption rate. An increase in phenocryst content of 10% has been modeled to cause a decrease in eruption rate of 5.88% and a decrease in flow length of 8.64%. Phenocryst content is the most important impute variable for this study as it is varied in order to produce the best-fit model. The problem with phenocryst content is that as Figure 17 indicates it does not have a strong linear relationship with flow length and eruption rate. Phenocryst content is related to both viscosity and yield strength and the inclusion in these two terms (with exponents) causes the velocity to have a complex (non-linear) relationship based on Equation 2.

Model analysis shows only a slight positive correlation between increases in vesicularity and an increase in flow length. Increasing the vesicularity from 10% to 90% (an 800% increase) causes only a 9% increase in flow length.

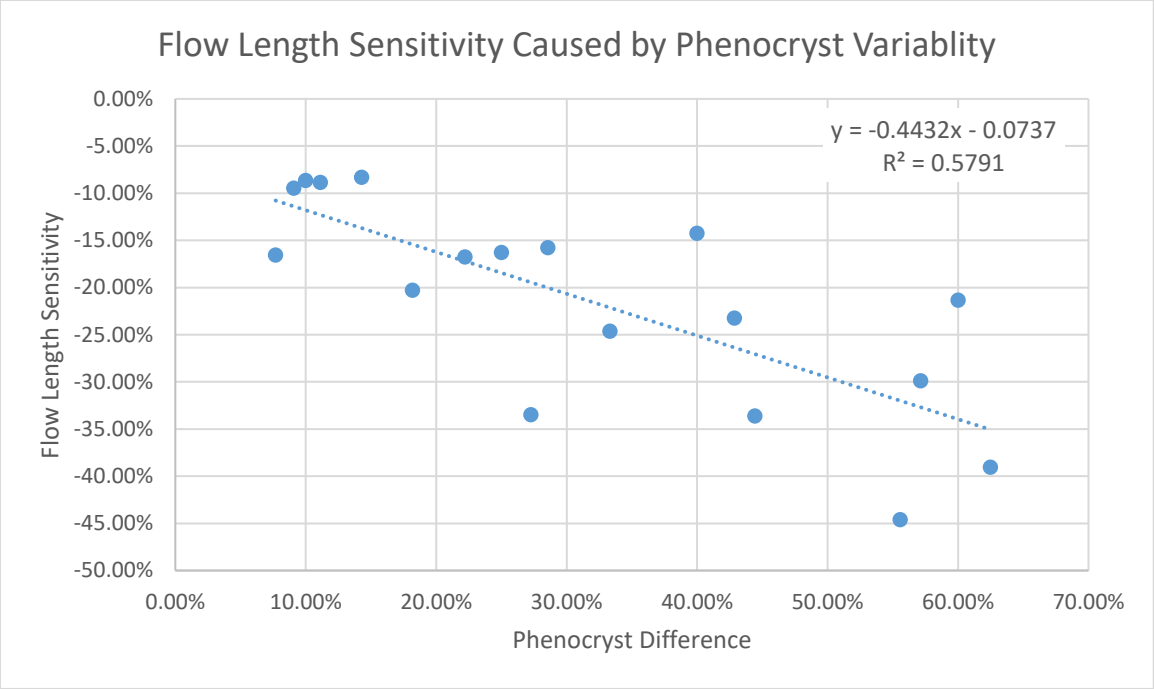

Figure 17: Plot showing the sensitivity of flow length to changes in phenocryst content. Overlaid on the plot is the linear fit line and equation for this relationship.

Table 10: Table summarizing chosen data sets from sensitivity analysis of chosen variables.

Phenocryst Sensitivity		
	Difference in Value	Sensitivity
Phenocryst	0.010	10.00%
Eruption Rate	-57.32	-5.88%
Flow Length	-8.00	-8.64%
Phenocryst	0.02	25.00%
Eruption Rate	-116.75	-10.70%
Flow Length	-18	-16.28%

Crust Temperature Sensitivity		
	Difference in Value	Sensitivity
Tcrust	200	66.67%
Eruption Rate	0	0.00%
Flow Length	-209	-60.49%
Tcrust	300	100.00%
Eruption Rate	0	0.00%
Flow Length	-260	-75.24%

Eruption Temperature Sensitivity		
	Difference in Value	Sensitivity
Terupt	60	5.71%
Eruption Rate	577.35	265.56%
Flow Length	99.67	370.93%

Emissivity Sensitivity		
	Difference in Value	Sensitivity
Emissivity	0.15	18.75%
Eruption Rate	0	0.00%
Flow Length	-16.65	-21.75%

Vesicularity Sensitivity		
	Difference in Value	Sensitivity
Vesicularity	0.8	800.00%
Eruption Rate	0	0.00%
Flow Length	29	8.96%

Slope Sensitivity		
	Difference in Value	Sensitivity
Avg. Slope	0.1	25.00%
Eruption Rate	195.05	26.80%
Flow Length	13.43	28.63%

Model analysis has shown that minor variations in the slope cause a significant impact on flow length and eruption rate (Figure 18). One example shows that changing all slope points to be equal to the flow path's average slope increases flow length by 15.4% and eruption rate by 45.1%. Changing the average slope value by 25% will cause a 28.6% increase in flow length and a 26.8% increase in eruption rate. This relationship is related to the inclusion of slope in Equation 2 which is used to calculate the flow velocity at each increment step so any variation along the slope path will change the flow rate at that step. This relationship was further examined by including two sections 2.5 km long of with a shallow slope (0.1°) separated by varying distances. Figure 18b shows that the greater the separation distance the shorter the modeled flow length. A less direct relationship involves the step size between slope data points and subsequent model results.

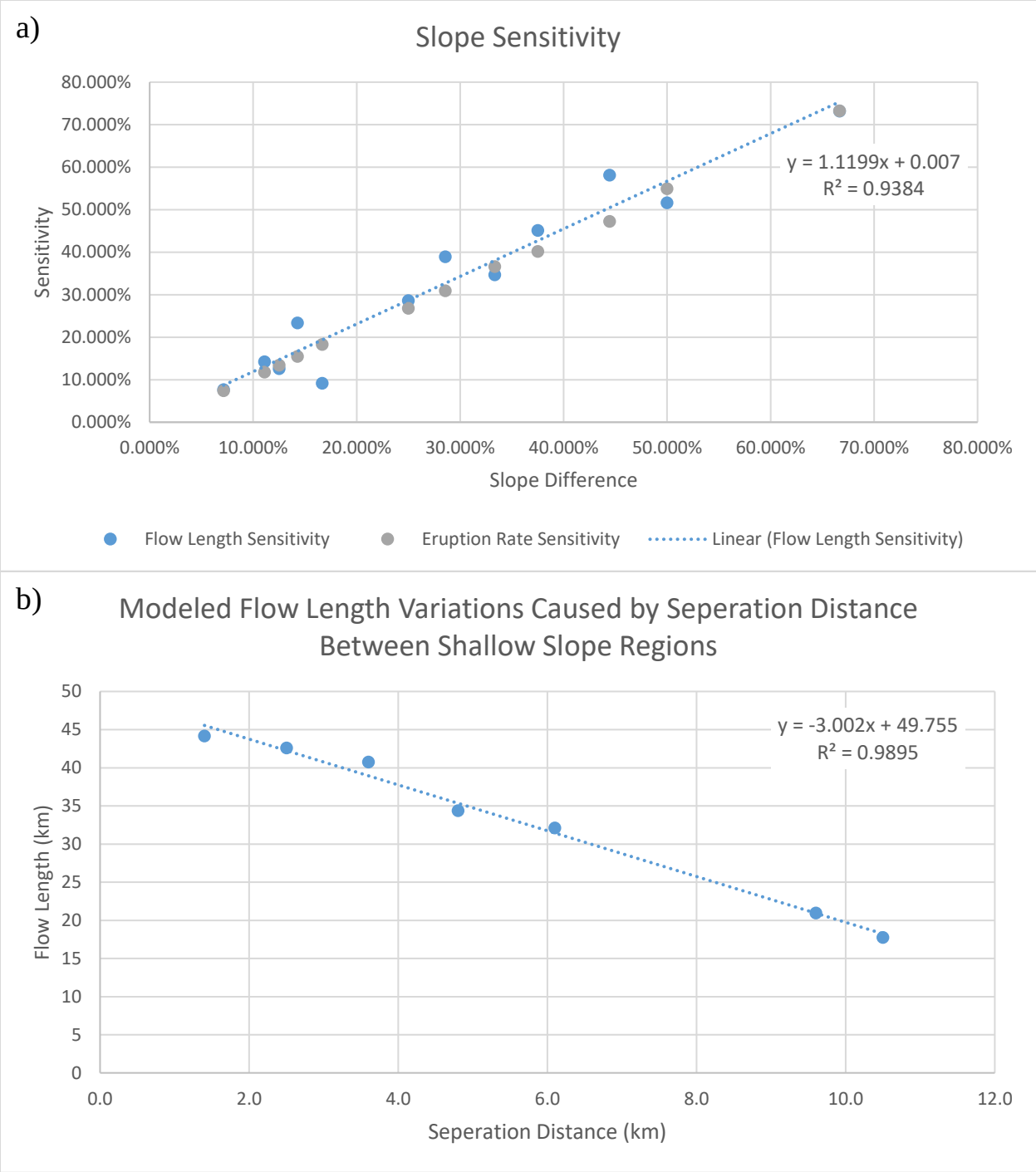

Figure 18: a) Plot showing the sensitivity of flow length and eruption rate to changes in average slope. Overlaid on the plot is the linear fit line for only flow length and the equation for this relationship. b) Plot showing how modeled flow length is effected by the separation distance between two regions of shallow slope.

The distance between slope points determines how finely the topography of the region is simulated in the model. The initial step size of 228 m for Flow 3 was determined by separating the distance of a slope line along the flow's path into 301 equally distanced apart. The effects of step size was determined by separating the line into points by a set distance (step size) starting with 300 m for a small increase. Larger step size increases were done by doubling (484 m) and tripling (684 m) the original step size. The larger the step size the smoother the surface used in the model but Figure 19 shows that even tripling the step size has only a limited effect on the path slope. Table 11 shows this small variation in slope has limited effect on the final model results. This limited effect is a result of the slope data being provided from the gridded DEM that has already smoothed the topographic variations.

Table 11: Summary table of the model results for Flow 3 at different step sizes based on the distance between slope data points. A step size of 228 m was used for the original model runs.

Step Size (m)	228	300	456	684
Measured Length (km)	71.72	71.72	71.72	71.72
Modeled Length (km)	72.54	73.1	75.944	70.72
Flow Length Difference	1.14%	1.92%	5.89%	-1.39%
Eruption Rate (m3/s)	15,701.56	15,610.73	15,610.73	15,159.31
Width (m)	149.55	149.55	149.55	149.55
Depth (m)	13.8	13.8	13.8	13.8
Crust Temperature (°C)	625	625.00	625.00	625.00
Phenocryst Content	10.90%	11.0%	11.0%	11.5%
Emissivity	0.8	0.8	0.8	0.8
Ave. Slope	0.64	0.642	0.638	0.6421
Beginning Viscosity	949.61	408.470	408.470	419.110
Ending Viscosity	2.17×10^5	2.67×10^4	1.96×10^4	1.35×10^4

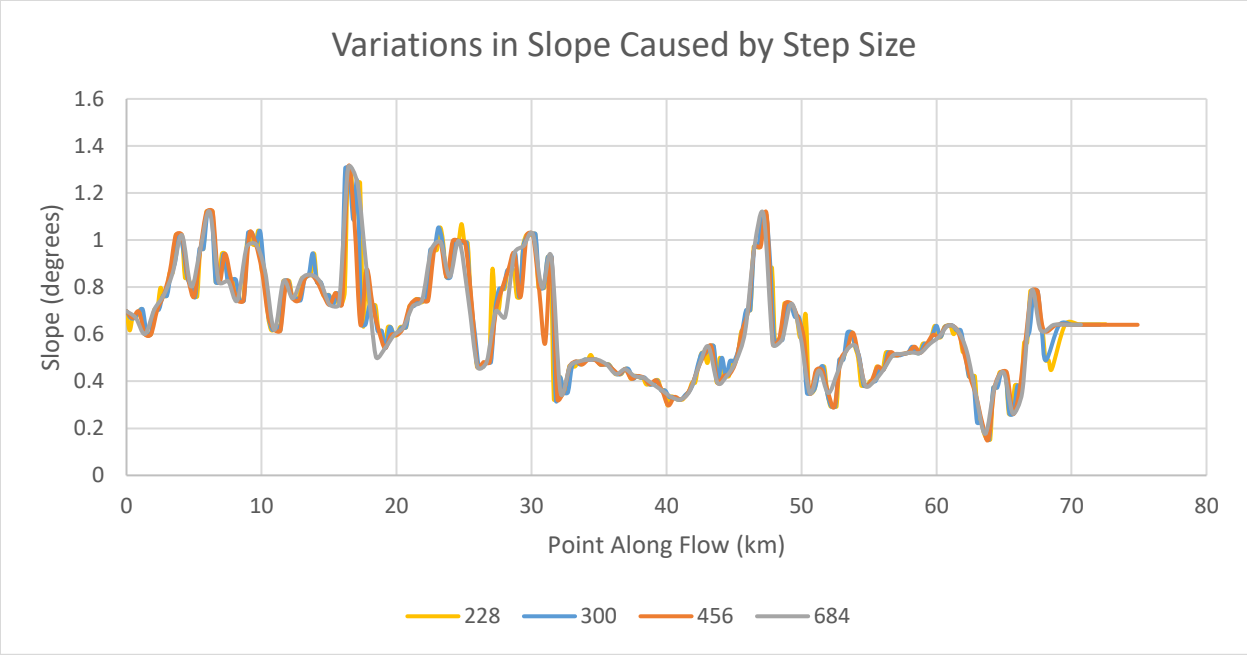

Figure 19: Figure of the change in slope over flow length caused by variations in step size. Legend gives the step size in meters.

3.5.1 Model Comparisons

The two secondary models $M1_{0.95}$ and $M2_{0.80}$ provided a method for comparing the final results with variations in model settings. Changing the emissivity value to 0.95 ($M1_{0.95}$) caused varying changes to the model results. This increase in emissivity caused a decrease in both the required starting phenocryst content and starting viscosity for all flows except Flow 5 (Table 6 and 7). Figure 20 shows that the variation in modeled flow length and starting phenocryst content are minimal. For example, the phenocryst change for Flow 3 was only 1.70%. Flow 5 is unique as changes in models required a change in the crust temperature in order to match the flow length leading to the larger variation in model results. The starting viscosity shows a much greater variation in change with Flow 3 decreasing by -60.70% but rest of the flows having an average decrease of 4.30%. The eruption rate of the all flows except for Flow 5 increased by as little as

2.81% to a maximum of 15.76%. The final viscosity shows no distinct inclination to decrease or increase for model $M1_{0.95}$ compared to model $M1_{0.80}$.

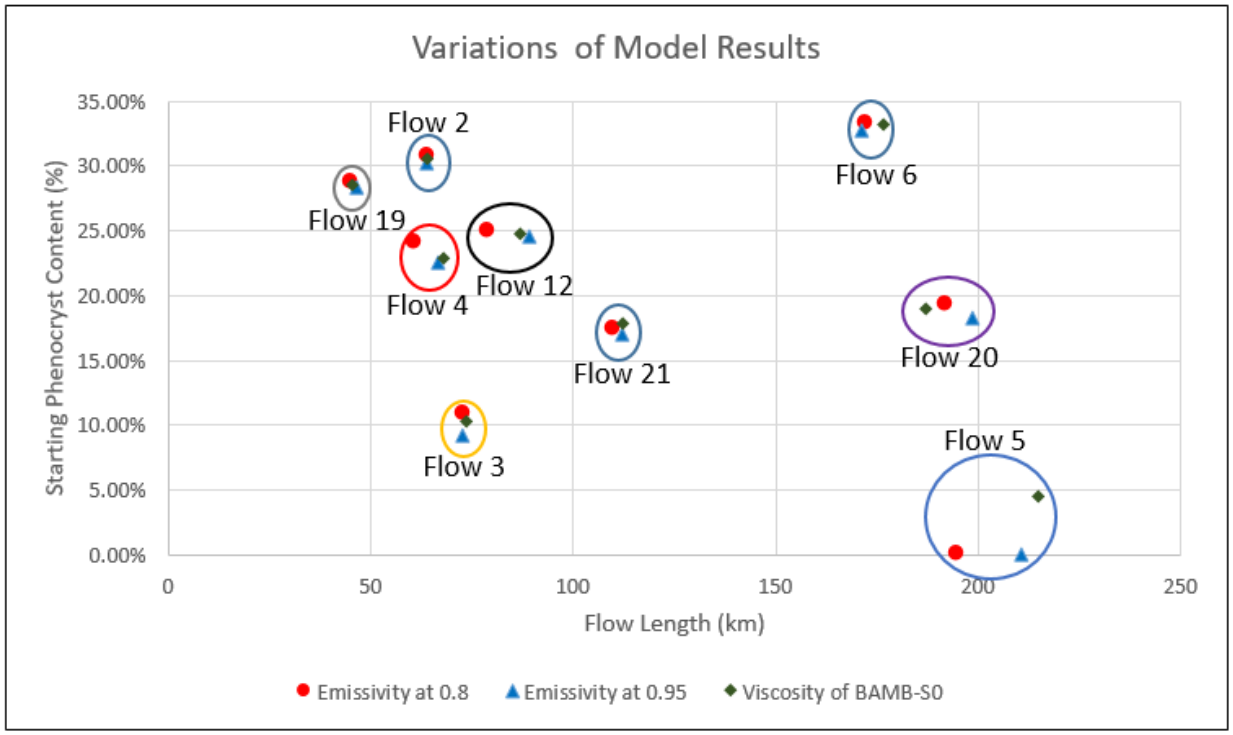

Figure 20: Figure summarizing variations in modeled flow length and best-fit starting phenocryst content depending on the model used.

Model $M2_{0.80}$ has the same parameters as $M1_{0.80}$ except that the viscosity model is changed to the Mars specific parameters of BAMB-S0. Overall this change has similar effects as the change to the model $M1_{0.95}$ with a minimal decrease in phenocryst content. One difference is that the eruption rate in this case is decreased by an average of -5.81% with Flow 5 being an outlier at -22.62%. The change in viscosity model caused an overall increase of starting viscosity of 7.85% with the exclusion of the -55.82% for Flow 3.

Visual comparison of Figure 21a shows that the various changes in models examined in this study cause only small variations in eruption rate. A comparison to Figure 21b shows that

viscosity has a large variation in value across models. This variation is not model specific as the figure only shows that variation in values and not which value belongs to which model.

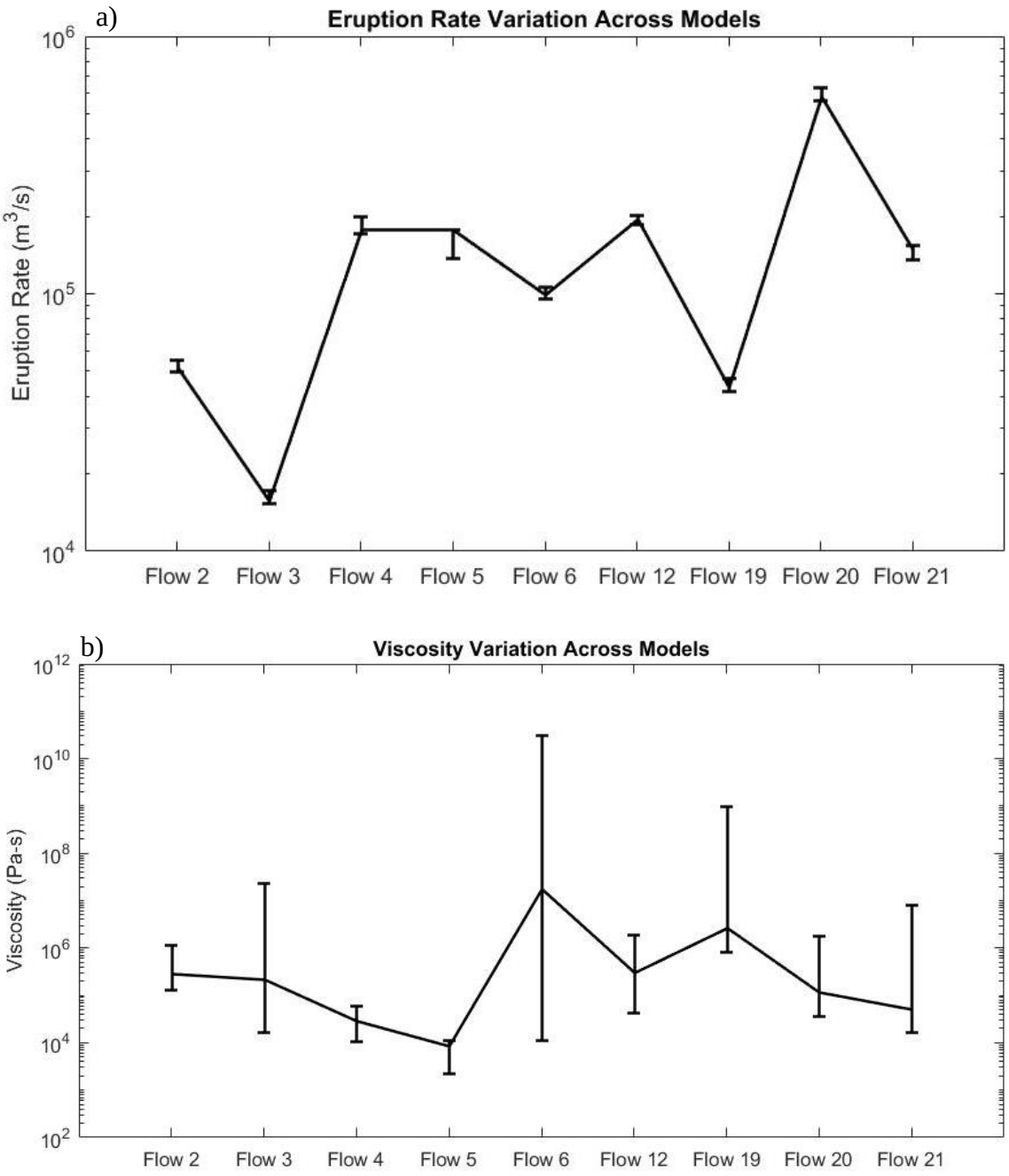

Figure 21: Figures summarizing variations in modeled flow length (18a) and viscosity (18b) across the Models $M1_{0.80}$, $M1_{0.95}$, and $M2_{0.80}$. Error bars in figures depict variation of values for each flow and do not correspond to the model used.

4.0 DISCUSSION

The model results presented in this study rely on the chosen values inputted into the model with most parameters taken from terrestrial analog data presented in Table 12 of Appendix A. The eruption temperature value used in the study was maintained at 1114°C as it represented a reasonable average value already provided for in the original data set for Piton de la Fournaise taken firm Harris et al., 2015. The sensitivity analysis section showed the importance of this value and thus any change to it will cause substantial alterations to the model results. This value was maintained as it an approximate average value compared to the ranges given for other basaltic volcanoes such as Kilauea which ranges from 1130-1150°C and Etna with a range of 1070-1190°C and the lack of countering data for Martian flows (Harris and Rowland, 2015 and reference therein found in table 17.2). By comparison crust temperature value for this study was determined not only by analog data but by the range of possible emissivity values and a constant phenocryst content and a set of model runs for this study.

The value determined in this study relies on the choice of flow used in the model runs and the constant phenocryst value chosen. The subsequent use of this value must take this into consideration as changing either value in the model run for this determination will change the subsequent average crustal temperature value. Flow 3 was chosen for this process as it had the thinness thickness and thus easiest to model to the measured flow length. Phenocryst content was chosen as the rounded value from the original data set value of 10.4%. The resulting value 625° C

was accepted for the study as it was within the range of values from terrestrial research (390-770°C taken from Flynn & Mouginis-Mark 1994). As sensitivity analysis shows a decrease in this value will cause a subsequent increase in flow length which was required for the modeling of Flow 5 for models $M1_{0.95}$ and $M2_{0.80}$.

Phenocryst content was an important variable/parameter determined for each flow in this study as it was the only one varied in between flows within each model run. The results of Model $M1_{0.80}$ show that flows into Daedalia Planum require phenocryst content that ranges from 0 to 33.3% which is a reasonable range when compared to terrestrial data. This range is nearly identical to the range shown for Kilauea which is 0-30% (Harris and Rowland, 2015b). The problem with this model result is that the higher the starting phenocryst content the more viscous the flow should be and the shorter its overall length. This irregularity is exemplified by Flow 6 which has the highest phenocryst content is also fairly long at 174.54 km. This contradiction can impart be explained by differences in planetary constants such as gravity but can also be attributed to flow specific parameters such as flow thickness and path slope. Flow 6 has the greatest thickness and also one of the highest average path slopes of all flows in this investigation. The combination of these values gives the flow a high starting velocity of 16.13 m/s compared to the 7.61 m/s for Flow 3 which is the thinnest flow.

The resulting eruption rate and viscosity values from this study show a definite similarity to previous study results. For example, the eruption rate results shown in Figure 11 and the viscosity range in Figure 12 fall within the higher range of previous results. Eruption rate values compared to the modeled values here come from previous research that only used an empirical relationship to determine eruption rate from dimensional values of Martian flows such as area, length, width and slope rather than as part of a flow model study. As a method for direct

comparison, eruption rate was calculated using the Graetz number method but produced a value only one eightieth the maximum eruption rate for the modeled flow's. This large discrepancy in values for the same flows can be attributed to the different methods in which eruption rates were calculated between the two methods. The Graetz number method relies on a relationship between eruption rate and the cooling of the flow while the modeled eruption rate is determined from the area of the channel and the calculated flow velocity. The similarity in this study's results and previous results indicates that these results accurately depict the rheological values for Martian flows in the Daedalia Planum.

4.1 STUDY LIMITATIONS

This study was performed with limited direct Martian data which includes the flow length measurements. The measured flow length only gives the minimum length of the flow as the starting point of the flow cannot easily be identified with the newer flows overlying points of older flow as shown in Figure 22. A second method to examine the accuracy of the model is to compare the measured channel width to the modeled values as shown in Figure 23. There is a strong correlation shown in this figure for the first two thirds of the flow length but breaks down at the end of the flow. The setup of the model causes the width of the flow to change as the velocity decreases to maintain a constant eruption rate. This setup makes it so that at the end of the flow the final part of the modeled flow to be overly wide compared to the measured values as the velocity nears zero. The velocity of the flow at each step is directly related to the slope at that step as shown in Figure 24 so any large variations in slope will have a corresponding effect on channel width.

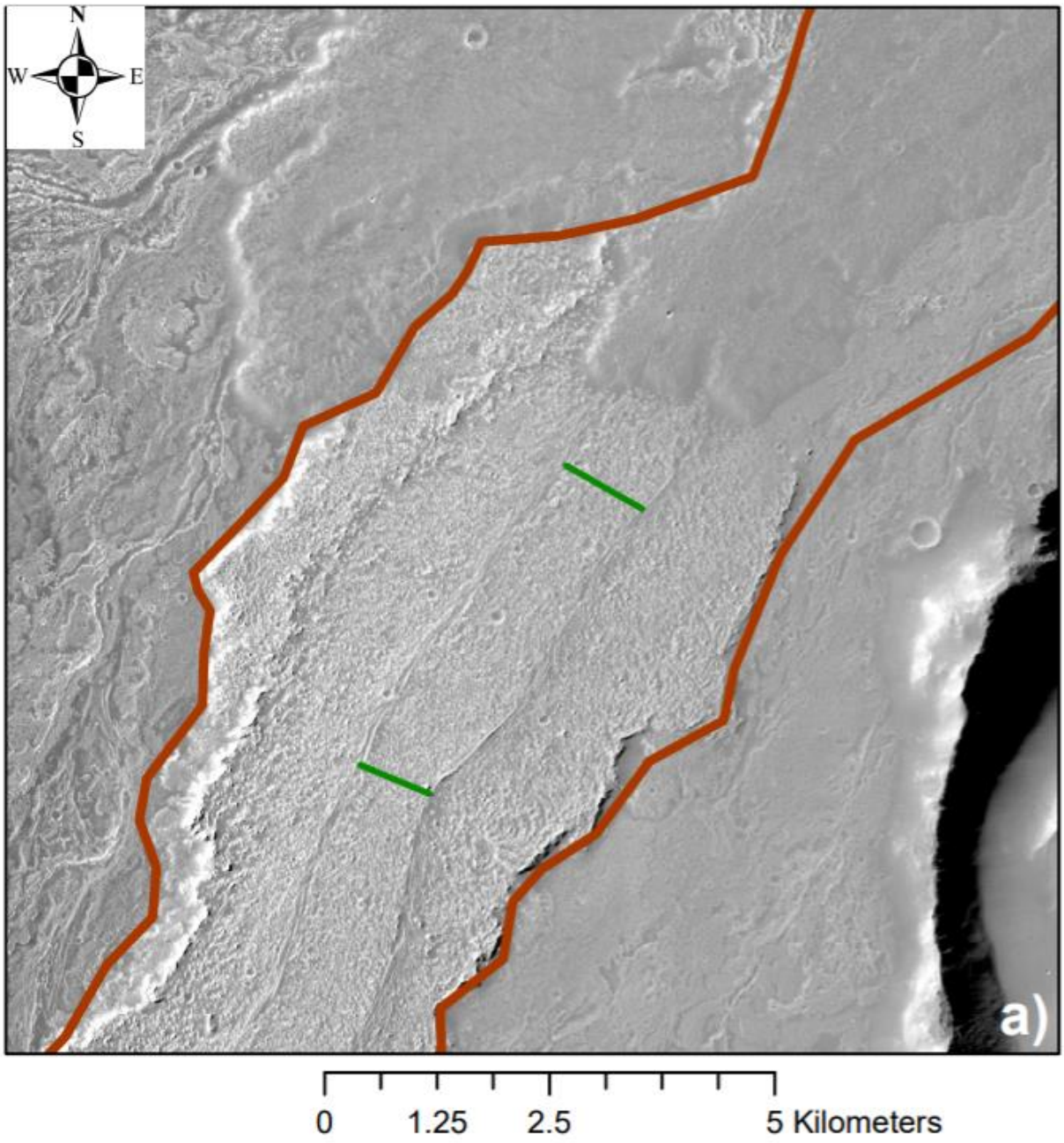

Figure 22: Subset of CTX image of Flow 20 showing how a newer flow has flowed over and covered the beginning section of the flow. This figure is part a) subset of Figure 40 in Appendix B.

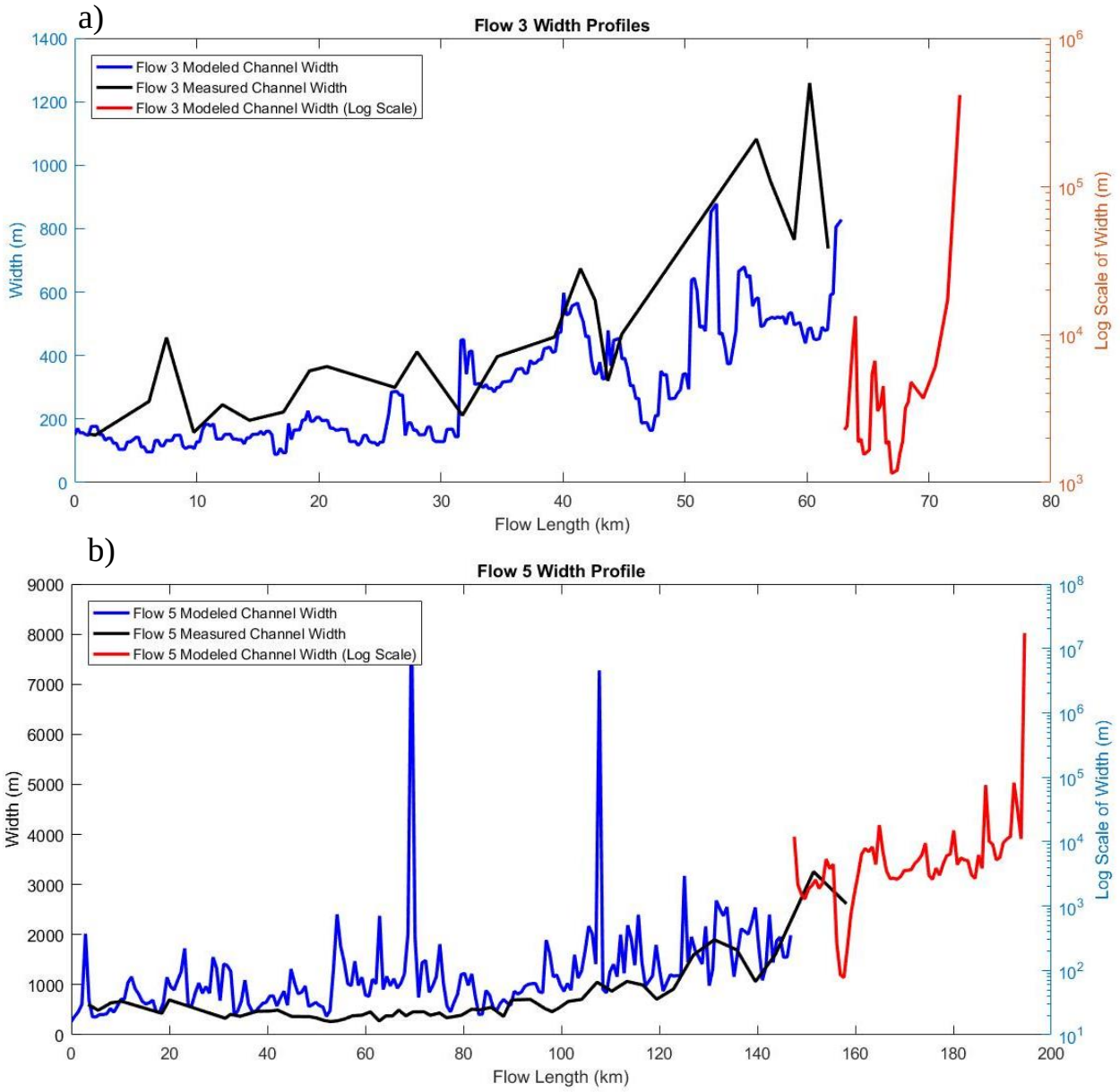

Figure 23: Figure showing the measured and modeled channel widths for Flow 3 (20a) and Flow 5 (20b) along its length. The end of the modeled flows were separated into log scale for clarity.

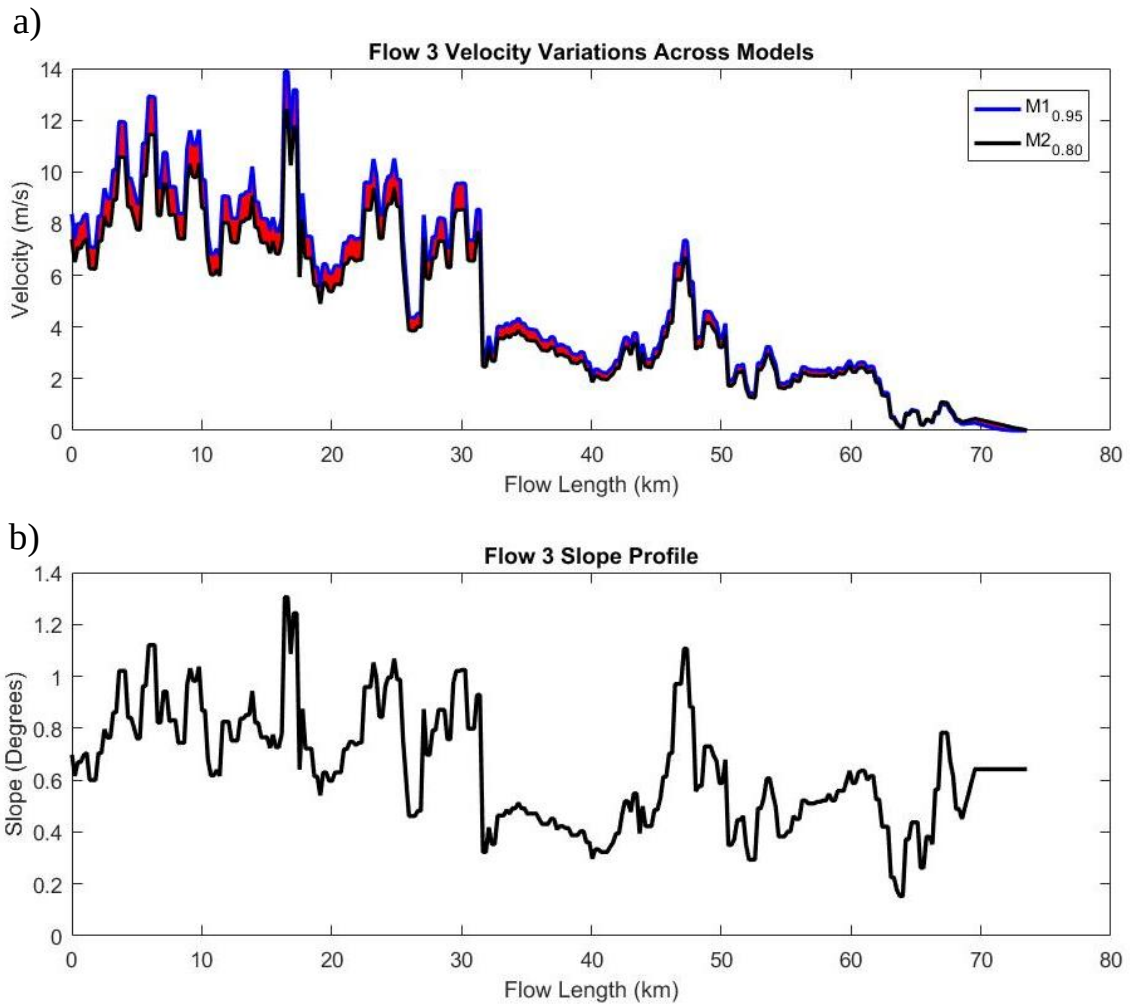

Figure 24: Figure showing the changes in flow velocity (22a) and path slope (22b) along the flow length.

One limitation to FLOWGO only stops the flow when the velocity reaches zero or when the core temperature is below the solidus without considering if it is rheologically possible for the final flow to exist (Harris and Rowland, 2015). Reexamination of the Flow 6 results show that this result occurs with a total crystal content of $1.4 \times 10^6\%$ which is not physically possible. This high crystal content can explain the high viscosity for this flow. This result fit the measured flow length best but a limitation for the resulting total crystal content would excluded it.

5.0 CONCLUSION

This study has shown that channelized flows in Daedalia Planum can be modeled by FLOWGO with a high degree of accuracy. Flows in the region required a phenocryst content of 0-33.3%, which is in the range of terrestrial basalt flows. This study resulted in eruption rates that ranged from $1.52\times10^{3}-6.27\times10^{5}$ m^3/s and a viscosity range of $2.23\times10^{3}-3.14\times10^{10}$ Pa-s. These are fell within the range of previous studies for Martian flows. Flow 6 had a higher than expected viscosity caused by limitations in the model. This study also showed that changing emissivity, the viscosity model and slope step did not strongly influence the model results.

Using the results from this study, inferences on differences in the volcanism in the region can be made. Based on differences in the best-fit starting phenocryst content, the region can be separated into the following three groups: flows 3 and 5, flows 20-21, and flows 2, 4, 6, 12, and 19. These groups may represent variations in composition caused by the source or age of eruption. These groups do not provide evidence for regional variations in volcanism as there is little to no spatial relationship (proximity) between the flows that make up the groups.

Similar studies such as this can give indications of differences in volcanism in a region that can be compared to visual observations of morphology. This concept can be applied to channelized flows on Mars and other planetary bodies with sufficient data.

APPENDIX A

TABULAR DATA

Table 12: Table of input parameters for Flow 3 best fit model ($M1_{0.80}$). Parameter values taken from Piton de la Fournaise (2010) channel included in Harris et al. (2015) with values for the gravity constant, crust temperature, phenocryst content and flow thickness modified for this study.

INPUT PARAMETERS

Channel Dimensions		
Channel width (w)	m	149.55
Channel depth (d)	m	13.80
Down-flow increment	m	1000
Velocity Constants		
Gravity (g)	m s^{-2}	3.80
Channel Shape (B)		3.00
Viscosity and Yield Strength (YS) Parameters		
Viscosity @ Eruption	Pa s	1000
Constant a	K^{-1}	0.04
Constant b	Pa	0.01
Constant c	K^{-1}	0.08
Radiation Parameters		
Stefan–Boltzmann (σ)	W m^{-2} K^{-4}	5.67×10^{-8}
Emissivity (ε)		0.80
Conduction Parameters		
Thermal conductivity (K)	W m^{-1} K^{-1}	0.88
Basal temperature (T_{base})	C	500
	K	773.15
Core to base distance	%	19
h_{base}	m	2.62

Thermal Parameters		
Eruption temperature (T_{erupt})	°C	1114
	K	1387.15
Crust temperature	°C	625
(Tcrust)	K	898.15
Buffer	°C	135
(T_h=T_{erupt}-Buffer)	K	135
Crust cover (f)		0.60
Core exposure (1–f)		0.40
Crust to velocity relationship (d)		-0.0076
Density and Vesicularity		
DRE Density (ρ_{DRE})	kg m^{-3}	2970
Vesicularity		0.64
Bulk Density (ρ)	kg m^{-3}	1080
Convection Parameters)		
Wind Speed (U)	m s^{-1}	5.00
C_H		0.0036
Air Temperature (T_{air})	C	-54.00
	K	219.15
Air Density (ρ_{air})	kg m^{-3}	0.44
Air Specific Heat Cap ($c\rho_{air}$)	J kg^{-1} K^{-1}	1099
Crystal Parameters		
Phenocryst Content (ϕ)		0.1090
Post eruption xtals ($\Delta\phi$)		0.89
Cooling Range (ΔT)	K	150
Rate of crystallization ($\Delta\phi/\Delta$T)	fractional xtalization per K	0.0059
Latent heat of crystallization (L)	J kg^{-1}	3.5×10^5
R		1.67

Table 13: Viscosity and convection models used in FLOWGO model. Convection model has been modified for Martian atmospheric values.

Temperature dependent viscosity relation of Villeneuve et al. (2008)

$$\log\eta = -4.52 + 5558/(T-582.9).$$

This equation yields 919 K for the standard glass transition temperature, at which the viscosity is 10^{12} Pa s. Static measurements

Check:

Temperature:	919	K
Log(viscosity)	12.02	Pa s
Viscosity	1.04×10^{12}	Pa s

Mars free convection model from Rowland et al. (2004)

Free Convection	**Q_{free}**	**401**	**W/m^2**	
Surface Temperature	Tconv	918	K	
Ambient Air Temp.	Tair	219.15	K	
Thermal Conductivity	alpha	9.4×10^{-3}	W/m	Eqn. A6
Cubic Expansivity	kappa	8.13×10^{-5}	m^2/s	Eqn. A8
Density	dens	14.41	kg/m^3	Eqn. A1
Dynamic viscosity	visc	8.23×10^{-6}	Pa s	
Thermal Diffusivity	beta	0.004563	1/K	
Atmospheric T	T_{atmos}	394.47	Rankine	
Reference T for CO_2	To	528	Rankine	

Values for Martian atmosphere from Appendix A of Rowland et al., 2004			
Constant for CO_2	A	-0.01183	W/m K
Constant for CO_2	B	1.02×10^{-4}	W/m K^2
Constant for CO_2	C	-2.22×10^{-8}	W/m K^3
Thermal Diffusivity	Beta	0.004563	1/T
	v	14.6	
Pressure	P	600	Pa
Ideal gas constant	R	0.19	J/mol K
Reference Viscosity	visco0	1.48×10^{-5}	Pa s
(0.555 x To) + Tamos	a	459	Rankine
(0.555 x To) + To	b	533	Rankine
Sutherland's constant	S	240	Rankine

Table 14: Table of the CTX images used in the study separated by Study Area.

Study Area A	Study Area B
B02_010385_1569_XN_23S125W	B02_010464_1545_XI_25S122W
B08_012798_1573_XN_22S124W	B03_010899_1601_XN_19S119W
B12_014143_1553_XN_24S124W	B12_014367_1576_XN_22S120W
B12_014354_1531_XN_26S124W	B17_016345_1576_XN_22S120W
B17_016332_1563_XN_23S125W	B17_016411_1594_XN_20S122W
B20_017255_1664_XN_13S125W	B20_017479_1604_XN_19S120W
B20_017466_1664_XN_13S126W	D10_030995_1613_XN_18S121W
B20_017611_1624_XN_17S124W	F02_036731_1578_XN_22S122W
B21_017677_1664_XN_13S126W	F04_037298_1588_XN_21S123W
B21_017822_1656_XN_14S125W	F07_038485_1587_XN_21S123W
B21_017888_1638_XN_16S127W	F16_041940_1570_XN_23S122W
D05_029281_1607_XN_19S124W	F16_042006_1570_XN_23S122W
D06_029492_1645_XN_15S126W	F17_042362_1542_XN_25S123W
D10_030995_1613_XN_18S121W	G03_019536_1574_XN_22S119W
D12_031839_1545_XI_25S125W	G05_020314_1608_XN_19S120W
D14_032617_1605_XN_19S125W	G06_020525_1601_XN_19S120W
D20_035096_1544_XN_25S125W	G09_021659_1579_XN_22S120W
D21_035518_1553_XN_24S127W	G10_022226_1603_XN_19S121W
F01_036085_1588_XN_21S126W	G14_023782_1621_XN_17S122W
F03_036863_1554_XN_24S126W	G16_024560_1578_XN_22S120W
F05_037641_1569_XN_23S127W	G18_025061_1602_XN_19S119W
F16_041861_1575_XN_22S125W	G23_027105_1598_XN_20S122W
F17_042573_1571_XN_22S126W	G23_027171_1572_XN_22S123W
F18_042995_1570_XN_23S126W	P01_001524_1569_XN_23S122W
G03_019378_1661_XN_13S127W	P01_001590_1567_XN_23S122W
G04_019879_1667_XN_13S125W	P03_002078_1568_XN_23S121W
G11_022358_1640_XN_16S125W	P04_002500_1563_XI_23S122W
G15_024125_1596_XN_20S125W	P04_002711_1560_XN_24S122W
G18_025259_1604_XN_19S125W	P05_002856_1568_XI_23S121W
G18_025325_1607_XN_19S127W	P06_003278_1582_XN_21S122W
G19_025615_1631_XN_16S124W	P11_005190_1590_XI_21S122W
G22_026736_1585_XN_21S128W	P11_005401_1541_XN_25S122W
P02_001854_1636_XN_16S126W	P13_006258_1616_XN_18S121W
P02_001999_1639_XN_16S125W	P14_006469_1605_XN_19S122W
P03_002065_1572_XN_22S126W	P14_006614_1597_XI_20S121W
P03_002210_1632_XN_16S125W	P16_007471_1586_XN_21S121W
P04_002487_1597_XN_20S127W	P17_007537_1539_XN_26S122W
P04_002777_1634_XN_16S125W	P17_007616_1634_XN_16S121W
P05_002843_1553_XN_24S126W	P18_008038_1544_XN_25S123W
P06_003555_1604_XN_19S125W	P19_008473_1537_XN_26S121W
P07_003621_1585_XN_21S126W	
P07_003766_1639_XN_16S126W	

P08_004188_1622_XN_17S127W
P09_004399_1543_XN_25S126W
P11_005177_1606_XN_19S127W
P11_005322_1623_XN_17S126W
P12_005533_1533_XN_26S126W
P12_005757_1637_XN_16S123W
P12_005889_1598_XN_20S126W
P13_006192_1602_XN_19S119W
P13_006258_1616_XN_18S121W
P17_007616_1634_XN_16S121W
P17_007669_1542_XI_25S126W
P17_007748_1554_XN_24S124W
P17_007814_1543_XN_25S126W
P18_008170_1592_XN_20S128W
P18_008249_1632_XN_16S125W
P19_008328_1638_XN_16S123W

Table 15: Table of the eruption rates from literature search and designated models.

Source	Eruption Rate (m^3/s)		Location	Background Information
	Minimum	Maximum		
Rowland and Walker, 1990	averaged at ~5 for 1983-1990	4.0×10^2	Kilauea, Hawaii	Historic Hawaiin Eruptions
Thordarson and Self, 1993		$\sim 9 \times 10^3$	Iceland	1783-1785 Islandic Laki eruption Fissure eruptions
Walker, 1973		$\sim 10^6$	Mars	Assumes Hawaiian emplacement conditions and empirical relationship between flow length and eruption rate.
Pieri and Baloga, 1986	9×10^2	10^6	Mars	Used 1983 Kilauea eruptions data $E_r \propto Q/A$
Kilburn and Lopes, 1991	10^5	4×10^6	Mars	Uses a variety of flows and not only Hawaiian style
Pinkerton and Wilson, 1994	6.0×10^2	2.0×10^3	Mars	Used the Gratz number based on the assumption that the flow is stopped only by conductive heat loss.
Pinkerton and Wilson, 1988	4×10^4	2×10^8	Mars	(volume/length $\times$ height)^3 Flows must be volume limited
Zimbelman, 1998	5×10^4	1.1×10^6	Mars	Jeffreys equation used to determine the velocity of the lava flow as a Newtonian fluid
Hulme, 1976		4.7×10^2	Olympus Mons, Mars	Flow of a Bingham fluid down an inclined plane leveed flow on Olympus Mons.
Lopes and Kilburn, 1990	7.0×10^2	10^5	Alba Patera, Mars	Empirical relations derived for simple flows on Earth 18 flows on Alba Patera
Kilburn and Lopes, 1991	9×10^2	10^6	Mars	Hawaii style flows used in empirical relationships.
Cattermole, 1987	1.55×10^2	5.85×10^3	Alba Patera, Mars	Used a linear relationship between yield strength and viscosity for Alba Patera, Mars
Hiesinger et al., 2007	2.3×10^1	4.04×10^2	Ascraeus Mons, Mars	Gratz number method
Hauber et al., 2011	2.0×10^1	4.30×10^4		Gratz number method
Vauncher et al., 2009	4.5×10^4	1.15×10^5	Central Elysium Planitia, Mars	Gratz number method
Model 0 with e of 0.80	1.62×10^4	1.01×10^6		
Model 1 with e of 0.80	1.57×10^4	5.85×10^5	Daedalia Planum, Mars	
Model 1 with e of 0.95	1.73×10^4	6.28×10^5		
Model 2 with e of 0.80	1.53×10^4	5.60×10^5		
Graetz Number of Study Data	5.92×10^2	7.38×10^3		Used the Gratz number method for

Table 16: Summary table of specified impute and Model $M0_{0.80}$ result data.

	Flow 2	Flow 3	Flow 4	Flow 5	Flow 6	Flow 12	Flow 19	Flow 20	Flow 21
Measured Length (km)	63.95	71.72	67.27	214.606	174.542138	83.026322	48.8198	193.087	111.279
Length (km)	891.7993	81.54	442.63	108.49	2049.36	1273.06	1278.52	732.64	483.87
Flow Length Difference	12.95	0.14	5.58	-0.49	10.74	14.33	25.19	2.79	3.35
Eruption Rate (m3/s)	2.32×10^5	1.62×10^4	4.58×10^5	1.09×10^5	5.66×10^5	5.06×10^5	3.50×10^5	1.01×10^6	2.32×10^5
Width (m)	185.22	149.55	878.58	264.59	139.14	213.47	624.01	691.96	342.88
Depth (m)	26.87	13.8	25.83	17.9	44.46	36.1	41.04	35.02	30.72
Crust Temperature (°C)	625	625	625	625	625	625	625	625	625
Phenocryst Content	10.40%	10.40%	10.40%	10.40%	10.40%	10.40%	10.40%	10.40%	10.40%
Emissivity	0.8	0.8	0.8	0.8	0.8	0.8	0.8	0.8	0.8
Ave. Slope	0.875	0.642	0.471	0.485	0.828	0.539	0.37	0.346	0.328

Table 17: Summary table of specified impute and Model $M1_{0.80}$ result data.

	Flow 2	Flow 3	Flow 4	Flow 5	Flow 6	Flow 12	Flow 19	Flow 20	Flow 21
Measured Length (km)	63.95	71.72	67.27	214.61	174.54	83.03	48.82	193.09	111.28
Length (km)	63.8	72.54	61.01	194.56	172.36	78.8	45.13	191.64	109.87
Flow Length Difference	-0.23%	1.14%	-9.31%	-9.34%	-1.25%	-5.09%	-7.56%	-0.75%	-1.27%
Eruption Rate (m3/s)	5.19×10^4	1.57×10^4	1.71×10^5	1.78×10^5	9.98×10^4	1.96×10^5	4.35×10^4	5.84×10^5	1.49×10^5
Beginning Viscosity	1492.38	949.61	884.82	245.92	1873.26	942.84	1246.87	649.24	580.47
Ending Viscosity	1.14×10^6	2.17×10^5	1.04×10^5	2.23×10^3	3.14×10^{10}	4.27×10^4	2.74×10^6	1.20×10^5	7.79×10^6
Width (m)	185.22	149.55	878.58	264.59	139.14	213.47	624.01	691.96	342.88
Depth (m)	26.87	13.8	25.83	17.9	44.46	36.1	41.04	35.02	30.72
Crust Temperature (°C)	625	625	625	625	625	625	625	625	625
Phenocryst Content	30.77%	10.90%	24.00%	0.00%	33.30%	24.90%	28.60%	19.27%	17.41%
Emissivity	0.8	0.8	0.8	0.8	0.8	0.8	0.8	0.8	0.8
Ave. Slope	0.88	0.64	0.47	0.485	0.83	0.54	0.37	0.35	0.33

Table 18: Summary table of specified impute and Model $M1_{0.95}$ result data.

	Flow 2	Flow 3	Flow 4	Flow 5	Flow 6	Flow 12	Flow 19	Flow 20	Flow 21
Measured Length (km)	63.95	71.72	67.27	214.61	174.54	83.03	48.82	193.09	111.28
Length (km)	63.80	72.54	66.63	210.47	171.21	89.06	46.52	198.64	111.87
Flow Length Difference	-0.24%	1.14%	-0.96%	-1.93%	-1.91%	7.27%	-4.71%	2.88%	0.53%
Eruption Rate (m^3/s)	5.54×10^4	1.73×10^4	1.99×10^5	1.78×10^5	1.07×10^5	2.01×10^5	4.67×10^4	6.28×10^5	1.53×10^5
Beginning Viscosity	1413.41	373.16	793.39	245.92	1771.59	920.31	1214.58	610.2	566.7
Ending Viscosity	2.98×10^5	2.26×10^7	5.88×10^4	8.53×10^3	1.13×10^4	3.12×10^5	8.30×10^5	3.60×10^4	1.67×10^4
Width (m)	185.22	149.55	878.58	264.59	139.14	213.47	624.01	691.96	342.88
Depth (m)	26.87	13.8	25.83	17.9	44.46	36.1	41.04	35.02	30.72
Crust Temperature (°C)	625	625	625	575	625	625	625	625	625
Phenocryst Content	30.13%	9.20%	22.40%	0.00%	32.70%	24.56%	28.27%	18.25%	17.00%
Emissivity	0.95	0.95	0.95	0.95	0.95	0.95	0.95	0.95	0.95
Ave. Slope	0.88	0.64	0.47	0.49	0.83	0.54	0.37	0.35	0.33

Table 19: Summary table of specified impute and Model $M2_{0.80}$ result data.

	Flow 2	Flow 3	Flow 4	Flow 5	Flow 6	Flow 12	Flow 19	Flow 20	Flow 21
Measured Length (km)	63.95	71.72	67.27	214.61	174.54	83.03	48.82	193.09	111.28
Length (km)	63.8	73.54	67.63	214.81	176.36	87.06	45.4378	186.64	111.87
Flow Length Difference	-0.23%	2.54%	0.54%	0.10%	1.04%	4.86%	-6.93%	-3.34%	0.53%
Eruption Rate (m^3/s)	4.97×10^4	1.53×10^4	1.78×10^5	1.38×10^5	9.59×10^4	1.85×10^5	4.16×10^4	5.60×10^5	1.35×10^5
Beginning Viscosity	1562.5	419.51	875.36	317.51	1955.95	998.1	1319.68	679.2	634.5
Ending Viscosity	1.32×10^5	1.63×10^4	2.98×10^4	1.12×10^4	1.82×10^7	1.92×10^6	9.82×10^8	1.73×10^6	5.26×10^4
Width (m)	185.22	149.55	878.58	264.59	139.14	213.47	624.01	691.96	342.88
Depth (m)	26.87	13.8	25.83	17.9	44.46	36.1	41.04	35.02	30.72
Crust Temperature (°C)	625	625	625	500	625	625	625	625	625
Phenocryst Content	30.55%	10.25%	22.90%	4.40%	33.07%	24.79%	28.50%	18.95%	17.82%
Emissivity	0.8	0.8	0.8	0.8	0.8	0.8	0.8	0.8	0.8
Ave. Slope	0.875	0.642	0.471	0.485	0.828	0.539	0.37	0.346	0.328

Table 20: Reference table of specifications for the instruments used in this study.

	CTX	MOLA	THEMIS
Type of Instrument	Visible, Single Band Imager	Laser Altimeter	Multi-band imager
Resolution	~5-6 m	DEM Horizontal: 100 m Vertical: ~3 m PEDR Horizontal: Variable Vertical: 37.5 cm	100 m (Spatial)
Band Pass	0.5-0.7 µm	1.064 µm	11.83 µm

APPENDIX B

FLOW IMAGES

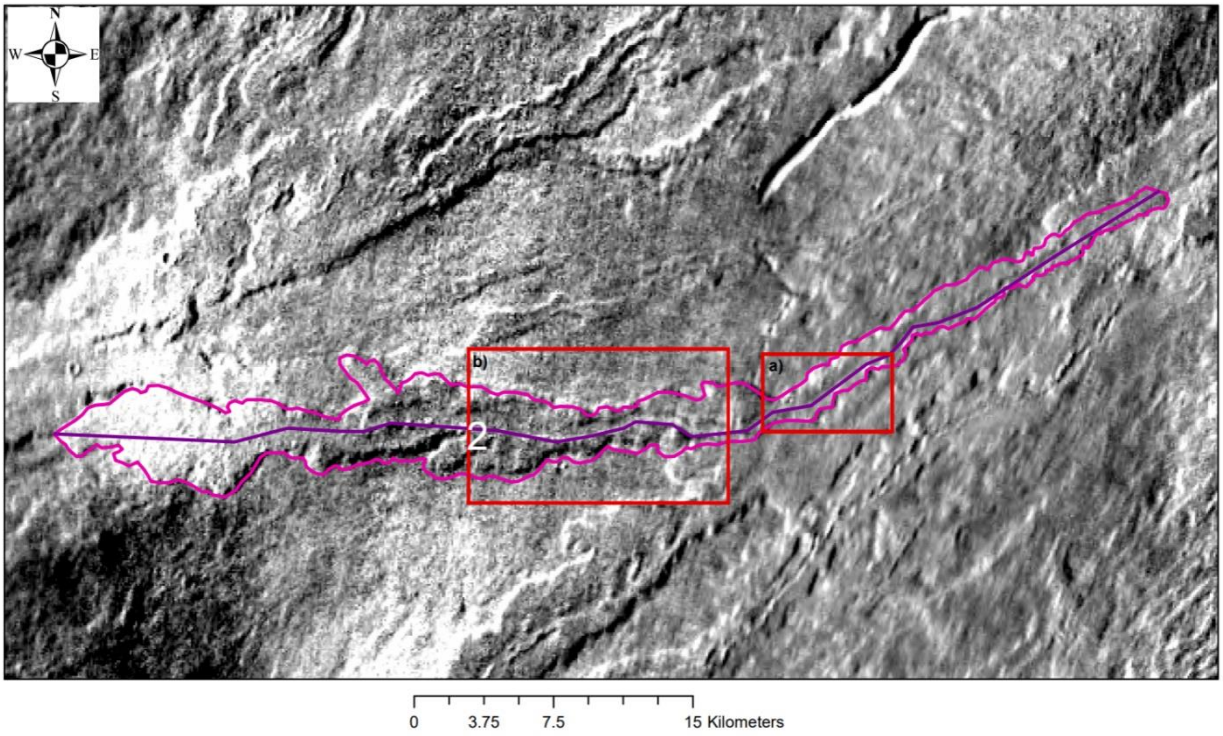

Figure 25: THEMIS mosaic image of Flow 2 with outlines for CTX subsets (Figure 26).

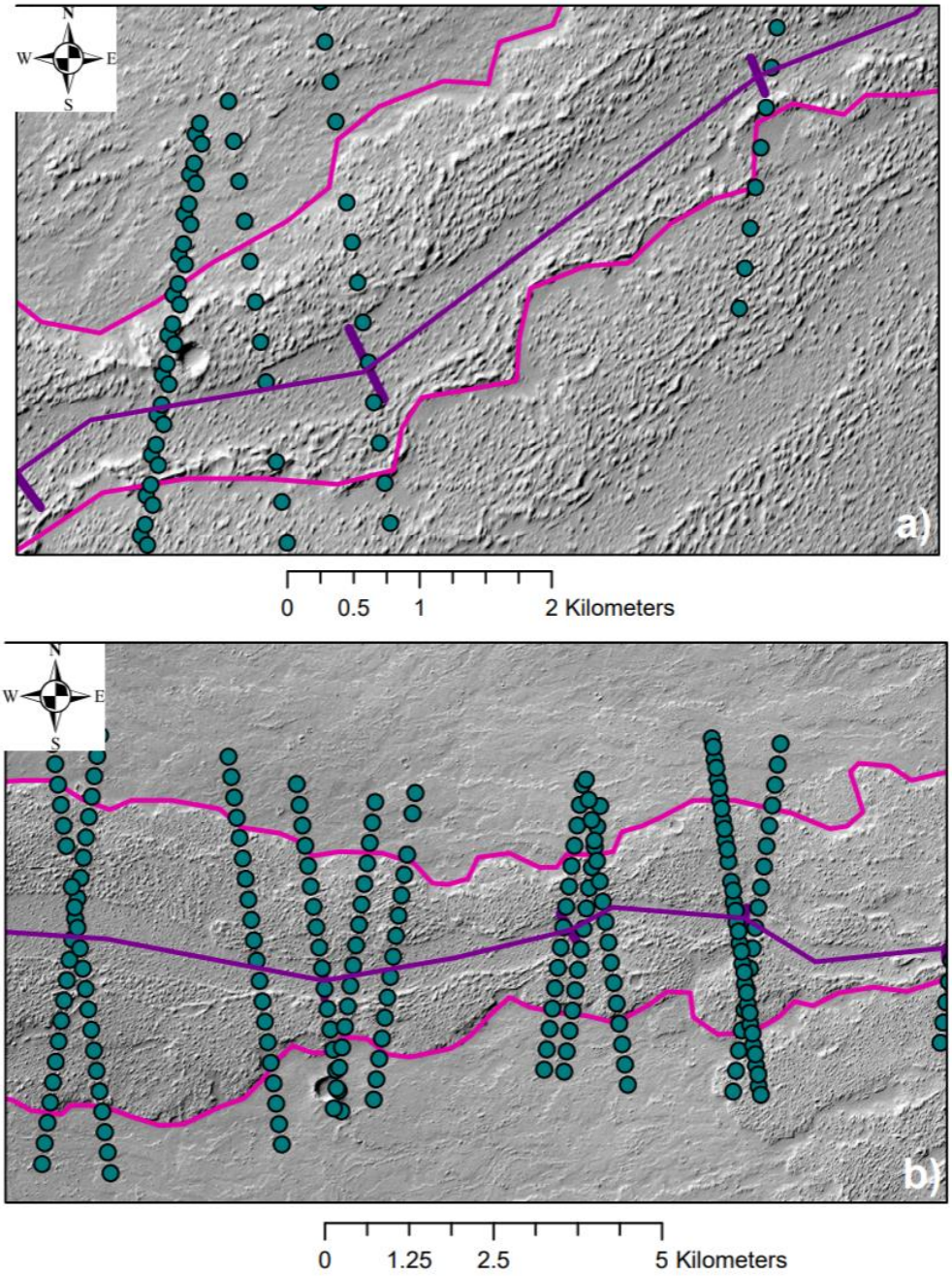

Figure 26: CTX subsets a and b of Flow 2 overplayed with flow length, channel width and MOLA elevation data.

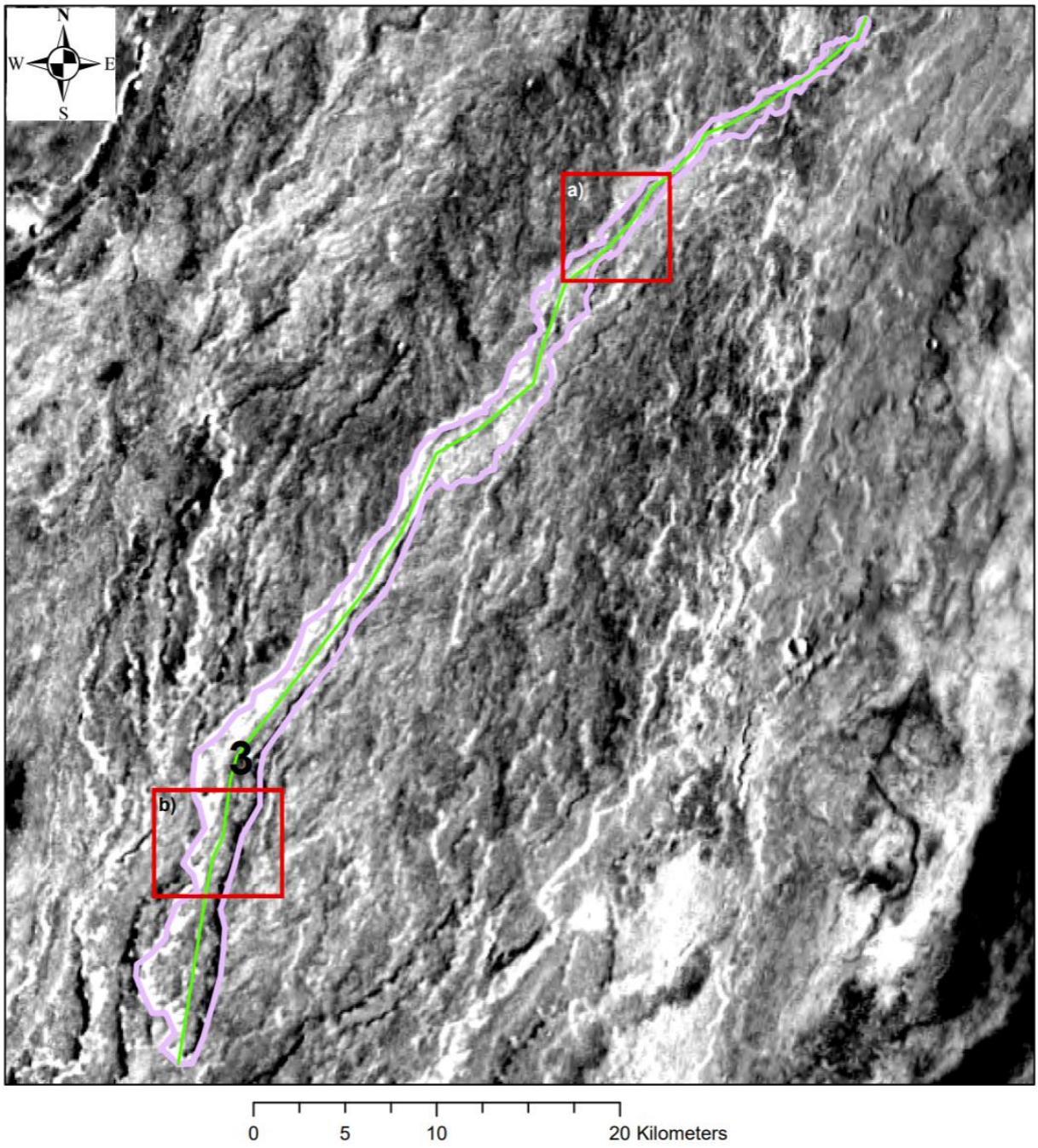

Figure 27: THEMIS mosaic image of Flow 3 with outlines for CTX subsets (Figure 28).

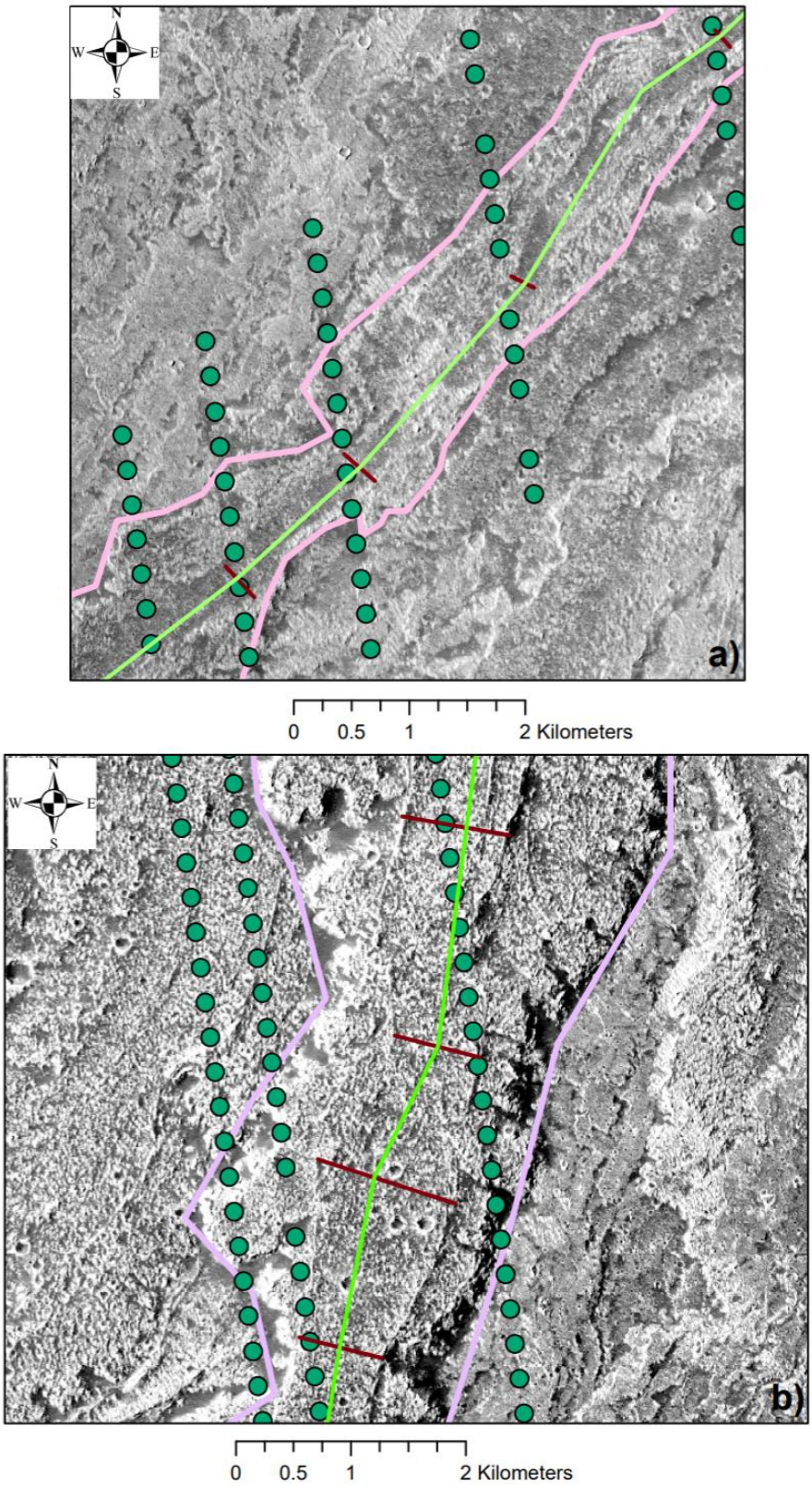

Figure 28: CTX subsets a and b of Flow 3 overplayed with flow length, channel width and MOLA elevation data.

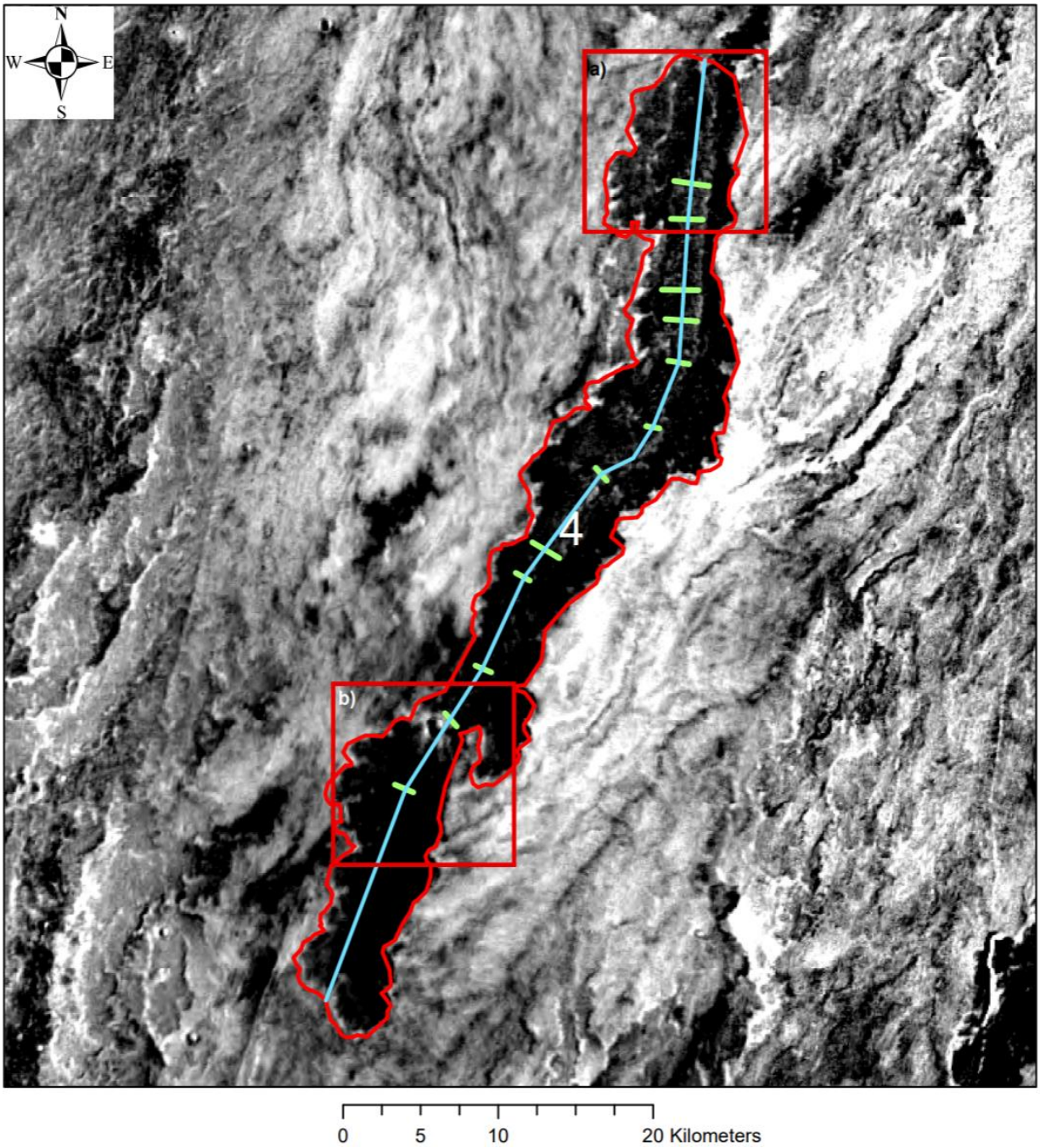

Figure 29: THEMIS mosaic image of Flow 4 with outlines for CTX subsets (Figure 30).

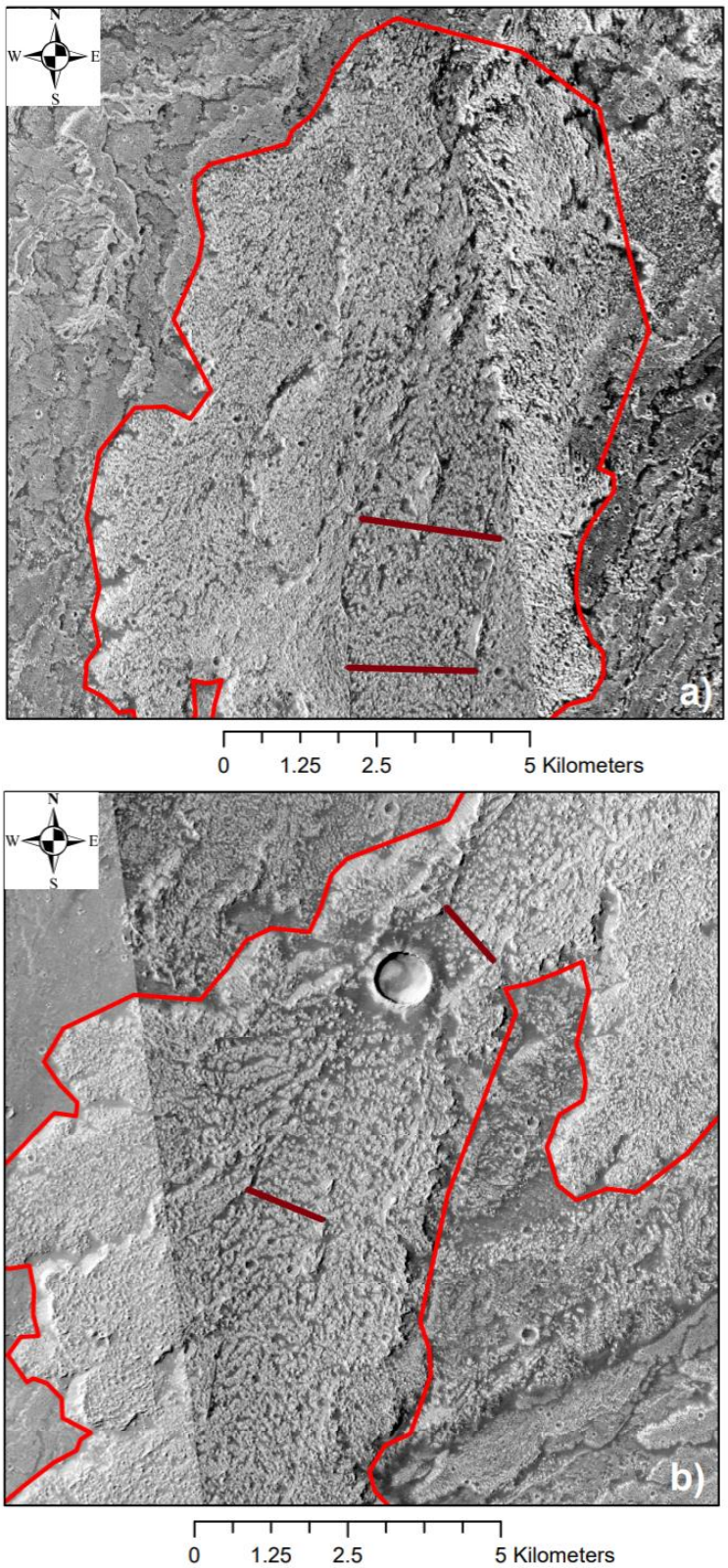

Figure 30: CTX subsets a and b of Flow 4 overplayed with the channel width measurement locations.

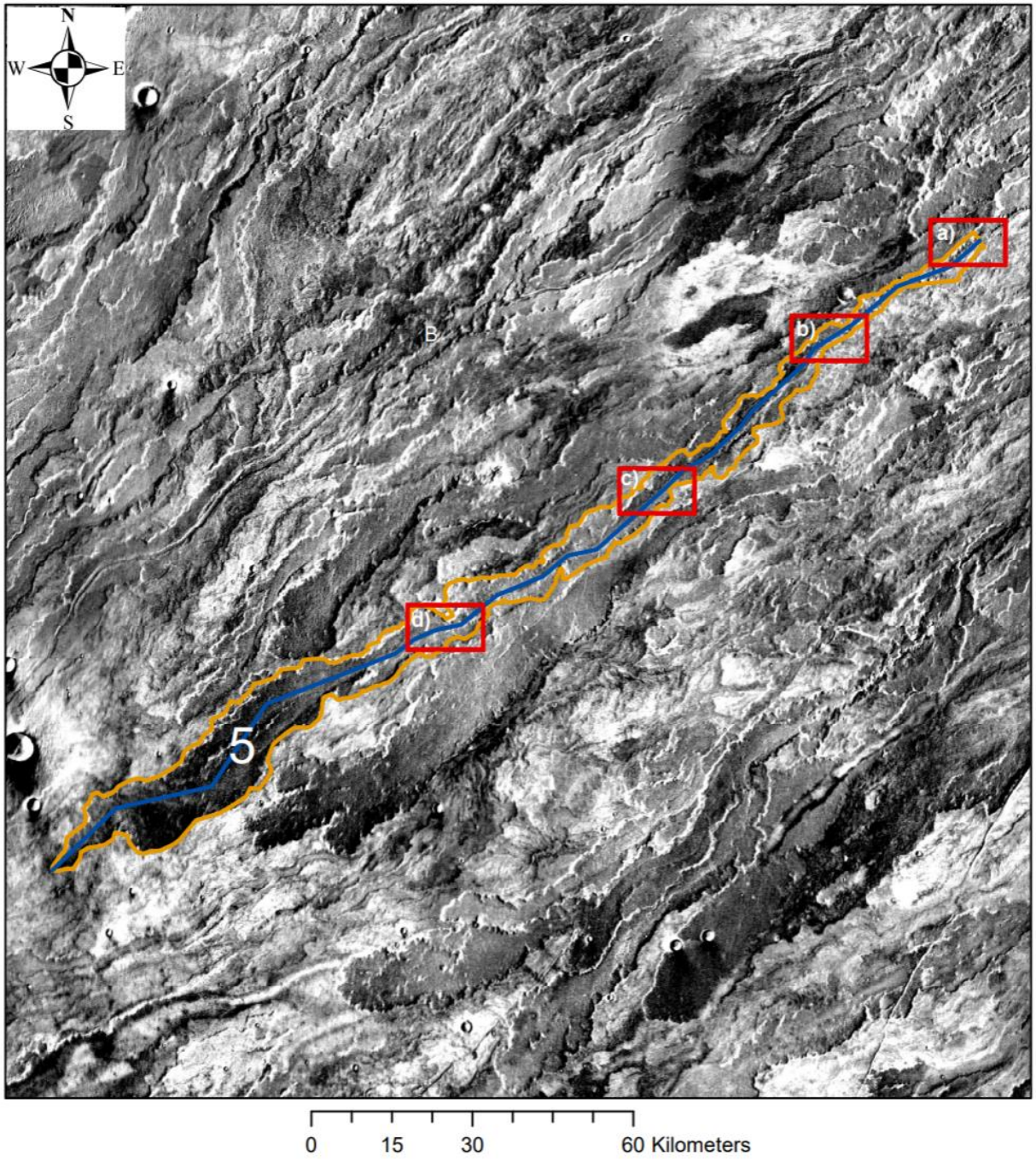

Figure 31: THEMIS mosaic image of Flow 5 with outlines for CTX subsets (Figure 32).

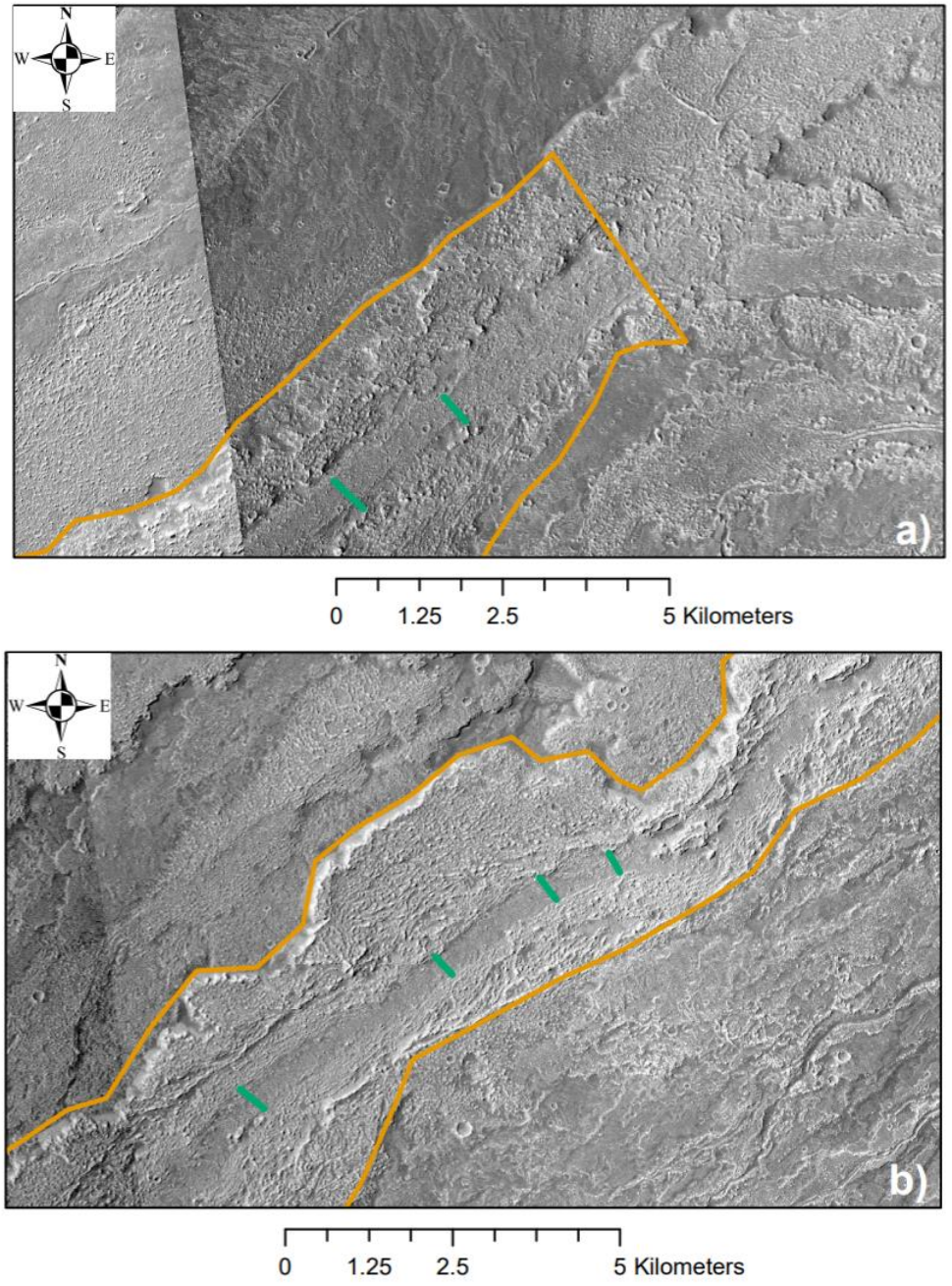
N
W
E
S
a)
0
1.25
2.5
5 Kilometers
N
W
E
S
b)
0
1.25
2.5
5 Kilometers

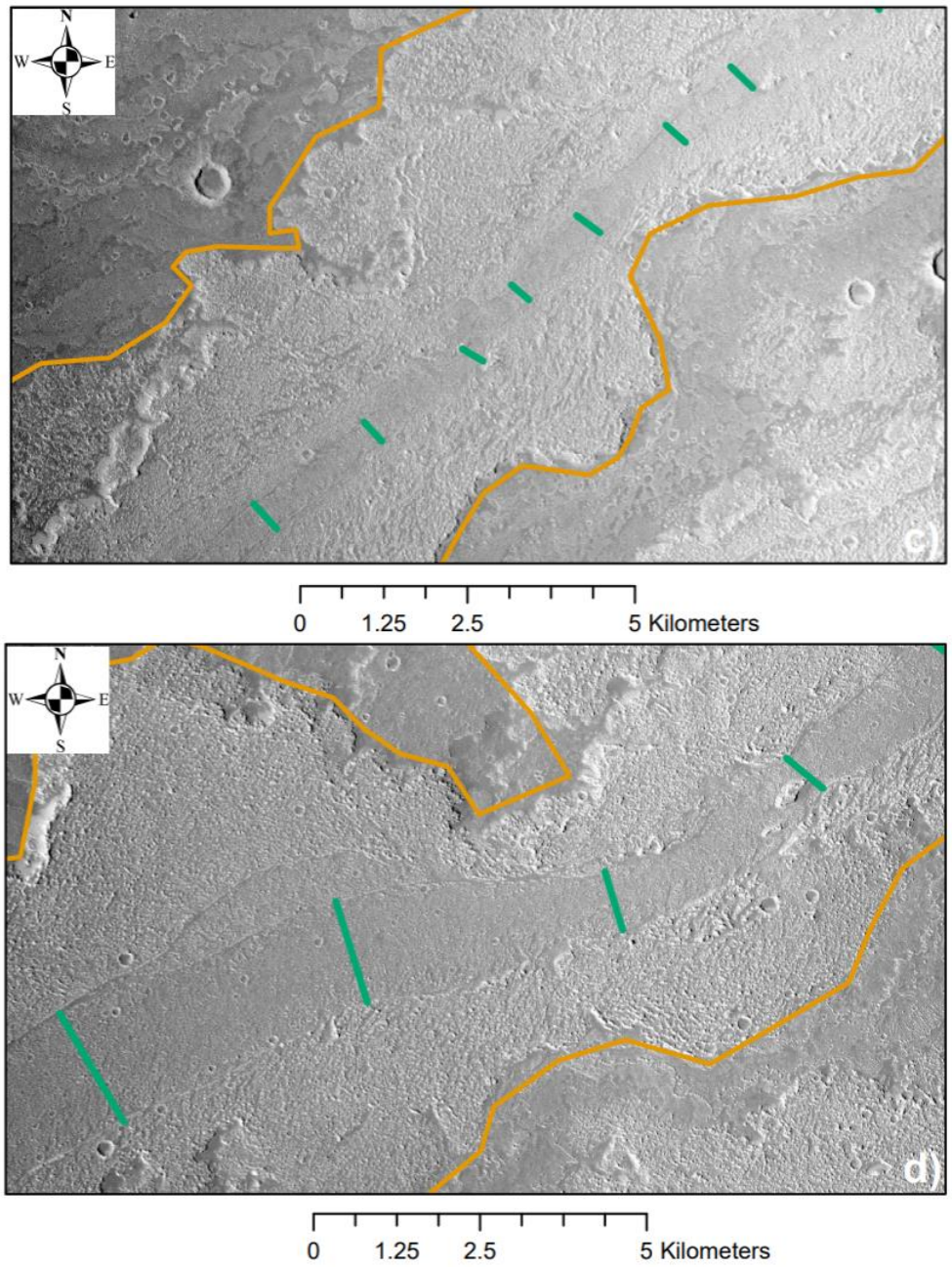

Figure 32: CTX subsets a-d of Flow 5 overplayed with flow channel width measurement locations.

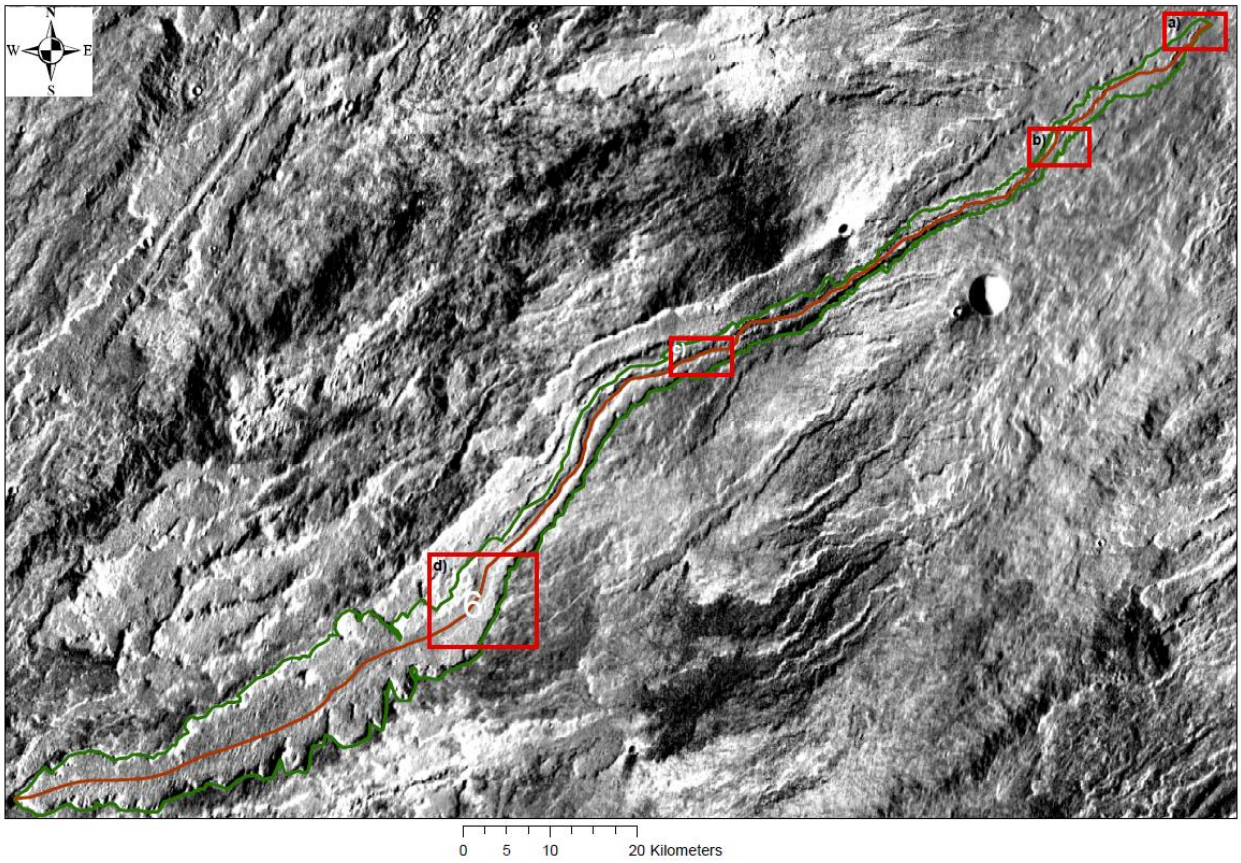

Figure 33: THEMIS mosaic image of Flow 6 with outlines for CTX subsets (Figure 34).

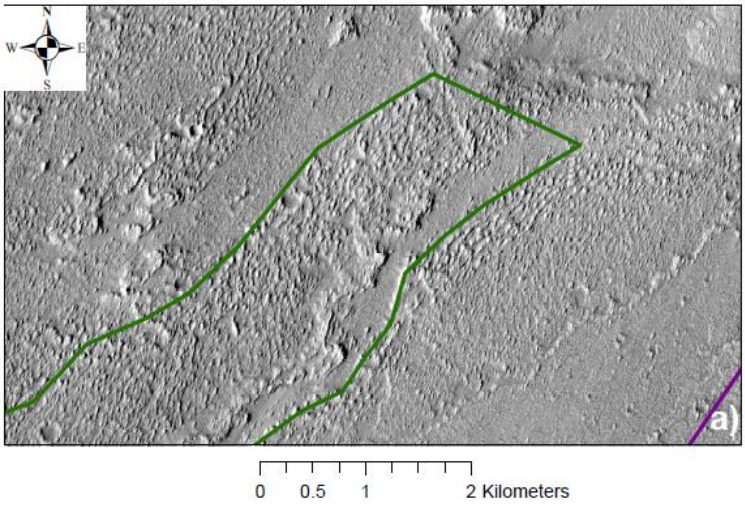

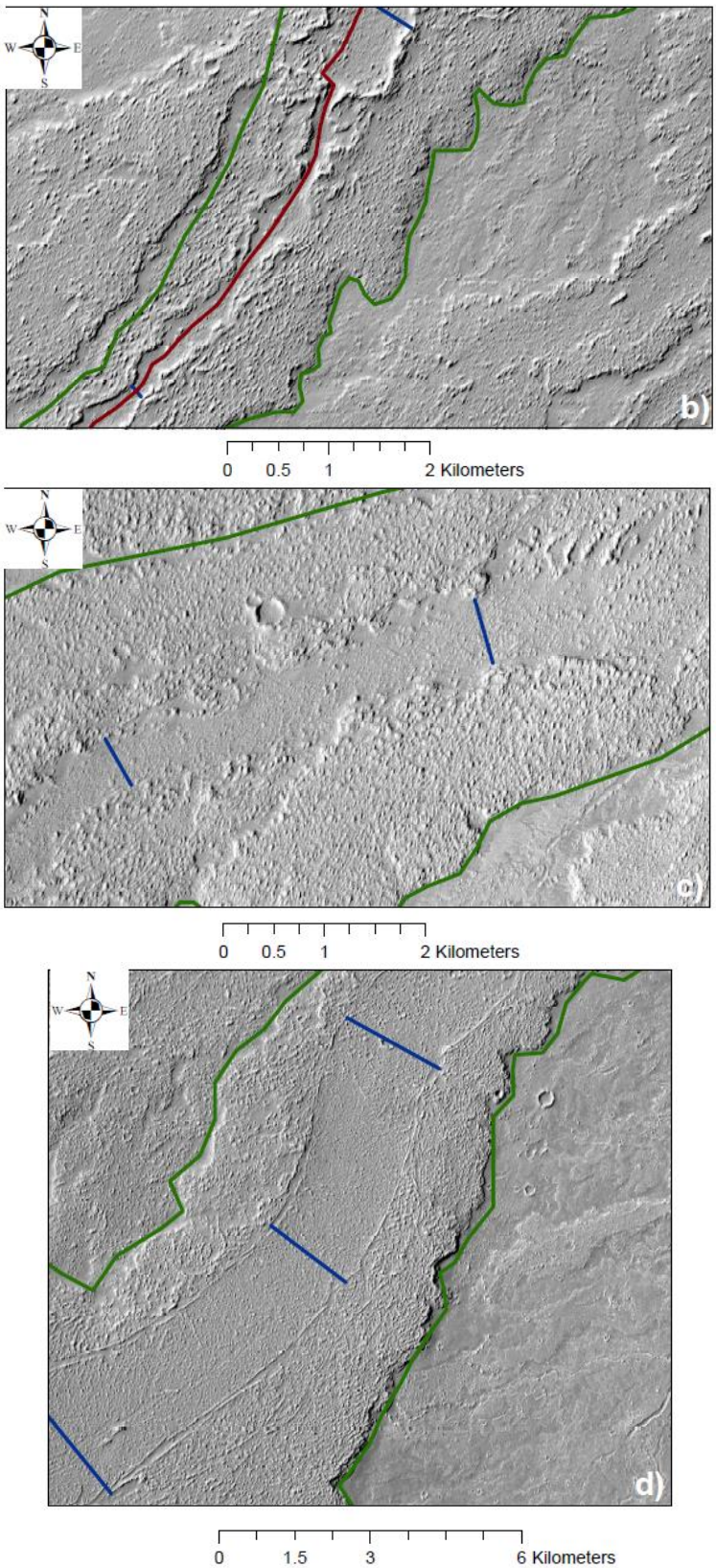

Figure 34: CTX subsets a-d of Flow 6 overplayed with flow channel width measurement locations.

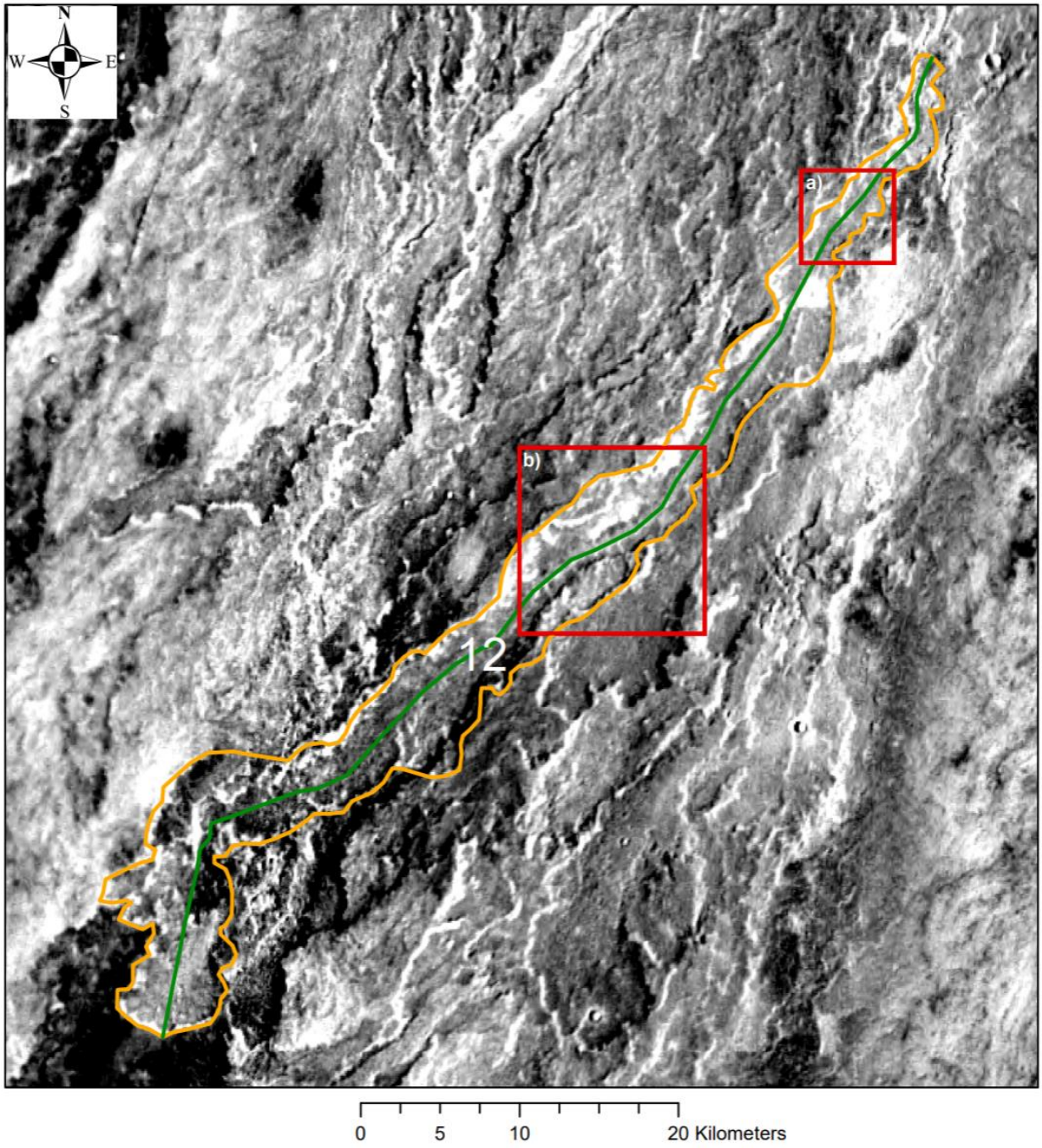

Figure 35: THEMIS mosaic image of Flow 12 with outlines for CTX subsets (Figure 36).

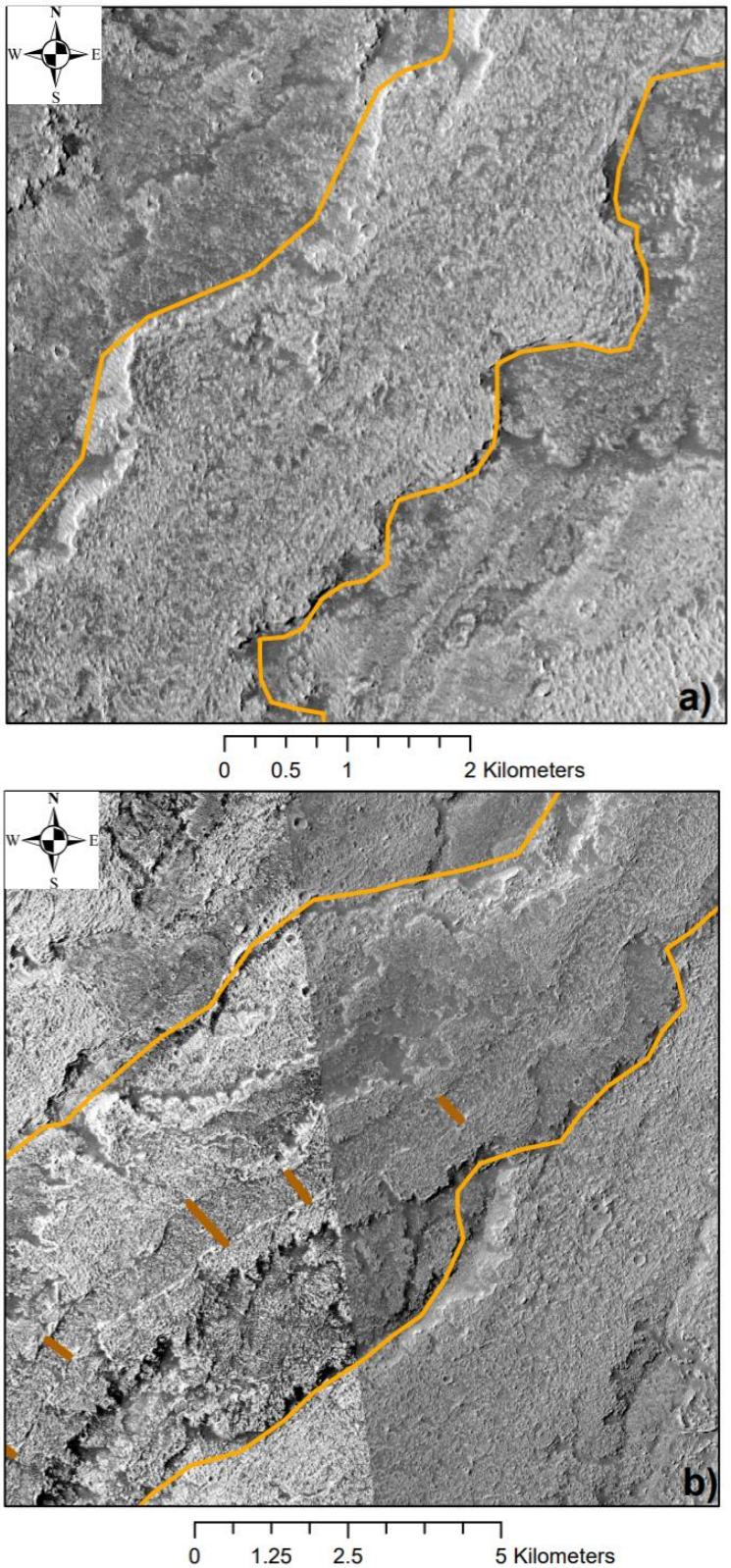

Figure 36: CTX subsets a and b of Flow 12 overplayed with flow channel width measurement locations. Figure 36a does not have lines denoting channel width as the channel is not discernable in this image.

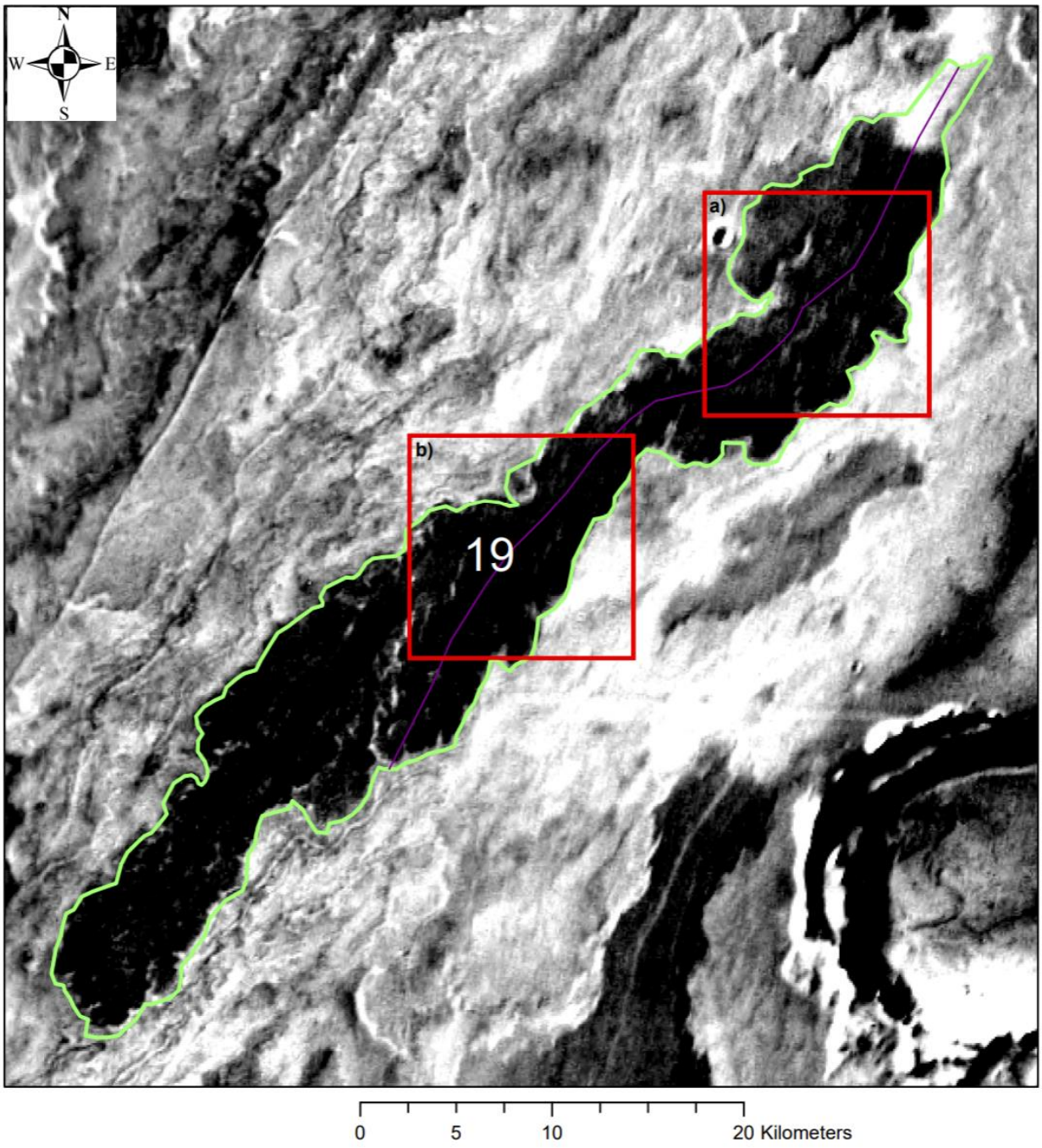

Figure 37: THEMIS mosaic image of Flow 19 with outlines for CTX subsets (Figure 38).

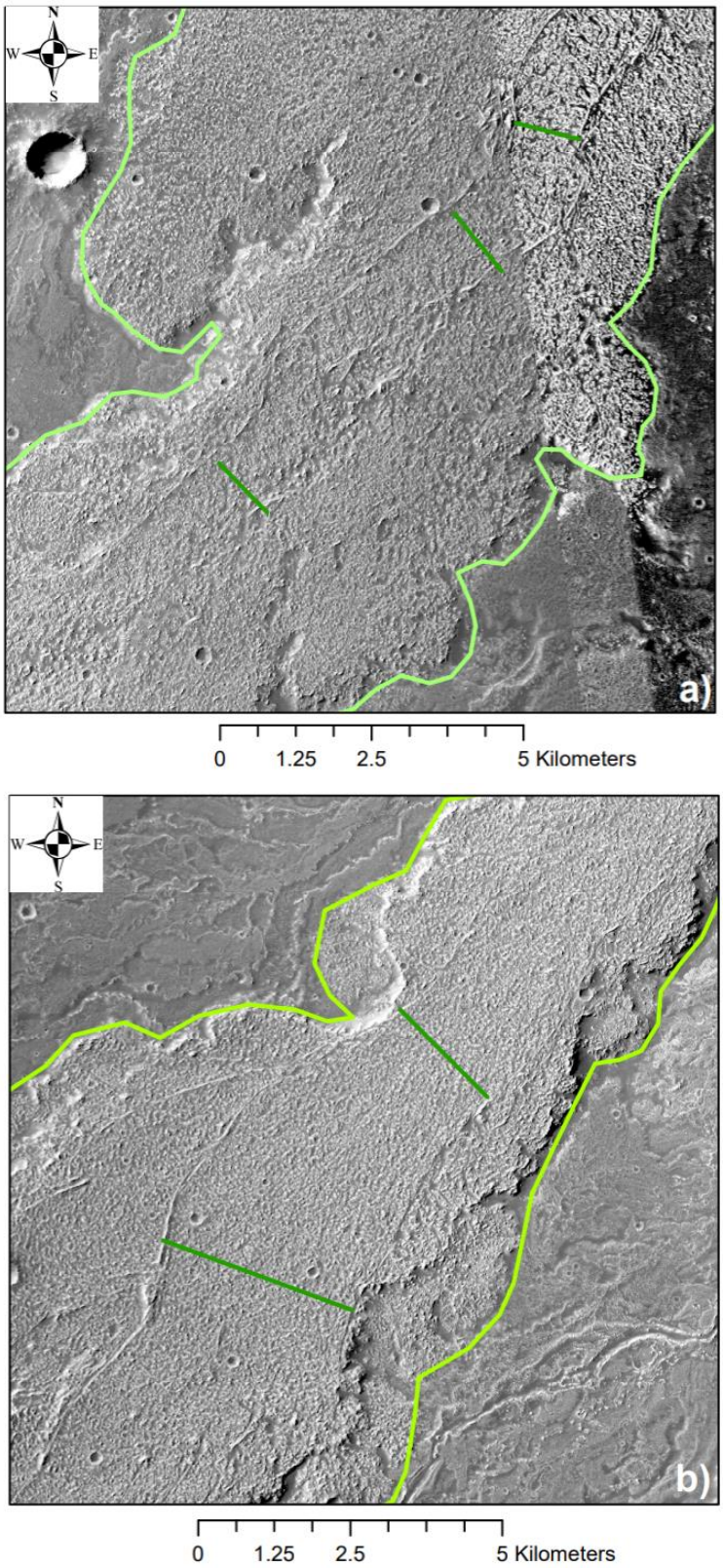

Figure 38: CTX subsets a and b of Flow 19 overplayed with flow channel width measurement locations. Figure 38b is unique as it shows the splitting of the flow channel.

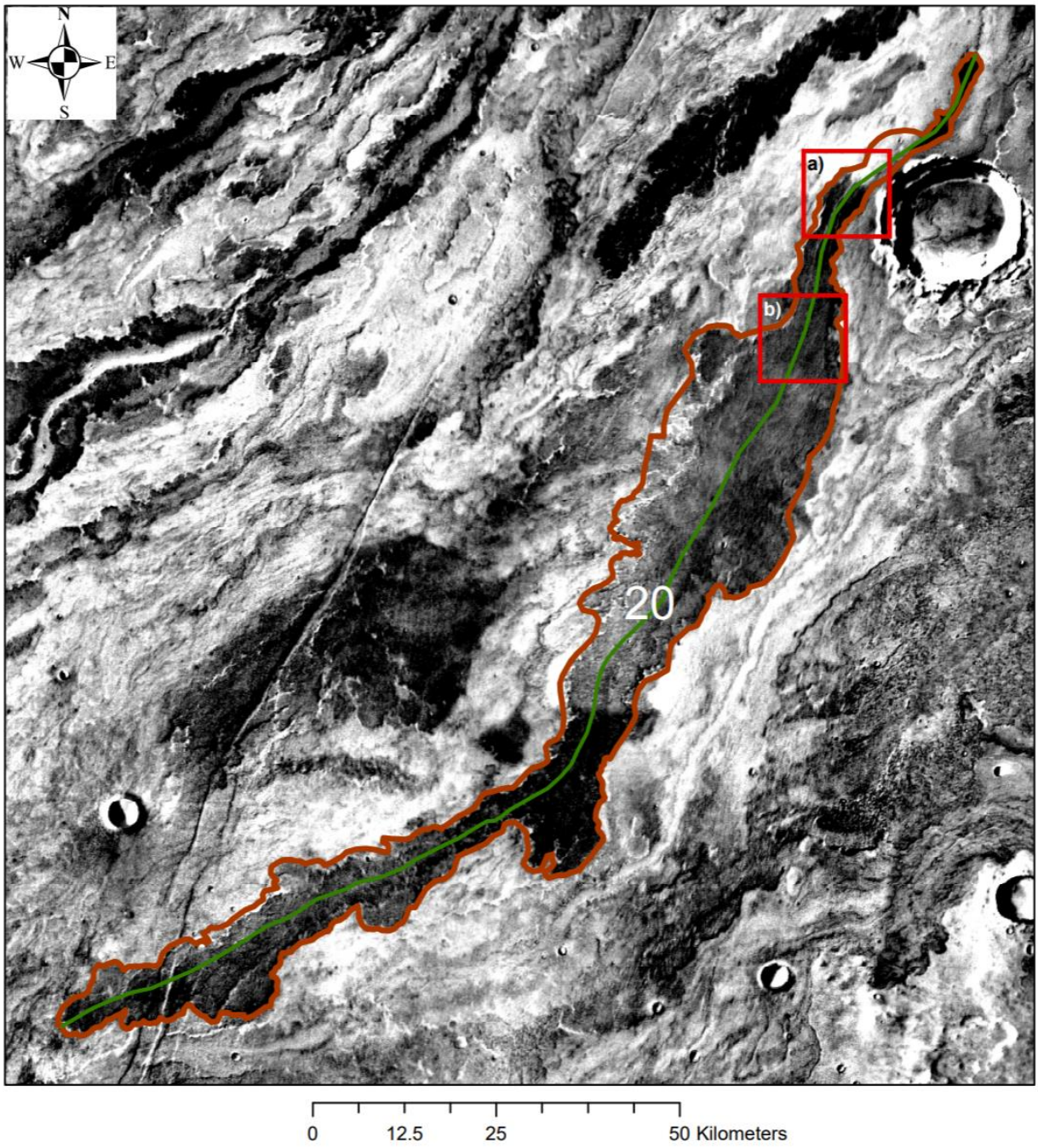

Figure 39: THEMIS mosaic image of Flow 20 with outlines for CTX subsets (Figure 40).

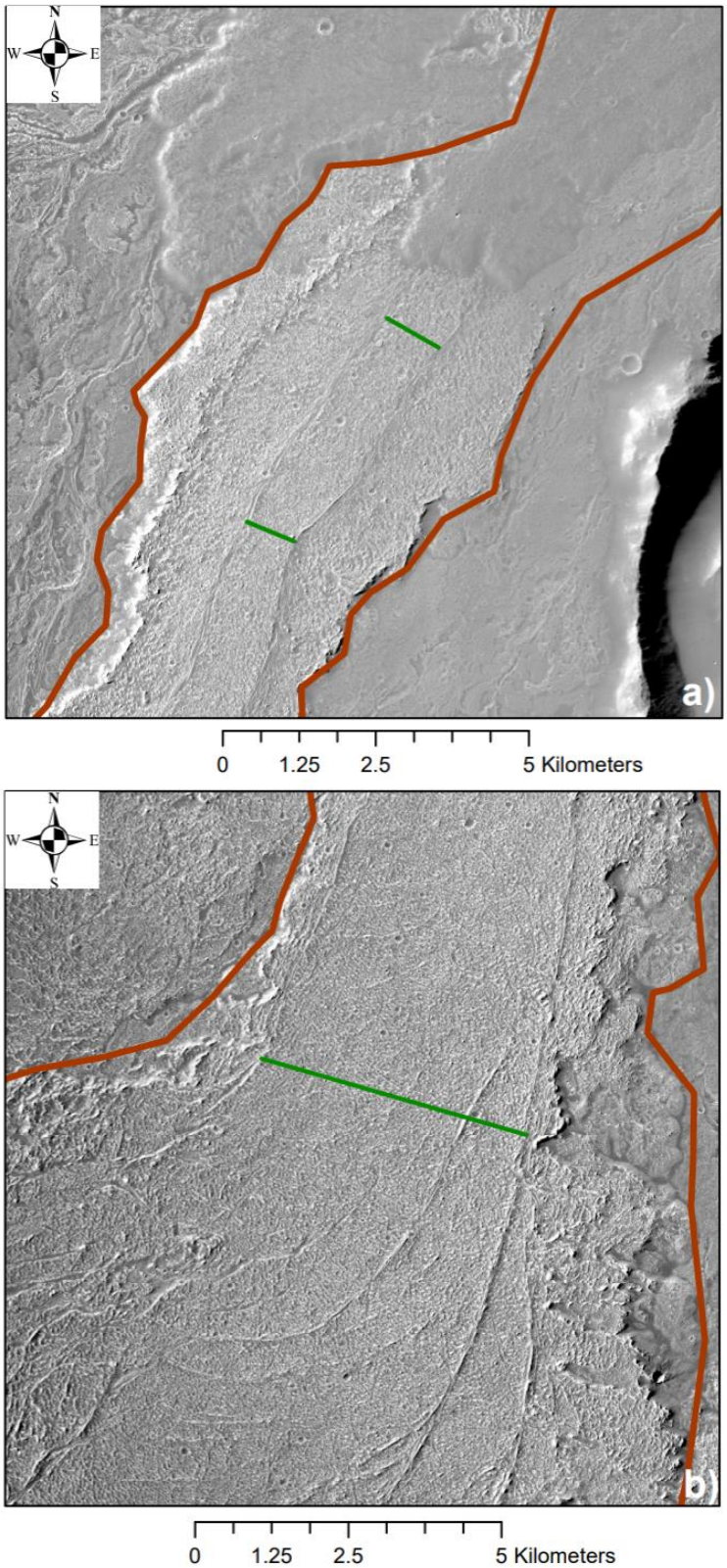

Figure 40: CTX subsets a and b of for Flow 20 with overlays for channel width.

APPENDIX C

LICENSE

This Agreement between Mr. Nathan Beauchamp ("You") and Elsevier ("Elsevier") consists of your license details and the terms and conditions provided by Elsevier and Copyright Clearance Center.

License Number	4241000609860
License date	Dec 02, 2017
Licensed Content Publisher	Elsevier
Licensed Content Publication	Computers & Geosciences
Licensed Content Title	PyFLOWGO: An open-source platform for simulation of channelized lava thermo-rheological properties
Licensed Content Author	Magdalena Oryaëlle Chevrel,Jérémie Labroquère,Andrew J.L. Harris,Scott K. Rowland
Licensed Content Date	Feb 1, 2018
Licensed Content Volume	111
Licensed Content Issue	n/a
Licensed Content Pages	14
Start Page	167
End Page	180
Type of Use	reuse in a thesis/dissertation
Intended publisher of new work	other
Portion	figures/tables/illustrations
Number of figures/tables/illustrations	1
Format	both print and electronic
Are you the author of this Elsevier article?	No
Will you be translating?	No
Original figure numbers	Fig. 1.
Title of your thesis/dissertation	Numerical Modeling of the Daedalia Planum Lava Flows, Mars
Expected completion date	Dec 2017
Estimated size (number of pages)	60

BIBLIOGRAPHY

Bailey, J. E., Harris, A. J. L., Dehn, J., Calvari, S., & Rowland, S. K. (2006). The changing morphology of an open lava channel on Mt. Etna. *Bulletin of Volcanology, 68*(6), 497-515. doi:10.1007/s00445-005-0025-6

Baloga, S. M., & Glaze, L. S. (2008). A self-replication model for long channelized lava flows on the Mars plains. Journal of Geophysical Research, 113(E5), Citation E05003. doi:http://dx.doi.org/10.1029/2007JE002954

Baloga, S. M., Mouginis-Mark, P. J., & Glaze, L. S. (2003). Rheology of a long lava flow at Pavonis Mons, Mars. *Journal of Geophysical Research, 108*(E7), 10. doi:http://dx.doi.org/10.1029/2002JE001981

Bandfield, J. L., Hamilton, V. E., & Christensen, P. R. (2000). A Global View of Martian Surface Compositions from MGS-TES. *Science, 287*(5458), 1626.

Banerdt, W., P. Golombek, M., & L. Tanaka, K. (1992). Stress and tectonics on Mars (Vol. 1).

Bibring, J.-P., Langevin, Y., Gendrin, A. G. B., Poulet, F., Berthe, M., Soufflot, A., . . . Drossart, P. (2005). Mars surface diversity as revealed by the OMEGA/Mars Express observations. *Science, 307*, 1576+.

Bleacher, J. E., Greeley, R., Williams, D. A., Cave, S. R., & Neukum, G. (2007a). Trends in effusive style at the Tharsis Montes, Mars, and implications for the development of the Tharsis province. *Journal of Geophysical Research - Planets, 112*(E9), E09005. doi:10.1029/2006JE002873

Bleacher, J. E., Greeley, R., Williams, D. A., Werner, S. C., Hauber, E., & Neukum, G. (2007b). Olympus Mons, Mars; inferred changes in late Amazonian aged effusive activity from lava flow mapping of Mars Express High Resolution Stereo Camera data. *Journal of Geophysical Research, 112*(E4), Citation E04003. doi:http://dx.doi.org/10.1029/2006JE002826

Calvari, S., Neri, M., & Pinkerton, H. (2003). Effusion rate estimations during the 1999 summit eruption on Mount Etna, and growth of two distinct lava flow fields. *Journal of Volcanology and Geothermal Research, 119*(1), 107-123. doi:http://dx.doi.org/10.1016/S0377-0273(02)00308-6

Carling, G. T., Radebaugh, J., Saito, T., Lorenz, R. D., Dangerfield, A., Tingey, D. G., . . . Diniega, S. (2015). Temperatures, thermal structure, and behavior of eruptions at Kilauea and Erta Ale volcanoes using a consumer digital camcorder. *GeoResJ, 5*, 47-56. doi:http://dx.doi.org/10.1016/j.grj.2015.01.001

Carr, M. H. (2007). *The Surface of Mars*. Cambridge, GB: Cambridge University Press.

Carr, M. H., & Head, J. W. (2010). Geologic history of Mars. *Earth and Planetary Science Letters, 294*(3), 185-203. doi:https://doi.org/10.1016/j.epsl.2009.06.

Cattermole, P. (1987). Sequence, rheological properties, and effusion rates of volcanic flows at Alba Patera, Mars. *Journal of Geophysical Research: Solid Earth, 92*(B4), E553-E560. doi:10.1029/JB092iB04p0E553

Chevrel, M. O., Baratoux, D., Hess, K.-U., & Dingwell, D. B. (2014). Viscous flow behavior of tholeiitic and alkaline Fe-rich martian basalts. *Geochimica et Cosmochimica Acta, 124*(Supplement C), 348-365. doi:https://doi.org/10.1016/j.gca.2013.08.026

Chevrel, M. O., Labroquère, J., Harris, A. J. L., & Rowland, S. K. (2018). PyFLOWGO: An open-source platform for simulation of channelized lava thermo-rheological properties. *Computers & Geosciences, 111*(Supplement C), 167-180. doi:https://doi.org/10.1016/j.cageo.2017.11.009

Christensen, P.R., Engle, E., Anwar, S., Dickenshied, S., Noss, D., Gorelick, N. &Weiss-Malik, M. *JMARS – A Planetary GIS*, http://adsabs.harvard.edu/abs/2009AGUFMIN22A..06C

Cigolini, C., Borgia, A., & Casertano, L. (1984). Intra-crater activity, aa-block lava, viscosity and flow dynamics: Arenal Volcano, Costa Rica. *Journal of Volcanology and Geothermal Research, 20*(1), 155-176. doi:https://doi.org/10.1016/0377-0273(84)90072-6

Coppola, D., Piscopo, D., Staudacher, T., & Cigolini, C. (2009). Lava discharge rate and effusive pattern at Piton de la Fournaise from MODIS data. *Journal of Volcanology and Geothermal Research, 184*(1), 174-192. doi:https://doi.org/10.1016/j.jvolgeores.2008.11.031

Crisp, J., & Baloga, S. (1990). A model for lava flows with two thermal components. *Journal of Geophysical Research: Solid Earth, 95*(B2), 1255-1270. doi:10.1029/JB095iB02p01255

Crisp, J., Kahle, A. B., & Abbott, E. A. (1990). Thermal infrared spectral character of Hawaiian basaltic glasses. *Journal of Geophysical Research: Solid Earth, 95*(B13), 21657-21669. doi:10.1029/JB095iB13p21657

Crown, D., Berman, D., & Ramsey, M. (2015). *Lava Flow Fields of Southern Tharsis, Mars: Flow Types, Interactions, and Ages.* Paper presented at the Lunar and Planetary Science Conference.

Crown, D. A., & Ramsey, M. S. (2016). Morphologic and thermophysical characteristics of lava flows southwest of Arsia Mons, Mars. *Journal of Volcanology and Geothermal Research*. doi:http://dx.doi.org/10.1016/j.jvolgeores.2016.07.008

Edwards, C. S., Nowicki, K. J., Christensen, P. R., Hill, J., Gorelick, N., & Murray, K. (2011). Mosaicking of global planetary image datasets: 1. Techniques and data processing for Thermal Emission Imaging System (THEMIS) multi-spectral data. *Journal of Geophysical Research. Planets, 116*(1). doi:10.1029/2010JE003755

Einstein, A. (1906). Eine neue bestimmung der moleküldimensionen. *Annalen der Physik, 324*(2), 289-306.

Fink, J. H., & Zimbelman, J. (1990). Longitudinal Variations in Rheological Properties of Lavas: Puu Oo Basalt Flows, Kilauea Volcano, Hawaii. In J. H. Fink (Ed.), *Lava Flows and Domes: Emplacement Mechanisms and Hazard Implications* (pp. 157-173). Berlin, Heidelberg: Springer Berlin Heidelberg.

Flynn, L. P., Harris, A. J. L., & Wright, R. (2001). Improved identification of volcanic features using Landsat 7 ETM+. *Remote Sensing of Environment, 78*(1-2), 180-193.

Flynn, L. P., & Mouginis-Mark, P. J. (1992). Cooling rate of an active Hawaiian lava flow from nighttime spectroradiometer measurements. *Geophysical Research Letters, 19*(17), 1783-1786. doi:10.1029/92GL01577

Flynn, L. P., & Mouginis-Mark, P. J. (1994). Temperature of an active lava channel from spectral measurements, Kilauea Volcano, Hawaii. *Bulletin of Volcanology, 56*(4), 297-301. doi:10.1007/bf00302082

Garry, W. B., Zimbelman, J. R., & Gregg, T. K. P. (2007). Morphology and emplacement of a long channeled lava flow near Ascraeus Mons Volcano, Mars. *Journal of Geophysical Research: Planets, 112*(E8), n/a-n/a. doi:10.1029/2006JE002803

Garvin, J. B., Sakimoto, S. E. H., Frawley, J. J., & Schnetzler, C. (2000). North Polar Region Craterforms on Mars: Geometric Characteristics from the Mars Orbiter Laser Altimeter. *Icarus, 144*(2), 329-352. doi:http://dx.doi.org/10.1006/icar.1999.6298

Gauthier, F. (1973). Field and Laboratory Studies of the Rheology of Mount Etna Lava. Philosophical Transactions of the Royal Society of London. Series A, Mathematical and Physical Sciences, 274(1238), 83-98. doi:10.1098/rsta.1973.0028

Giacomini, L., Massironi, M., Martellato, E., Pasquarè, G., Frigeri, A., & Cremonese, G. (2009). Inflated flows on Daedalia Planum (Mars)? Clues from a comparative analysis with the Payen volcanic complex (Argentina). *Planetary and Space Science, 57*(5), 556-570. doi:10.1016/j.pss.2008.12.001

Giordano, D., Russell, J. K., & Dingwell, D. B. (2008). Viscosity of magmatic liquids: A model. *Earth and Planetary Science Letters, 271*(1), 123-134. doi:https://doi.org/10.1016/j.epsl.2008.03.038

Glaze, L. S. (1998). Dimensions of Pu'u O'o lave flows on Mars. *Journal of Geophysical Research, 103*(E6), 13659-13666. doi:10.1029/97JE01427

Glaze, L. S., & Baloga, S. M. (2007). Topographic variability on Mars: Implications for lava flow modeling. *Journal of Geophysical Research - Planets, 112*(E8), E08006. doi:10.1029/2006JE002879

Glaze, L. S., Baloga, S. M., & Stofan, E. R. (2003). A methodology for constraining lava flow rheologies with MOLA. *Icarus, 165*(1), 26-33. doi:http://dx.doi.org/10.1016/S0019-1035(03)00171-4

Greeley, R., Bridges, N. T., Crown, D. A., Crumpler, L., Fagents, S. A., Mouginis-Mark, P. J., & Zimbelman, J. R. (2000). Volcanism on the Red Planet: Mars. In J. R. Zimbelman & T. K. P. Gregg (Eds.), *Environmental Effects on Volcanic Eruptions: From Deep Oceans to Deep Space* (pp. 75-112). Boston, MA: Springer US.

Gregg, T. K. P., & Fink, J. H. (1996). Quantification of extraterrestrial lava flow effusion rates through laboratory simulations. *Journal of Geophysical Research: Planets, 101*(E7), 16891-16900. doi:10.1029/96JE01254

Harris, A. J. L. (2013a). *Thermal remote sensing of active volcanoes: a user's manual*: Cambridge University Press, 78-90.

Harris, A. J. L. (2013b). Lava flows. In: Fagents, S., Gregg, T. & Lopes, R. (eds.) *Modeling Volcanic Processes. The Physics and Mathematics of Volcanism.* Cambridge University Press, Cambridge, 85–106.

Harris, A., Bailey, J., Calvari, S., & Dehn, J. (2005). Heat loss measured at a lava channel and its implications for down-channel cooling and rheology. In M. Manga & G. Ventura (Eds.): Geological Society of America.

Harris, A., Favalli, M., Mazzarini, F., & Pareschi, M. T. (2007). Best-fit results from application of a thermo-rheological model for channelized lava flow to high spatial resolution morphological data. *Geophysical Research Letters, 34*(1), L01301. doi:10.1029/2006GL028126

Harris, A. J., & Rowland, S. (2001). FLOWGO: a kinematic thermo-rheological model for lava flowing in a channel. *Bulletin of Volcanology, 63*(1), 20-44.

Harris, A. J. L., Favalli, M., Mazzarini, F., & Hamilton, C. W. (2009). Construction dynamics of a lava channel. *Bulletin of Volcanology, 71*(4), 459-474. doi:10.1007/s00445-008-0238-6

Harris, A. J. L., Flynn, L. P., Keszthelyi, L., Mouginis-Mark, P. J., Rowland, S. K., & Resing, J. A. (1998). Calculation of lava effusion rates from Landsat TM data. *Bulletin of Volcanology, 60*(1), 52-71. doi:10.1007/s004450050216

Harris, A. J. L., Murray, J. B., Aries, S. E., Davies, M. A., Flynn, L. P., Wooster, M. J., . . . Rothery, D. A. (2000). Effusion rate trends at Etna and Krafla and their implications for eruptive mechanisms. *Journal of Volcanology and Geothermal Research, 102*(3–4), 237-269. doi:https://doi.org/10.1016/S0377-0273(00)00190-6

Harris, A. J. L., Rhety, M., Gurioli, L., Villeneuve, N., & Paris, R. (2015). Simulating the thermorheological evolution of channel-contained lava; FLOWGO and its implementation in EXCEL. *Special Publication - Geological Society of London, 426*, 24. doi:http://dx.doi.org/10.1144/SP426.9

Harris, A. J. L., & Rowland, S. K. (2015a). FLOWGO 2012 *Hawaiian Volcanoes* (pp. 457-481): John Wiley & Sons, Inc.

Harris, A. J., & Rowland, S. (2015b). Lava flows and rheology. Sigurdsson, H., Houghton, B., McNutt, S., Rymer, H., & Stix, J. (eds.) *The encyclopedia of volcanoes.* Elsevier Science, 317-455.

Hartmann, W. K., & Neukum, G. (2001). Cratering Chronology and the Evolution of Mars. *Space Science Reviews, 96*(1), 165-194. doi:10.1023/a:1011945222010

Hauber, E., Bleacher, J., Gwinner, K., Williams, D., & Greeley, R. (2009). The topography and morphology of low shields and associated landforms of plains volcanism in the Tharsis region of Mars. *Journal of Volcanology and Geothermal Research, 185*(1), 69-95. doi:http://dx.doi.org/10.1016/j.jvolgeores.2009.04.015

Hauber, E., Brož, P., Jagert, F., Jodłowski, P., & Platz, T. (2011). Very recent and wide-spread basaltic volcanism on Mars. *Geophysical Research Letters, 38*(10), n/a-n/a. doi:10.1029/2011GL047310

Hess, K. U., & Dingwell, D. D. (1996). Viscosities of hydrous leucogranitic melts: A non-Arrhenian model. American Mineralogist, 81(9), 1297-1300. doi:10.2138/am-1996-9-1031

Hiesinger, H., Head, J. W., III, & Neukum, G. (2007). Young lava flows on the eastern flank of Ascraeus Mons; rheological properties derived from High Resolution Stereo Camera (HRSC) images and Mars Orbiter Laser Altimeter (MOLA) data. *Journal of Geophysical Research, 112*(E5), Citation E05011. doi:http://dx.doi.org/10.1029/2006JE002717

Hill, J., Edwards, C., & Christensen, P. (2014). *Mapping the Martian Surface with THEMIS Global Infrared Mosaics.* Paper presented at the Eighth International Conference on Mars.

Hon, K. E. N., Kauahikaua, J. I. M., Denlinger, R., & Mackay, K. (1994). Emplacement and inflation of pahoehoe sheet flows: Observations and measurements of active lava flows on Kilauea Volcano, Hawaii. *GSA Bulletin, 106*(3), 351-370. doi:10.1130/0016-7606(1994)106<0351:EAIOPS>2.3.CO;2

Hulme, G. (1974). The Interpretation of Lava Flow Morphology. *Geophysical Journal International, 39*(2), 361-383. doi:10.1111/j.1365-246X.1974.tb05460.x

Hulme, G. (1976). The determination of the rheological properties and effusion rate of an Olympus Mons lava. *Icarus, 27*(2), 207-213. doi:10.1016/0019-1035(76)90004-X

Jeffreys, H. (1925). LXXXIV. The flow of water in an inclined channel of rectangular section. *Philosophical Magazine, 49*(293), 793-807. doi:10.1080/14786442508634662

Keszthelyi, L., McEwen, A., & Thordarson, T. (2000). Terrestrial analogs and thermal models for Martian flood lavas. *Journal of Geophysical Research: Planets, 105*(E6), 15027-15049.

Keszthelyi, L., & Self, S. (1998). Some physical requirements for the emplacement of long basaltic lava flows. *Journal of Geophysical Research: Solid Earth, 103*(B11), 27447-27464.

Kilburn, C. R. J., & Lopes, R. M. C. (1991). General patterns of flow field growth: Aa and blocky lavas. Journal of Geophysical Research: Solid Earth, 96(B12), 19721-19732. doi:10.1029/91JB01924

Lopes, R. M. C., & Kilburn, C. R. J. (1990). Emplacement of lava flow fields: Application of terrestrial studies to Alba Patera, Mars. *Journal of Geophysical Research: Solid Earth, 95*(B9), 14383-14397. doi:10.1029/JB095iB09p14383

Malin, M. C. (1980). Lengths of Hawaiian lava flows. *Geology, 8*(7), 306-308. doi:10.1130/0091-7613(1980)8<306:LOHLF>2.0.CO;2

Malin, M. C., Bell, J. F., Cantor, B. A., Caplinger, M. A., Calvin, W. M., Clancy, R. T., . . . Wolff, M. J. (2007). Context Camera Investigation on board the Mars Reconnaissance Orbiter. *Journal of Geophysical Research: Planets, 112*(E5), n/a-n/a. doi:10.1029/2006JE002808

Mano, J. F., & Pereira, E. (2004). Data Analysis with the Vogel−Fulcher−Tammann−Hesse Equation. The Journal of Physical Chemistry A, 108(49), 10824-10833. doi:10.1021/jp0484433

Ming, D. W., Gellert, R., Morris, R. V., Arvidson, R. E., Brückner, J., Clark, B. C., . . . Zipfel, J. (2008). Geochemical properties of rocks and soils in Gusev Crater, Mars: Results of the Alpha Particle X-Ray Spectrometer from Cumberland Ridge to Home Plate. Journal of Geophysical Research: Planets, 113(E12), n/a-n/a. doi:10.1029/2008JE003195

Moore, H., Arthur, D., & Schaber, G. (1978). *Yield strengths of flows on the Earth, Mars, and Moon.* Paper presented at the Lunar and planetary science conference proceedings.

Neukum, G., Ivanov, B. A., & Hartmann, W. K. (2001). Cratering Records in the Inner Solar System in Relation to the Lunar Reference System. In R. Kallenbach, J. Geiss, & W. K. Hartmann (Eds.), *Chronology and Evolution of Mars: Proceedings of an ISSI Workshop, 10–14 April 2000, Bern, Switzerland* (pp. 55-86). Dordrecht: Springer Netherlands.

Neukum, G., Jaumann, R., Hoffmann, H., Hauber, E., & et al. (2004). Recent and episodic volcanic and glacial activity on Mars revealed by the High Resolution Stereo Camera. *Nature, 432*(7020), 971-979.

Phillips, R. J., Zuber, M. T., Solomon, S. C., Golombek, M. P., Jakosky, B. M., Banerdt, W. B., . . . Hauck, S. A. (2001). Ancient Geodynamics and Global-Scale Hydrology on Mars. *Science, 291*(5513), 2587-2591.

Pieri, D., & Baloga, S. (1986). *Eruption rate, area, and length relationships for some Hawaiian lava flows* (Vol. 30).

Pinkerton, H., James, M., & Jones, A. (2002). Surface temperature measurements of active lava flows on Kilauea volcano, Hawai′i. *Journal of Volcanology and Geothermal Research, 113*(1), 159-176. doi:http://dx.doi.org/10.1016/S0377-0273(01)00257-8

Pinkerton, H., & Norton, G. (1995). Rheological properties of basaltic lavas at sub-liquidus temperatures: laboratory and field measurements on lavas from Mount Etna. *Journal of Volcanology and Geothermal Research, 68*(4), 307-323. doi:http://dx.doi.org/10.1016/0377-0273(95)00018-7

Pinkerton, H., & Sparks, R. S. J. (1976). The 1975 sub-terminal lavas, mount etna: a case history of the formation of a compound lava field. *Journal of Volcanology and Geothermal Research, 1*(2), 167-182. doi:https://doi.org/10.1016/0377-0273(76)90005-6

Pinkerton, H., & Stevenson, R. J. (1992). Methods of determining the rheological properties of magmas at sub-liquidus temperatures. *Journal of Volcanology and Geothermal Research, 53*(1), 47-66. doi:https://doi.org/10.1016/0377-0273(92)90073-M

Pinkerton, H., & Wilson, L. (1988). The lengths of lava flows. *Abstracts of Papers Submitted to the Lunar and Planetary Science Conference, 19, Part 3*, 937-938.

Pinkerton, H., & Wilson, L. (1994). Factors controlling the lengths of channel-fed lava flows. *Bulletin of Volcanology, 56*(2), 108-120. doi:10.1007/BF00304106

Plescia, J. B. (2004). Morphometric properties of Martian volcanoes. *Journal of Geophysical Research: Planets, 109*(E3), n/a-n/a. doi:10.1029/2002JE002031

Ramsey, M. S., Harris, A. J. L., & Crown, D. A. (2016). What can thermal infrared remote sensing of terrestrial volcanoes tell us about processes past and present on Mars? Journal of Volcanology and Geothermal Research, 311(Supplement C), 198-216. doi:https://doi.org/10.1016/j.jvolgeores.2016.01.012

Roscoe, R. (1952). The viscosity of suspensions of rigid spheres. *British Journal of Applied Physics, 3*(8), 267.

Rossi, A. P., & Van Gasselt, S. (2010). Geology of Mars after the first 40 years of exploration. *Research in Astronomy and Astrophysics, 10*(7), 621.

Rowland, S. K., Garbeil, H., & Harris, A. J. L. (2005). Lengths and hazards from channel-fed lava flows on Mauna Loa, Hawai'i, determined from thermal and downslope modeling with FLOWGO. *Bulletin of Volcanology, 67*(7), 634-647. doi:http://dx.doi.org/10.1007/s00445-004-0399-x

Rowland, S. K., Harris, A. J. L., & Garbeil, H. (2004). Effects of Martian conditions on numerically modeled, cooling-limited, channelized lava flows. *Journal of Geophysical Research: Planets, 109*(E10), n/a-n/a. doi:10.1029/2004JE002288

Rowland, S. K., & Walker, G. P. (1988). Mafic-crystal distributions, viscosities, and lava structures of some Hawaiian lava flows. Journal of Volcanology and Geothermal Research, 35(1-2), 55-66.

Rowland, S. K., & Walker, G. P. (1990). Pahoehoe and aa in Hawaii: volumetric flow rate controls the lava structure. *Bulletin of Volcanology, 52*(8), 615-628. doi:10.1007/bf00301212

Russell, J. K. (1987). Crystallization and vesiculation of the 1984 eruption of Mauna Loa. *Journal of Geophysical Research: Solid Earth, 92*(B13), 13731-13743. doi:10.1029/JB092iB13p13731

Sabins, F. (1997). *Remote sensing: Principles and interpretation* (Third ed., pp. 265). Long Grove, Illinois: Waveland Press.

Scott, D. H., Tanaka, K. L., Planetary, G., Geophysics, P., Geological, S., United States. National, A., & Space, A. (Cartographer). (1986). Geologic map of the western equatorial region of Mars.

Shaw, H. R., Wright, T. L., Peck, D. L., & Okamura, R. (1968). The viscosity of basaltic magma; an analysis of field measurements in Makaopuhi lava lake, Hawaii. American Journal of Science, 266(4), 225-264. doi:10.2475/ajs.266.4.225

Smith, D. E., Zuber, M. T., Frey, H. V., Garvin, J. B., Head, J. W., Muhleman, D. O., . . . Sun, X. (2001). Mars Orbiter Laser Altimeter: Experiment summary after the first year of global mapping of Mars. *Journal of Geophysical Research: Planets, 106*(E10), 23689-23722. doi:10.1029/2000JE001364

Smith, D., Neumann, G., Arvidson, R.E., Guinness, E.A., Slavney, S., 2003. Mars global surveyor laser altimeter mission experiment gridded data record, NASA planetary

data system, MGS-M-MOLA-5-MEGDR-L3-V1.0.
Smith, D., Neumann, G., Ford, P., Arvidson, R.E., Guinness, E.A., Slavney, S., 1999b. Mars global surveyor laser altimeter precision experiment data record, NASA planetary data system, MGS-M-MOLA-3-PEDR-L1A-V1.0.
Smith, D. E., Zuber, M. T., Solomon, S. C., Phillips, R. J., Head, J. W., Garvin, J. B., . . . Duxbury, T. C. (1999a). The Global Topography of Mars and Implications for Surface Evolution. *Science, 284*(5419), 1495-1503.
Solomon, S. C., & Head, J. W. (1982). Evolution of the Tharsis Province of Mars: The importance of heterogeneous lithospheric thickness and volcanic construction. Journal of Geophysical Research: Solid Earth, 87(B12), 9755-9774. doi:10.1029/JB087iB12p09755
Thordarson, T., & Self, S. (1993). The Laki (Skaftár Fires) and Grímsvötn eruptions in 1783–1785. *Bulletin of Volcanology, 55*(4), 233-263. doi:10.1007/bf00624353
Vaucher, J., Baratoux, D., Toplis, M. J., Pinet, P., Mangold, N., & Kurita, K. (2009). The morphologies of volcanic landforms at Central Elysium Planitia: Evidence for recent and fluid lavas on Mars. *Icarus, 200*(1), 39-51. doi:http://dx.doi.org/10.1016/j.icarus.2008.11.005
Villeneuve, N., Neuville, D. R., Boivin, P., Bachèlery, P., & Richet, P. (2008). Magma crystallization and viscosity: A study of molten basalts from the Piton de la Fournaise volcano (La Réunion island). Chemical Geology, 256(3), 242-251. doi:https://doi.org/10.1016/j.chemgeo.2008.06.039
Walker, G. P. L., Huntingdon, A. T., Sanders, A. T., & Dinsdale, J. L. (1973). Lengths of Lava Flows [and Discussion]. *Philosophical Transactions of the Royal Society of London. Series A, Mathematical and Physical Sciences, 274*(1238), 107-118.
Wantim, M. N., Kervyn, M., Ernst, G. G. J., del Marmol, M. A., Suh, C. E., & Jacobs, P. (2013). Numerical experiments on the dynamics of channelised lava flows at Mount Cameroon Volcano with the FLOWGO thermo-rheological model. *Journal of Volcanology and Geothermal Research, 253*, 35-53. doi:http://dx.doi.org/10.1016/j.jvolgeores.2012.12.003
Warner, N. H., & Gregg, T. K. P. (2003). Evolved lavas on Mars? Observations from southwest Arsia Mons and Sabancaya volcano, Peru. *Journal of Geophysical Research: Planets, 108*(E10), n/a-n/a. doi:10.1029/2002JE001969
Wells, M. A., & Cullinane, T. (2007). Spectral discrimination of dolerite in crushed rock road aggregate, Perth, Western Australia. *International Journal of Remote Sensing, 28*(23), 5299-5314. doi:10.1080/01431160601105918
Wilson, L., & Head, J. (1983). A comparison of volcanic eruption processes on Earth, Moon, Mars, lo and Venus. *Nature (London), 302*, 663-669.
Wilson, L., & Head, J. W., III. (1994). Mars; review and analysis of volcanic eruption theory and relationships to observed landforms. *Reviews of Geophysics, 32*(3), 221-263. doi:http://dx.doi.org/10.1029/94RG01113
Wright, R., & Flynn, L. P. (2003). On the retrieval of lava-flow surface temperatures from infrared satellite data. *Geology, 31*(10), 893-896. doi:10.1130/G19645.1
Wyatt, M. B., & McSween, H. Y., Jr. (2002). Spectral evidence for weathered basalt as an alternative to andesite in the northern lowlands of Mars. *Nature, 417*(6886), 263-266. doi:http://dx.doi.org/10.1038/417263a
Zimbelman, J. R. (1985). Estimates of rheologic properties for flows on the Martian volcano Ascraeus Mons. *Journal of Geophysical Research: Solid Earth, 90*(S01), 157-162. doi:10.1029/JB090iS01p00157

Zimbelman, J. R. (1998). Emplacement of long lava flows on planetary surfaces. *Journal of Geophysical Research: Solid Earth*, *103*(B11), 27503-27516. doi:10.1029/98JB01123

Zimbelman, J. R., & Edgett, K. S. (1992). The Tharsis Montes, Mars; comparison of volcanic and modified landforms. *Proceedings of the Lunar and Planetary Science Conference, 22*, 31-44.

Zuber, M. T., Solomon, S. C., Phillips, R. J., Smith, D. E., Tyler, G. L., Aharonson, O., . . . Zhong, S. (2000). Internal Structure and Early Thermal Evolution of Mars from Mars Global Surveyor Topography and Gravity. *Science*, *287*(5459), 1788-1793.